

AD-A036 999

ILLINOIS UNIV AT URBANA-CHAMPAIGN
THE SINGULARITY EXPANSION REPRESENTATION OF THE TRANSIENT ELECT--ETC(U)
FEB 77 L W PEARSON, R MITTRA

F/G 20/14

AF-AFOSR-2861-75

UNCLASSIFIED

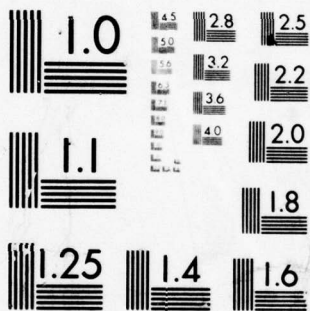
AFWL -TR-76-249

NL

1 OF 2

AD
A036999





MICROCOPY RESOLUTION TEST CHART
NATIONAL BUREAU OF STANDARDS-1963-A

AD A036999



THE SINGULARITY EXPANSION REPRESENTATION OF
THE TRANSIENT ELECTROMAGNETIC COUPLING
THROUGH A RECTANGULAR APERTURE

University of Illinois
Urbana, IL 61801

February 1977

Final Report



Approved for public release; distribution unlimited.

AIR FORCE WEAPONS LABORATORY
Air Force Systems Command
Kirtland Air Force Base, NM 87117

This final report was prepared by the University of Illinois, Urbana, Illinois, under AFOSR Grant No. 75-2861, Job Order 12090517 with the Air Force Weapons Laboratory, Kirtland Air Force Base, New Mexico. Captain Michael G. Harrison (ELP) was the Laboratory Project Officer-in-Charge.

When US Government drawings, specifications, or other data are used for any purpose other than a definitely related Government procurement operation, the Government thereby incurs no responsibility nor any obligation whatsoever, and the fact that the Government may have formulated, furnished, or in any way supplied the said drawings, specifications, or other data is not to be regarded by implication or otherwise as in any manner licensing the holder or any other person or corporation or conveying any rights or permission to manufacture, use, or sell any patented invention that may in any way be related thereto.

This report has been reviewed by the Information Office (OI) and is releasable to the National Technical Information Service (NTIS). At NTIS, it will be available to the general public, including foreign nations.

This technical report has been reviewed and is approved for publication.

Michael G. Harrison

MICHAEL G. HARRISON
Captain, USAF
Project Officer

FOR THE COMMANDER

Aaron B. Loggins

AARON B. LOGGINS
Lt Colonel, USAF
Chief, Phenomenology & Technology Br.

James L. Griggs, Jr.

JAMES L. GRIGGS, JR.
Colonel, USAF
Chief, Electronics Division

| | | |
|--------------|---------------|--------------------------|
| Approved for | White Section | <input type="checkbox"/> |
| NTIS | Buff Section | <input type="checkbox"/> |
| by | DATE | BY |
| REPRODUCTION | AVAILABILITY | STATUS |
| A | | |

DO NOT RETURN THIS COPY. RETAIN OR DESTROY.

UNCLASSIFIED

SECURITY CLASSIFICATION OF THIS PAGE (When Data Entered)

| 19 REPORT DOCUMENTATION PAGE | | READ INSTRUCTIONS BEFORE COMPLETING FORM | |
|---|-----------------------|---|--|
| 18 1. REPORT NUMBER AFWL-TR-76-249 | 2. GOVT ACCESSION NO. | 3. RECIPIENT'S CATALOG NUMBER 9 | |
| 4. TITLE (and Subtitle) 6 THE SINGULARITY EXPANSION REPRESENTATION OF THE TRANSIENT ELECTROMAGNETIC COUPLING THROUGH A RECTANGULAR APERTURE, | | 5. TYPE OF REPORT & PERIOD COVERED Final Report, | |
| 7. AUTHOR(s) 10 L. Wilson/Pearson Raj/Mittra | | 6. PERFORMING ORG. REPORT NUMBER | |
| 9. PERFORMING ORGANIZATION NAME AND ADDRESS The University of Illinois Urbana, IL 61801 | | 8. CONTRACT OR GRANT NUMBER(s) AFOSR Grant No. 75-2861 | |
| 11. CONTROLLING OFFICE NAME AND ADDRESS Air Force Weapons Laboratory (ELP) Kirtland Air Force Base, NM 87117 | | 10. PROGRAM ELEMENT, PROJECT, TASK AREA & WORK UNIT NUMBERS 64747F/12090517 | |
| 14. MONITORING AGENCY NAME & ADDRESS (if different from Controlling Office) 12 17p. | | 12. REPORT DATE February 1977 | |
| | | 13. NUMBER OF PAGES 116 | |
| | | 15. SECURITY CLASS. (of this report) Unclassified | |
| 16. DISTRIBUTION STATEMENT (of this Report) Approved for public release; distribution unlimited. | | 15a. DECLASSIFICATION/DOWNGRADING SCHEDULE | |
| 17. DISTRIBUTION STATEMENT (of the abstract entered in Block 20, if different from Report) 15 VAF-AFOSR-2861-75 | | | |
| 16 1209 17 05 | | | |
| 18. SUPPLEMENTARY NOTES | | | |
| 19. KEY WORDS (Continue on reverse side if necessary and identify by block number) Electromagnetic Fields and Waves Electromagnetic Pulse Apertures Interaction Singularity Expansion Method | | | |
| 20. ABSTRACT (Continue on reverse side if necessary and identify by block number) The singularity expansion method (SEM) is applied numerically to the electromagnetic dual of the rectangular aperture in a screen of infinite extent--the rectangular plate in free space. The SEM quantities are determined through a numerical treatment of the applicable electric field integral equations, and the details relating to computational efficiency are described. The pole trajectories for the plate are given for a range of aspect ratios, along with natural modes at specimen poles. Physical | | | |

DD FORM 1 JAN 73 1473

EDITION OF 1 NOV 65 IS OBSOLETE

UNCLASSIFIED

SECURITY CLASSIFICATION OF THIS PAGE (When Data Entered)


175750

y/B

~~UNCLASSIFIED~~

SECURITY CLASSIFICATION OF THIS PAGE(When Data Entered)

20. ABSTRACT

and numerical interpretations for these data are stated where possible. 

~~UNCLASSIFIED~~

SECURITY CLASSIFICATION OF THIS PAGE(When Data Entered)

SUMMARY

The singularity expansion method (SEM) is applied numerically to the electromagnetic dual of the rectangular aperture in a screen of infinite extent - the rectangular plate in free space. The SEM quantities are determined through a numerical treatment of the applicable electric field integral equations, and the details relating to computational efficiency are described. The pole trajectories for the plate are given for a range of aspect ratios, along with natural modes at specimen poles. Physical and numerical interpretations for these data are stated where possible.

Theoretical aspects of SEM relating to coupling coefficient forms and to the role of complex domain entire functions in the time domain SEM representation are explored. Correct coupling coefficient forms are found to depend on the asymptotic behavior at infinity of the frequency domain Green's function. This asymptotic behavior is unrecoverable in numerical solutions, however. Tests on the time domain expansion of the Green's function are proposed herein to determine the validity of a particular coupling coefficient form for a particular problem when the asymptotic behavior is unavailable. It is observed that Baum's Class 1 coupling coefficient can be made valid in problems where it otherwise would not apply at the expense of including an entire function contribution in the time domain expansion. This entire function contribution is, in general, significant.

TABLE OF CONTENTS

| | Page |
|--|------|
| 1. INTRODUCTION. | 7 |
| 1.1 Description of the Work. | 7 |
| 1.2 The Singularity Expansion Method | 7 |
| 1.3 Scope of the Present Work. | 8 |
| 1.4 Notation | 10 |
| 2. THE SEM REPRESENTATION AND INVERSION PROCEDURE. | 11 |
| 2.1 Introduction | 11 |
| 2.2 Transform Solution of Time Domain Electromagnetic Integral Equations | 12 |
| 2.2.1 Laplace transform of integral equation. | 12 |
| 2.2.2 An inversion of the transformed integral equation . | 14 |
| 2.2.3 The Laplace inversion of the solution | 15 |
| 2.3 An Analytically Tractable Example: The Transmission Line. | 20 |
| 2.3.1 Transmission line formulation | 20 |
| 2.3.2 Solution for the Green's function | 23 |
| 2.3.3 The causal time domain Green's function | 24 |
| 2.4 An Examination of the Time Domain Green's Function for the Thin-Wire Scatterer. | 28 |
| 2.5 Relation Between Coupling Coefficient Forms and Asymptotic Behavior. | 34 |
| 2.5.1 Effect of closure time on the coupling coefficient | 34 |
| 2.5.2 Heuristic development of the asymptotic form of $\frac{1}{r} - 1$ - a conservative coupling coefficient | 39 |
| 2.5.3 The purpose of the closure time in the time domain Green's function | 46 |
| 2.6 Conclusions. | 53 |
| 3. DETERMINATION OF THE SEM REPRESENTATION FOR A RECTANGULAR APERTURE. | 57 |
| 3.1 Introduction | 57 |
| 3.2 Thin-Plate Integral Equation Formulation for Complex Wavenumber | 58 |
| 3.2.1 The integral equations for complex frequency. . . . | 58 |
| 3.2.2 Symmetry conditions for the natural mode currents . | 60 |

| | Page |
|---|------|
| 3.3 The Numerical Model. | 65 |
| 3.3.1 Discretization of the integral equations. | 65 |
| 3.3.2 Algorithmic considerations in evaluating the system determinant. | 71 |
| 3.3.3 Numerical evaluations of natural modes, coupling vectors, and normalization constants. | 75 |
| 3.4 Numerical Checks and Convergence | 76 |
| 3.4.1 Pole convergence in the thin strip limit. | 76 |
| 3.4.2 Pole convergence for larger aspect ratios | 78 |
| 3.5 Pole Location Strategies | 81 |
| 4. SEM CHARACTERIZATION FOR THE RECTANGULAR PLATE. | 87 |
| 4.1 Introduction | 87 |
| 4.2 Pole Trajectories of the Plate/Aperture as a Function of Aspect Ratio. | 88 |
| 4.3 Natural Modes for the Rectangular Structure. | 92 |
| 4.3.1 Graphical representation of the modes | 92 |
| 4.3.2 The ++ modes. | 93 |
| 4.3.3 The +- modes. | 99 |
| 4.3.4 The -+ modes. | 102 |
| 4.3.5 The -- modes. | 106 |
| 4.4 Conclusions. | 106 |
| 5. CONCLUSIONS | 111 |
| REFERENCES. | 114 |

LIST OF FIGURES

| Figure | Page |
|---|------|
| 2.1. The Bromwich contour for inversion of the Laplace transform and possible closures thereof. | 16 |
| 2.2. Defining geometry for the transmission line example | 21 |
| 2.3. Representation of the causal Green's function for the short circuited transmission line | 27 |
| 2.4. Diagram of an acausal Green's function for the shorted transmission line | 29 |
| 2.5. Geometry for thin-wire scatterer analysis | 31 |
| 2.6. Time domain inverse kernel for thin-wire scatterer plotted as a function of time for a source point at $x' = 0$ and two observation points. | 33 |
| 2.7. Representation of a scatterer showing the "excited region" over which the illuminating wave has passed | 40 |
| 2.8. Geometry for discussion of asymptotic form of $\tilde{I}^{-1}(\bar{r}, \bar{r}', s)$. | 42 |
| 2.9. Representation of the expanding of support of current propagating away from source coupling at $L/4$ and $3L/4$ as a plane wave passes across a linear scatterer. | 45 |
| 2.10. Qualitative representation of a time domain inverse kernel plot showing the principal features which have bearing on the applicability of the kernel. | 51 |
| 3.1. Geometry of the rectangular plate | 59 |
| 3.2. Lowest-order natural mode current pairs for each of the symmetry cases, (a) J symmetric w.r.t. x-axis and symmetric w.r.t. y-axis, (b) symmetric-antisymmetric, (c) antisymmetric-symmetric, and (d) antisymmetric-antisymmetric | 67 |
| 3.3. Subsectioning for the discretization of the integral equations | 68 |
| 3.4. (a) Conceptual zoning for calculation of the interaction matrix, (b) example of the four interaction contributions to a single source term | 73 |
| 3.5. Calculated pole locations for thin strip for varying numbers of zones in the x-direction | 77 |

| Figure | Page |
|--|------|
| 3.6. Convergence study plots of the second ++ mode poles. . . . | 79 |
| 3.7. Trajectories of the first -- mode pole for various zonings and thinner aspect ratios. | 82 |
| 3.8. The scheme of separating the complex plane into quadrants to apply the argument number method in locating pole trajectories for the ++ modes. | 84 |
| 3.9. Projection of the oversquare ++ trajectory onto the undersquare -- trajectory. | 86 |
| 4.1. Pole trajectories for the four modal symmetries. | 89 |
| 4.2. Sample cuts in the natural mode distribution for the ++1 mode with $w/L = 1.0$ | 94 |
| 4.3. Sample cuts in the natural mode distribution for the ++2 mode with $w/L = 1.0$ | 95 |
| 4.4. Sample cuts in the natural mode distribution for the ++2 mode with $w/L = 0.6$ | 96 |
| 4.5. Sample cuts in the natural mode distribution for the ++2 mode with $w/L = 0.2$ | 97 |
| 4.6. Sample cuts in the natural mode distribution for the ++3 mode with $w/L = 1.0$ | 98 |
| 4.7. Sample cuts in the natural mode distribution for the +-1 mode with $w/L = 1.0$ | 100 |
| 4.8. Sample cuts in the natural mode distribution for the +-1 mode with $w/L = 0.2$ | 101 |
| 4.9. Sample cuts in the natural mode distribution for the +-1 mode with $w/L = 1.0$ | 103 |
| 4.10. Sample cuts in the natural mode distribution for the +-1 mode with $w/L = 0.3$ | 104 |
| 4.11. Sample cuts in the natural mode distribution for the -+4 mode with $w/L = 1.0$ | 105 |
| 4.12. Sample cuts in the natural mode distribution for the --1 mode with $w/L = 0.2$ | 107 |
| 4.13. Sample cuts in the natural mode distribution for the --6 mode with $w/L = 1.0$ | 108 |
| 4.14. Sample cuts in the natural mode distribution for the --6 mode with $w/L = 0.3$ | 109 |

1. INTRODUCTION

1.1 Description of the Work

This document presents the results of an investigation of representing the transient electromagnetic coupling through a rectangular aperture in a conducting screen by means of the Singularity Expansion Method [1]. The problem is formulated by means of its electromagnetic dual problem, the scattering from a rectangular plate. Consequently, the results are equally applicable to both members of the dual pair.

The Singularity Expansion Method (SEM) was introduced by Baum in 1971 [2]. It provides a compact means of representing broadband transient electromagnetic phenomena on resonant bodies in terms of the complex natural resonances of the body in the complex Laplace transform plane. For the problem at hand, these resonances are located numerically by means of a method of moments solution to an integral equation formulation. The integral equations used to model the plate structure are the integrated forms of the coupled electric field integral equations for the plate developed by Rahmat-Samii and Mittra [3]. Their original formulation holds for the real frequency domain, but extends directly to complex frequencies for the purposes herein.

1.2 The Singularity Expansion Method

Subsequent to its introduction by Baum in 1971, SEM has been applied to many problems - both numerically and analytically. In fact, in his introductory paper [2], Baum constructed the formal SEM solution for a perfectly conducting spherical scatterer. Marin conducted an analytical solution for a prolate spheroidal scatterer [4]. Umashankar has applied SEM analytically to the circular-loop wire antenna [5].

Marin and Latham [6] made an important theoretical contribution to SEM early in its development. They demonstrated that in the complex frequency plane the only singularities in fields for finite perfectly conducting bodies are poles. This fact precludes the need to consider branch-cut integrals and allows broader applications of analytic continuation concepts in the frequency plane.

Tesche performed the first numerical SEM construction [7]. He considered the problem of a thin cylindrical antenna. Subsequently, various workers have applied the method numerically to the L-wire [5], [6], [9], and several coupled cylinder problems [10]-[12]. Tesche explored SEM solutions to resistively loaded thin wires [13].

In previous work, surface problems have been treated by analytical methods, and numerical methods have been applied only to wire structures. One contribution of the present work is to indicate the viability of the numerical approach to SEM on a surface problem.

1.3 Scope of the Present Work

There are three chapters of original substance in this document. Chapter 2 delves into some theoretical considerations that are important to all SEM problems. Chapters 3 and 4 deal with the specific problem of the rectangular aperture.

Chapter 2 defines the SEM formalism and presents some new insights into the inversion procedure. In particular, it relates the asymptotic behavior of the frequency domain SEM representation to the definition of the so-called coupling coefficient. Because all of the terms which enter into the asymptotic form are not recoverable in numerically derived SEM solutions, we must turn to indirect means of defining the role of the asymptotic behavior.

It is shown in Chapter 2 that the asymptotic behavior of the frequency domain representation dictates the support of the time domain Green's function for a given problem.

We introduce two means of overcoming the difficulties presented by the unavailable asymptotic information. One of the means is a postulated asymptotic behavior which is conservative and physically consistent. This postulated form results in a new "class X" coupling coefficient which may be used directly or as a basis of comparison for other coupling coefficient forms. The second means is a test on the time domain expansion to determine for a specific problem whether or not any particular coupling coefficient form is consistent with the physical concept of causality. The class X coupling coefficient, the effect, imposes causality directly.

Chapter 3 presents the complex frequency generalization of the thin plate integral equations and describes the numerical procedures used in determining the SEM quantities from this formulation. Because the present problem is a surface problem, we are forced to be particularly conscious of numerical efficiency. Some algorithmic considerations that are important to numerical efficiency are discussed in Chapter 3. The argument number procedure proposed by Baum [14] was used to advantage in isolating the SEM poles in the course of this work. The details of its application are given in Section 3.5.

Chapter 4 contains numerically obtained SEM data for the rectangular plate. Complete pole data for a portion of the complex plane are given for rectangles with aspect ratios between 0.1 and 1.0. Representative natural mode data are given to provide the reader a means of physical interpretation of the resonances of the structure. Complete mode data and normalization constants are available for the plate in computer data base form [15].

1.4 Notation

As in many other fields problem areas, mathematical notation for SEM that is simultaneously compact and explicit is desirable but a bit elusive. The notation used herein is built on that of Baum (as in [2]). Symbols denoting functions are chosen for their connotative value where possible and their attributes are indicated with bars, tildes, etc. In particular, a vector quantity is indicated with a single overbar, and a dyadic quantity by two overbars. Laplace transform pairs are denoted with the same alphabetic and vector attribute symbols in both domains. A tilde (\sim) oversymbol identifies the function of the pair which has as its domain complex frequency, while the absence of the oversymbol denotes its time domain counterpart.

The inner product notation $\langle \bar{A}(\bar{r}), \bar{B}(\bar{r}) \rangle$ means, per Baum, to take the vector inner product and integrate over the common spatial support. We have occasion to indicate explicitly time domain convolution and complex contour integration in addition to the spatial inner product.

For example,

$$\bar{E}(\bar{r}, t) = \int_{-\infty}^{\infty} \langle \bar{\Gamma}(\bar{r}, \bar{r}', t - t'), \bar{J}(\bar{r}', t') \rangle dt'$$

indicates that the time domain vector quantity $\bar{E}(\bar{r}, t)$ is the time domain convolution $\int_{-\infty}^{\infty} dt'$ of the vector dot product of the dyad $\bar{\Gamma}$ and the vector \bar{J} integrated over the spatial support common to \bar{J} and $\bar{\Gamma}$. The transform domain counterpart to this expression is

$$\tilde{\bar{E}}(\bar{r}, s) = \langle \tilde{\bar{\Gamma}}(\bar{r}, \bar{r}', s), \tilde{\bar{J}}(\bar{r}', s) \rangle$$

where the tildes indicate transform domain image functions. The convolution in time appears as a simple multiplication in the complex frequency domain.

2. THE SEM REPRESENTATION AND INVERSION PROCEDURE

2.1 Introduction

In this chapter, we develop the Laplace transform solution for a general linear operator equation involving time and spatial variations. The point of view taken here departs from those of the previous workers addressing SEM solutions. In any SEM development, the primary concern is to construct the solution to the operator equation in a Laplace transform domain, where the transform is taken with respect to the time variable in the equation. Where previous work has viewed this transform solution as the composition of a residue series and an entire function in the transform variable, the present work views the transform domain solution as the product of a driving term and the transform of a causal Green's function or inverse kernel (see, for example, Stakgold [16]). The Green's function may be formally constructed as an eigenfunction expansion [17]. The inverse transform to the time domain may be taken by appealing to Jordan's lemma and the Cauchy residue theorem.

Indeed, the last step introduces one of the most significant features in the SEM approach. The appeal to Jordan's lemma [18] depends on the asymptotic form of the transform of the solution for large s . The causal behavior of the time domain solution is imposed through this asymptotic form.

The asymptotic behavior of the Green's function factor in the solution can, in principle, arise either from the infinite pole series or from the entire function term in the Mittag-Leffler representation [19] of the Green's function. For example, the Green's function for the

wire loop shows exponential asymptotic behavior resulting from the pole series [5]. For problems which are solved numerically, only a finite number of poles in this representation are available to us. Consequently, the asymptotic behavior of the transform solution is not directly recoverable. In Section 2.5.2 we develop heuristically the dominant asymptotic form for the Green's function of an integral operator with a free-space wave equation related kernel. This asymptotic form leads to a new type of coupling coefficient for the SEM representation. This new "class X" coupling coefficient is observed to impose causality directly on the solution. We observe, however, that other coupling coefficient forms that do not impose causality directly have been used with varying success by other workers. A procedure determining when the new form may be reduced to a simpler coupling coefficient form is presented. The procedure is based on observation of the time domain transform.

2.2 Transform Solution of Time Domain Electromagnetic Integral Equations

2.2.1 Laplace transform of integral equation

We state a general time domain integral equation for perfectly conducting finite extent bodies in free space as follows.

$$\int_{-\infty}^{\infty} \langle \bar{\Gamma}(\bar{r}, \bar{r}', t - t'), \bar{J}(\bar{r}', t') \rangle dt' = \bar{E}(\bar{r}, t), \quad \bar{r} \in B,$$

$$\left. \begin{aligned} \bar{\Gamma}(\bar{r}, \bar{r}', t) &= 0 \\ \bar{J}(\bar{r}, t) &= 0 \\ \bar{E}(\bar{r}, t) &= 0 \end{aligned} \right\} \quad \bar{r}, \bar{r}' \in B \text{ and } t < 0 \quad . \quad (2.1)$$

The brackets denote an integration of the vector inner product of the two operands over the support of the second operand. The $\tilde{\Gamma}$ term is a dyadic kernel to the integral equation; \tilde{J} is a characteristic electromagnetic quantity, generally a current density; and \tilde{E} is an incident wave or driving function field. The $\int_{-\infty}^{\infty} dt'$ is a time domain convolution. The body is denoted by the region B in \bar{r} space.

We proceed to construct the inversion of (2.1). Provided the Laplace transforms exist for both the left and right sides of the integral equation, we may write it in the transform domain

$$\langle \tilde{\Gamma}(\bar{r}, \bar{r}', s), \tilde{J}(\bar{r}', s) \rangle = \tilde{E}(\bar{r}, s), \quad \bar{r} \in B, \quad \text{Re } s > 0. \quad (2.2)$$

The tilde (\sim) overbar is used to denote the Laplace transform domain images of the associated functions from (2.1). In the familiar way, the convolution over the time variable goes over to an algebraic product in the transform domain.

We appeal to the physical concept of causality and observe that each of the three functions in question must be causal in nature so long as we require that $\tilde{E}(\bar{r}, t)$ be zero for finite \bar{r} and t less than some finite starting time. If all of our functions are causal, we may with an appropriate shift of origin convert our transform to a one-sided one. Therefore, it is sufficient to consider all transforms as one-sided ones, and we define, explicitly,

$$\{f(t)\} = \tilde{f}(s) = \int_0^{\infty} f(t) e^{-st} dt, \quad \text{Re } s > 0 \quad (2.3)$$

under the condition that $f(t)$ be bounded for $t > 0$.

2.2.2 An inversion of the transformed integral equation

We may write a formal solution to (2.2) as

$$\tilde{J}(\bar{r}, s) = \langle \tilde{\Gamma}^{-1}(\bar{r}, \bar{r}', s), \bar{E}(\bar{r}', s) \rangle \quad (2.4)$$

where the inverse kernel $\tilde{\Gamma}^{-1}$ (Green's function) is the solution to

$$\langle \tilde{\Gamma}^{-1}(\bar{r}, \bar{r}', s), \tilde{\Gamma}(\bar{r}', \bar{r}_0, s) \rangle = \bar{I} \delta(\bar{r} - \bar{r}_0) \quad , \quad (2.5)$$

\bar{I} is an identity dyad on the three spatial vectors and $\delta(\bar{r} - \bar{r}_0)$ is a three-dimensional Dirac distribution. The equations (2.4) and (2.5) hold in a distributional sense. In fact, Schwartz points out that $\tilde{\Gamma}^{-1}$ cannot be a function [20]. In addition, Marin and Latham have shown that for perfectly conducting bodies of finite extent, $\tilde{\Gamma}^{-1}(\bar{r}, \bar{r}', s)$ is analytic in s except for pole singularities [6]. This latter property gives us the means of expressing our desired result, the time domain solution to (2.1) in terms of residues at the poles of $\tilde{\Gamma}^{-1}$. Since the body is passive and since a pole s_p gives rise to temporal behavior $\exp(s_p t)$, we conclude that all of the poles of $\tilde{\Gamma}^{-1}$ have a negative real part so as to produce decaying time behavior. Further, since (2.1) has a real solution, it is evident that the poles must occur in conjugate pairs in the complex s plane.

For many problems of practical interest, we can recover by numerical or analytical methods the poles which dominate the time response for excitations whose spectra are bandlimited. The key to practical application of SEM is to construct the time domain solution to (2.1) in such a way that it is accurately represented by this hopefully modest collection of poles.

2.2.3 The Laplace inversion of the solution

The time domain solution to (2.1) is constructed by forming the Laplace inversion of (2.4) as follows.

$$\begin{aligned}\bar{J}(\bar{r}, t) &= \frac{1}{2\pi j} \int_{C_B} \bar{\tilde{J}}(\bar{r}, s) e^{st} ds \\ &= \frac{1}{2\pi j} \int_{C_B} \langle \bar{\tilde{I}}^{-1}(\bar{r}, \bar{r}', s), \bar{\tilde{E}}(\bar{r}', s) \rangle e^{st} ds \quad .\end{aligned}\quad (2.6)$$

The integration is over the Bromwich contour, C_B , given by

$$s = \sigma + j\omega$$

$$\sigma > 0, \quad \omega \in (-\infty, \infty) \quad .$$

The real value of s for this contour must be chosen so as to place C_B in the region of convergence for the representation of $\bar{\tilde{J}}(\bar{r}, s)$. Consequently, we must have a representation for $\bar{\tilde{J}}(\bar{r}, s)$ which is valid in the right-half plane, i.e., that is convergent and solves (2.2) for s such that $\sigma > \sigma_0$, or a fixed positive number.

Typically, in the Laplace transform theory, one appeals to an indirect evaluation of the integral of (2.6). Namely, C_B is closed with a semicircular arc of infinite radius either to the right or to the left as indicated in Figure 2.1. The asymptotic behavior of the integrand generally dictates that the integrand vanish on one or the other of the semicircles so that Jordan's lemma [18] is satisfied and the integration over either the closed contour $C_B + C_\infty^+$ or $C_B + C_\infty^-$ is equivalent to integration over C_B alone. The composite contours $C_B + C_\infty^+$ and $C_B + C_\infty^-$

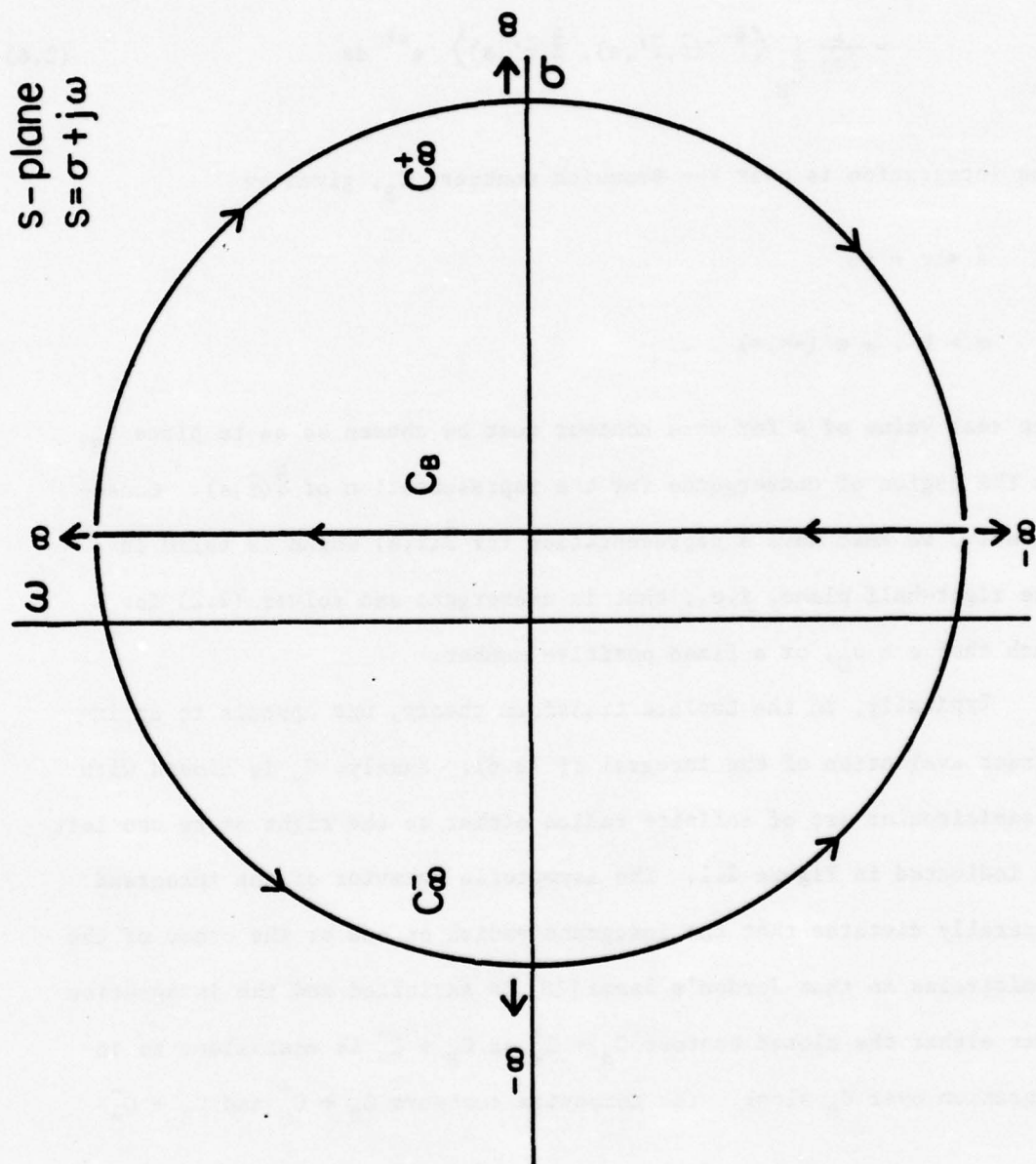


Figure 2.1. The Bromwich contour for inversion of the Laplace transform and possible closures thereof.

are closed contours. Hence, when integration along C_B is equivalent to integration over one of these closed contours, we may evaluate the integration by means of Cauchy's residue theorem so that information at the poles of $\tilde{J}(\bar{r}, s)$ suffices to represent $\tilde{J}(\bar{r}, t)$.

Before considering the asymptotic form of $\tilde{J}(\bar{r}, s)$, we shall develop the singularity expansion in a formal manner. The eigenfunction expansion point of view [17] is taken in this development.

The formal solution to (2.2) may be constructed by means of an eigenfunction expansion. That is, we define the left- and right-hand eigenvectors $\tilde{L}_n(\bar{r}, s)$, $\tilde{R}_n(\bar{r}, s)$ by the eigenvalue equations

$$\langle \tilde{L}_n(\bar{r}', s), \tilde{\Gamma}(\bar{r}, \bar{r}', s) \rangle = \lambda_n(s) \tilde{L}_n(\bar{r}, s) \quad (2.7a)$$

and

$$\langle \tilde{\Gamma}(\bar{r}, \bar{r}', s), \tilde{R}_n(\bar{r}', s) \rangle = \lambda_n(s) \tilde{R}_n(\bar{r}, s) \quad , \quad (2.7b)$$

where $\{\lambda_n(s)\}$ forms the set of eigenvalues for the operator defined by $\tilde{\Gamma}(s)$. We then proceed by expanding "everything in sight" in (2.2) in terms of the \tilde{R}_n . Then by means of the biorthogonality relation between \tilde{L}_n and \tilde{R}_n , we arrive at the explicit representation

$$\tilde{J}(\bar{r}, s) = \sum_n \lambda_n^{-1}(s) \frac{\langle \tilde{L}_n(\bar{r}', s), \tilde{E}(\bar{r}', s) \rangle}{\langle \tilde{L}_n(\bar{r}', s), \tilde{R}_n(\bar{r}', s) \rangle} \tilde{R}_n(\bar{r}, s) \quad . \quad (2.8)$$

Thus, we may write the inverse kernel $\tilde{\Gamma}^{-1}$ in (2.4) as an expansion of dyadic terms

$$\tilde{\Gamma}^{-1}(\bar{r}, \bar{r}', s) = \sum_n \lambda_n^{-1}(s) \frac{\tilde{R}_n(\bar{r}, s) \tilde{L}_n(\bar{r}', s)}{\langle \tilde{L}_n(\bar{r}', s), \tilde{R}_n(\bar{r}', s) \rangle} \quad . \quad (2.9)$$

Now the poles of $\tilde{\Gamma}^{-1}(\bar{r}, \bar{r}', s)$ are observed to be zeros of $\{\lambda_n(s)\}$. In [17] Baum discusses the specific associations between elements of the set of poles of $\tilde{\Gamma}^{-1}\{s_m\}$ and elements of the set of eigenvalues $\{\lambda_n(s)\}$ and designs an indexing scheme which explicitly represents these associations. We are not concerned with the specifics of the association here, however.

Thence, for t such that the asymptotic behavior of $\tilde{J}(\bar{r}, s) \exp(st)$ allows left closure and assuming simple poles for notational simplicity

$$\begin{aligned} \tilde{J}(\bar{r}, t) &= \frac{1}{2\pi j} \int_{C_B} \sum_n \lambda_n^{-1}(s) \frac{\langle \tilde{L}_n(\bar{r}', s), \tilde{E}(\bar{r}', s) \rangle}{\langle \tilde{L}_n(\bar{r}', s), \tilde{R}_n(\bar{r}', s) \rangle} \tilde{R}_n(\bar{r}, s) e^{st} ds \\ &= \sum_m \frac{d\lambda_n(s_m)^{-1}}{ds} \frac{\langle \tilde{L}_n(\bar{r}', s_m), \tilde{E}(\bar{r}', s_m) \rangle}{\langle \tilde{L}_n(\bar{r}', s_m), \tilde{R}_n(\bar{r}', s_m) \rangle} \tilde{R}_n(\bar{r}, s_m) e^{s_m t} \quad (2.10) \end{aligned}$$

The summation embraces the entire pole set $\{s_m\}$. The notation used assumes that $\lambda_n(s_m) = 0$. At the poles the eigenvectors $\tilde{L}_n(\bar{r}, s_m)$ and $\tilde{R}_n(\bar{r}, s_m)$ become the coupling vectors $\bar{C}_m(\bar{r})$ and the natural mode vector $\bar{M}_m(\bar{r})$, respectively, i.e., from (2.7)

$$\langle \bar{C}_m(\bar{r}'), \tilde{\Gamma}(\bar{r}, \bar{r}', s_m) \rangle = 0 \quad (2.11a)$$

and

$$\langle \tilde{\Gamma}(\bar{r}, \bar{r}', s_m), \tilde{M}_m(\bar{r}') \rangle = 0 \quad (2.11b)$$

Using this modal notation and the relationship

$$\frac{d\lambda_n(s_m)}{ds} = \frac{\langle \tilde{L}_n(\bar{r}, s_m), \frac{d}{ds} \tilde{\Gamma}(\bar{r}, \bar{r}', s_m), \tilde{R}_n(\bar{r}', s_m) \rangle}{\langle \tilde{L}_n(\bar{r}', s_m), \tilde{R}_n(\bar{r}, s_m) \rangle}$$

we rewrite (2.10) as

$$\bar{J}(\bar{r}, t) = \sum_m \beta_m \langle \bar{C}_m(\bar{r}), \tilde{E}(\bar{r}, s_m) \rangle \tilde{M}_m(\bar{r}) e^{s_m t} u(t). \quad (2.12)$$

The normalization constants

$$\beta_m = \langle \bar{C}_m(\bar{r}), \frac{d}{ds} \tilde{\Gamma}(\bar{r}, \bar{r}', s_m), \tilde{M}_m(\bar{r}') \rangle^{-1} \quad (2.13)$$

are introduced in arriving at (2.12). The inner product in (2.12) is generally defined as a "coupling coefficient" depending on a particular spatial form of \tilde{E} .

The formal expansion of (2.12) is the fundamental SEM form - the singularity expansion. The construction by which we arrived at (2.12) is a formal one. As subsequent sections of this chapter show, it is indeed valid for a sufficiently large t . For t less than some time T_0 , the right-hand closure to (2.6) is valid and $\bar{J}(\bar{r}, t)$ is zero. However, for some solutions, there is a time interval during which neither a zero value nor the particular expansion (2.12) is a correct representation for $\bar{J}(\bar{r}, t)$. The SEM approach for these solutions seeks to modify the coupling coefficient term in such a way that a form similar to (2.12) holds

for all time for which $\bar{J}(\bar{r}, t)$ is nonzero. In succeeding sections, we present some alternative coupling coefficient forms to this end and basic guidelines for using these forms.

2.3 An Analytically Tractable Example: The Transmission Line

2.3.1 Transmission line formulation

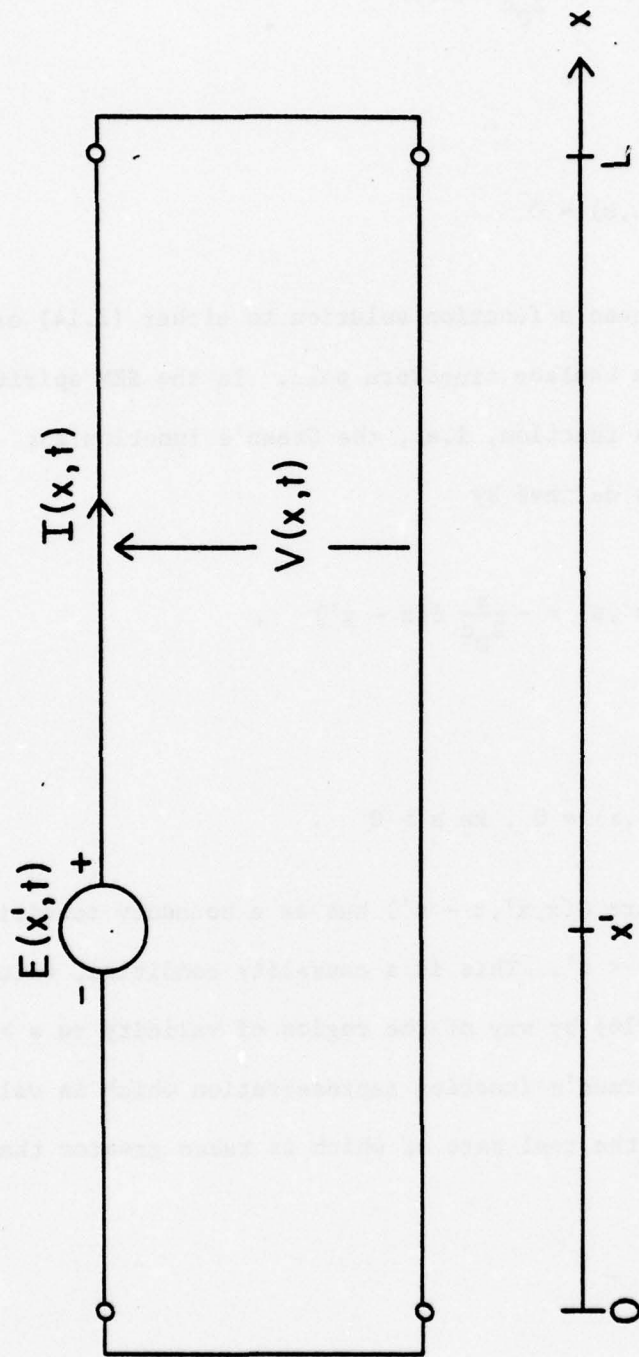
The lossless transmission line proves to be an instructive example in studying the principle involved in the SEM representation*. The instructiveness of the problem results from the facts that the SEM representation is fully derivable analytically and that we may represent both resonant and nonresonant structures with finite and infinite extent lines. Because the residue series is analytically summable, it is possible to explore its asymptotic behavior and the consequences of truncation of the representation to a finite collection of poles. It happens that the problem is best addressed through a differential equation rather than an integral equation of the form (2.1). However, concepts applicable to the Green's function here transfer directly to the "inverse kernel" Green's function of the integral equation.

The geometry of the transmission line is defined in Figure 2.2. The line is shorted at $x = 0$ and $x = L$. The wave equation describing this line and the associated boundary conditions are

$$\left[\frac{\partial^2}{\partial x^2} - \frac{1}{c^2} \frac{\partial^2}{\partial t^2} \right] I(x, t) = - \frac{1}{Z_0 c} \frac{\partial}{\partial t} E(x, t),$$

$$\frac{\partial}{\partial x} I(0, t) = \frac{\partial}{\partial x} I(L, t) = 0, \quad I(x, t) = 0, \quad t < 0 \quad . \quad (2.14)$$

* The author is grateful to Professor D. R. Wilton of the University of Mississippi for his suggesting the transmission line example and for providing notes on parts of the formulation presented here.



Characteristic impedance = Z_0

Figure 2.2. Defining geometry for the transmission line example.

In the transform domain

$$\left[\frac{d^2}{dx^2} - (s/c)^2 \right] \tilde{I}(x,s) = -\frac{s}{Z_0 c} \tilde{E}(x,s) \quad (2.15)$$

with

$$\frac{\partial}{\partial x} \tilde{I}(0,s) = \frac{\partial}{\partial x} \tilde{I}(L,s) = 0 \quad .$$

We may obtain a causal Green's function solution to either (2.14) or (2.15), and the two are a Laplace transform pair. In the SEM spirit we write an s-domain Green's function, i.e., the Green's function for (2.15). This function is defined by

$$\left[\frac{d^2}{dx^2} - (s/c)^2 \right] \tilde{G}(x,x',s) = -\frac{s}{Z_0 c} \delta(x - x') \quad , \quad (2.16)$$

with

$$\tilde{G}'(0,x',s) = \tilde{G}'(L,x',s) = 0 \quad , \quad \text{Re } s > 0 \quad .$$

The time domain counterpart $G(x,x',t - t')$ has as a boundary condition $G(x,x',t - t') = 0$, for $t < t'$. This is a causality condition, which appears implicitly in (2.16) by way of the region of validity $\text{Re } s > 0$. That is, we must have a Green's function representation which is valid on the Bromwich contour, the real part of which is taken greater than zero.

2.3.2 Solution for the Green's function

We choose to write a constructive solution to (2.16) as

$$\tilde{G}(x, x', s) = \frac{1}{2Z_0} \left\{ e^{-s|x-x'|/c} + \sum_{n=0}^{\infty} e^{-s2nL/c} \left[e^{-s[x+x']/c} + e^{-s[2L+(x-x')]/c} + e^{-s[2L-(x+x')]/c} + e^{-s[2L-(x-x')]/c} \right] \right\}, \text{Re } s > 0 \quad (2.17)$$

This form is taken because of its instructiveness in showing explicitly the traveling-wave components corresponding to a direct wave and an infinite summation embracing reflections and multiple reflections at the shorted ends of the line.

A closed-form representation results directly from (2.17) by way of the sum formula

$$\sum_{n=0}^{\infty} e^{-s2nL/c} = [1 - e^{-2sL/c}]^{-1}, \text{Re } s > 0$$

The closed-form expression is

$$\tilde{G}(x, x', s) = \frac{1}{2Z_0} \left\{ \frac{\cosh s[L - |x - x'|]/c + \cosh s[L - (x + x')]/c}{\sinh sL/c} \right\} \quad (2.18)$$

Alternatively, this form can be constructed directly from (2.16) without using the summation form. The expression (2.18) is the unique analytic continuation of the expression (2.17).

This Green's function is the counterpart to the inverse kernel $\tilde{\Gamma}^{-1}$ developed for the integral equation formulation in Section 2.2. For this example, however, we have an explicit closed-form representation for \tilde{G} .

This function has the residue series representation

$$\tilde{G}(x, x', s) = \frac{c}{Z_0 L} \sum_{n=0}^{\infty} \epsilon_n \frac{s \cos(n\pi x/L) \cos(n\pi x'/L)}{s^2 + (n\pi c/L)^2}, \quad (2.19)$$

where

$$\epsilon_n = \begin{cases} 1, & n = 0 \\ 2, & n \neq 0 \end{cases}$$

is Neumann's number. It may be shown that (2.19) is a complete representation for $\tilde{G}(x, x', s)$ as expressed in (2.18). That is, $\tilde{G}(x, x', s)$ does not have an entire function component in its Mittag-Leffler representation. It is clear, however, from (2.18) that asymptotically $\tilde{G}(x, x', s)$ is exponential in character.

We also observe that (2.19) fits the dyadic form of (2.9) for the inverse operator, namely, dyadic numerator terms with poles in the denominator at $s = \pm jn\pi c/L$. Thus, for a general excitation function $\tilde{E}(x', s)$, we can construct

$$\tilde{I}(x, s) = \frac{c}{Z_0 L} \sum_{n=0}^{\infty} \epsilon_n \left\langle \frac{s \cos(n\pi x/L) \cos(n\pi x'/L)}{s^2 + (n\pi c/L)^2}, \tilde{E}(x', s) \right\rangle \quad (2.20)$$

2.3.3 The causal time domain Green's function

Alternatively, we can invert (2.19) to obtain the causal time domain Green's function. Then a general solution may be formed from the convolution

$$I(x, t) = \int_{-\infty}^{\infty} \langle G(x, x', t - t'), E(x', t') \rangle dt' \quad (2.21)$$

We proceed to construct $G(x, x', t)$ here because it is instructive to observe the time domain effects of operations which we perform in determining $I(x, t)$ from the transform domain form (2.20).

The time domain Green's function is given by

$$G(x, x', t) = \int_{C_B} \tilde{G}(x, x', s) e^{st} ds \quad (2.22)$$

In order to evaluate this integral in the conventional fashion, we require a knowledge of the asymptotic behavior of \tilde{G} . This is discernible from (2.18), viz.,

$$\tilde{G}_2(x, x', s) = \begin{cases} e^{-s|x-x'|/c}, & \text{in r.h.p.} \\ e^{s|x-x'|/c}, & \text{in l.h.p.} \end{cases} \quad (2.23)$$

We draw attention to the fact that this information is obscured in the residue series form (2.19). It is also noteworthy that \tilde{G} has different asymptotic forms in the right- and left-half planes. Thus, for $t < |x - x'|/c$ we may close C_B to the right, and since \tilde{G} has no poles for $\text{re } s > 0$, $G(x, x', t) = 0$, $t < |x - x'|/c$. For $t > -|x - x'|/c$ we may close C_B to the left and obtain the residue contributions at the poles of $\tilde{G}(x, x', s)$. We write then

$$G(x, x', t) = \begin{cases} 0, & t < |x - x'|/c \\ \frac{c}{LZ_0} \sum_{n=0}^{\infty} \epsilon_n \cos(n\pi x'/L) \cos(n\pi x/L) \cos(n\pi ct/L), & t > -|x - x'|/c \end{cases} \quad (2.24)$$

For $t \in (-|x - x'|/c, |x - x'|/c)$ the function must be zero, but the series representation is valid, too! It must sum to zero. Indeed, the time $|x - x'|/c$ is the arrival time for an incident wave at the observation point x launched from a spatially impulsive generator at x' . The phenomena coming to play are seen if we use the following distributional identity to sum the above series.

$$\sum_{-\infty}^{\infty} \delta(x - an) = \sum_{-\infty}^{\infty} e^{j2n\pi x/a} = \sum_{n=0}^{\infty} \epsilon_n \cos(2n\pi x/a) \quad .$$

This yields

$$\begin{aligned} G(x, x', t) = \frac{c}{4LZ_0} \sum_{n=-\infty}^{\infty} \{ & \delta[t - (x - x')/c - 2nL/c] \\ & + \delta[t + (x - x')/c - 2nL/c] \\ & + \delta[t - (x + x')/c - 2nL/c] \\ & + \delta[t + (x + x')/c - 2nL/c]\}, t > -|x - x'|/c, \end{aligned} \quad (2.25a)$$

or

$$\begin{aligned} G(x, x', t) = \frac{c}{4LZ_0} \left\{ & \delta[t - |x - x'|/c] + \delta[t - (x + x')/c] \right. \\ & + \sum_{n=1}^{\infty} \{ \delta[t - |x - x'|/c - 2nL/c] \\ & + \delta[t + |x - x'|/c - 2nL/c] \\ & + \delta[t - (x + x')/c - 2nL/c] \\ & \left. + \delta[t + (x + x')/c - 2nL/c] \} \right\} \quad . \end{aligned} \quad (2.25b)$$

This distribution is represented symbolically as a function of time in Figure 2.3. The distribution represents a direct current impulse arriving at the observation point at a time $|x - x'|/c$ accompanied by three impulses arriving after undergoing reflections at one or both shorted ends of the line. This pattern is replicated with a period $2L/c$ since the line is lossless and nondispersive.

We observe that the series representation yields replication into negative time as well, as shown by the dashed line impulses in Figure 2.3.

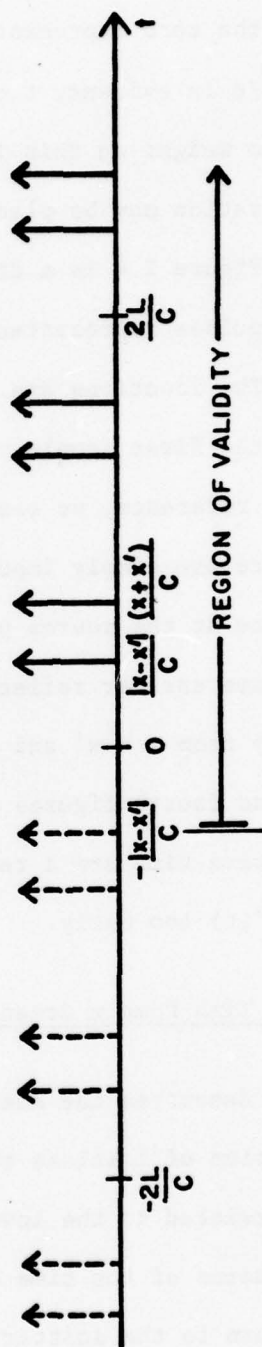


Figure 2.3. Representation of the causal Green's function for the short-circuited transmission line. This pattern replicates infinitely with a period $2L/c$. The impulses shown by dashed lines are those which are components to the series representation, but are outside the region of validity of the representation.

It is clear that if we attempted to apply the series for $t < -|x - x'|/c$, we would obtain erroneous results. The phenomenon of having both the series representation and the zero representation for $-|x - x'|/c < t < |x - x'|/c$ is evident, too. The series converges to a distribution which has zero weight on this interval.

A "physical" interpretation may be placed upon the acausal pulses which appear in (2.25a). Figure 2.4 is a diagram showing the spatial location of the current impulses represented by (2.25a) for a source generator $\delta(x - x')\delta(t)$. The locations are shown for four times - spaced at an increment Δt - with the first sample taken at $-\Delta t$. Using the $t = 0$ (second) figure as a reference, we see that the negative time impulses in the first figure are simply impulses propagating toward the source so as to coalesce at the source point at $t = 0$. All of the other negative time terms are earlier reflections of these pulses. The subsequent propagation away from $x = x'$ and reflection at the short at $x = L$ shown in the third and fourth figures are evident. The current impulses occurring in negative time are a result of applying the singularity expansion for $G(x, x', t)$ too early.

2.4 An Examination of the Time Domain Green's Function for the Thin-Wire Scatterer

The preceding section describes the analytical aspects of an SEM solution for a shorted section of lossless transmission line. The consequences of the analysis related to the inversion are evident when the solution is viewed in terms of the time domain Green's function for the problem. We now turn to the scattering problem perhaps most closely associated with the transmission line - that of the scattering from a perfectly conducting thin wire.

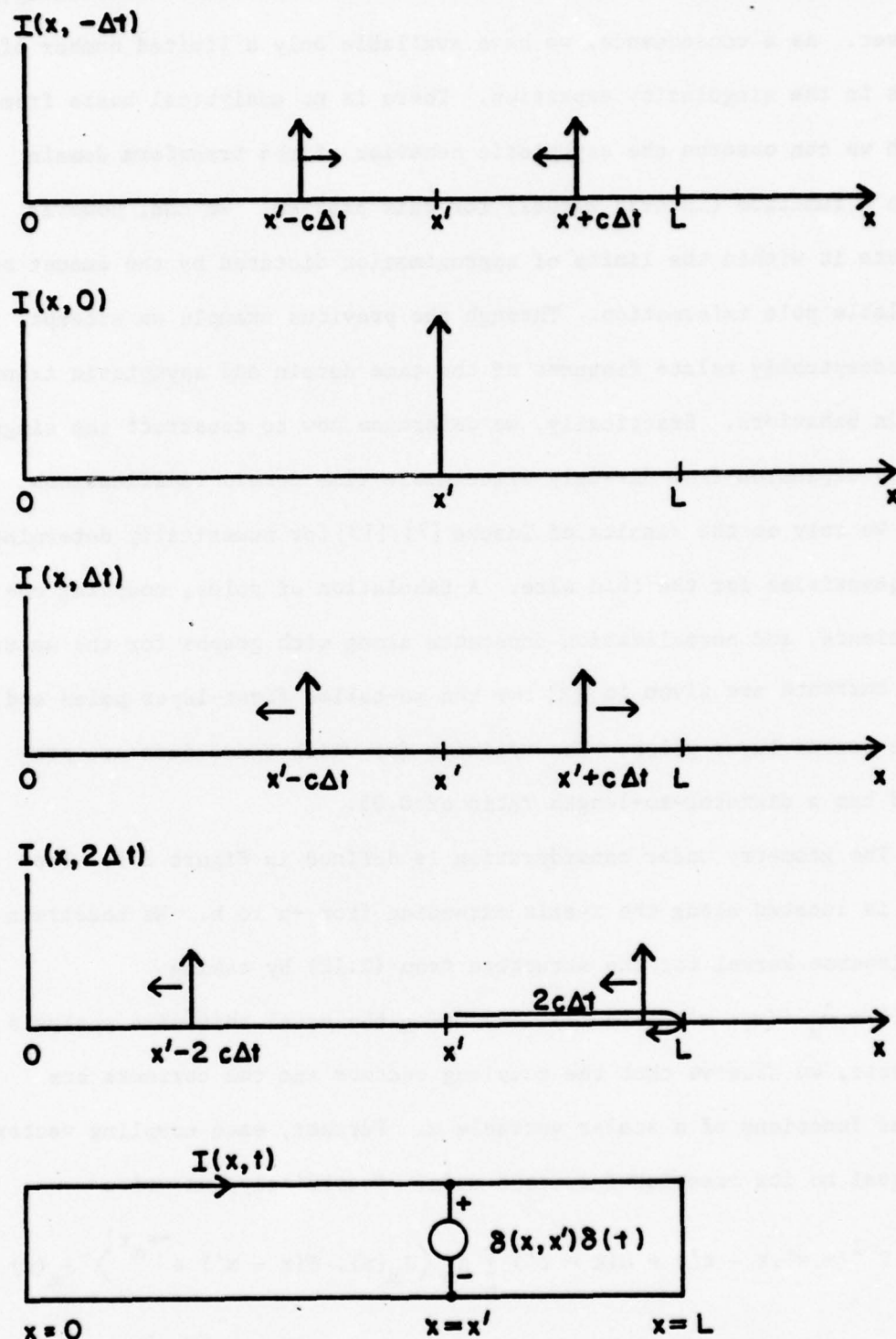


Figure 2.4. Diagram of an acausal Green's function for the shorted transmission line. The spatial location of the impulses of current on the line are shown "frozen" in time for four times each advanced Δt over its predecessor. Time $t = 0$ is given in the second graph.

The SEM solution to this problem must be constructed numerically, however. As a consequence, we have available only a limited number of terms in the singularity expansion. There is no analytical basis from which we can observe the asymptotic behavior of the transform domain Green's function (inverse kernel) for this problem. We can, however, compute it within the limits of approximation dictated by the amount of available pole information. Through the previous example we attempt to conceptually relate features of the time domain and asymptotic transform domain behaviors. Practically, we determine how to construct the singularity expansion from directly discernible time domain ramifications.

We rely on the results of Tesche [7],[13] for numerically determined SEM quantities for the thin wire. A tabulation of poles, coupling coefficients, and normalization constants along with graphs for the natural mode currents are given in [13] for ten so-called first-layer poles and three second-layer poles. The cylinder for which these data are provided has a diameter-to-length ratio of 0.05.

The geometry under consideration is defined in Figure 2.5. The wire is located along the x-axis extending from $-h$ to h . We construct the inverse kernel for the structure from (2.12) by taking $\bar{E}(\bar{r}, t) = \hat{u}_x \delta(x - x') \delta(t - t')$. By using the usual thin-wire analysis concepts, we observe that the coupling vectors and the currents are scalar functions of a scalar variable x . Further, each coupling vector is equal to its associated current mode. Accordingly, we write

$$\begin{aligned} \Gamma^{-1}(x, x', t - t') &= u(t - t') \sum_m \beta_m \left\langle J_m(x), \delta(x - x') e^{-s_m t'} \right\rangle J_m(x) e^{s_m t} \\ &= u(t - t') \sum_m \beta_m J_m(x') J_m(x) e^{s_m (t - t')} \end{aligned} \quad (2.26)$$

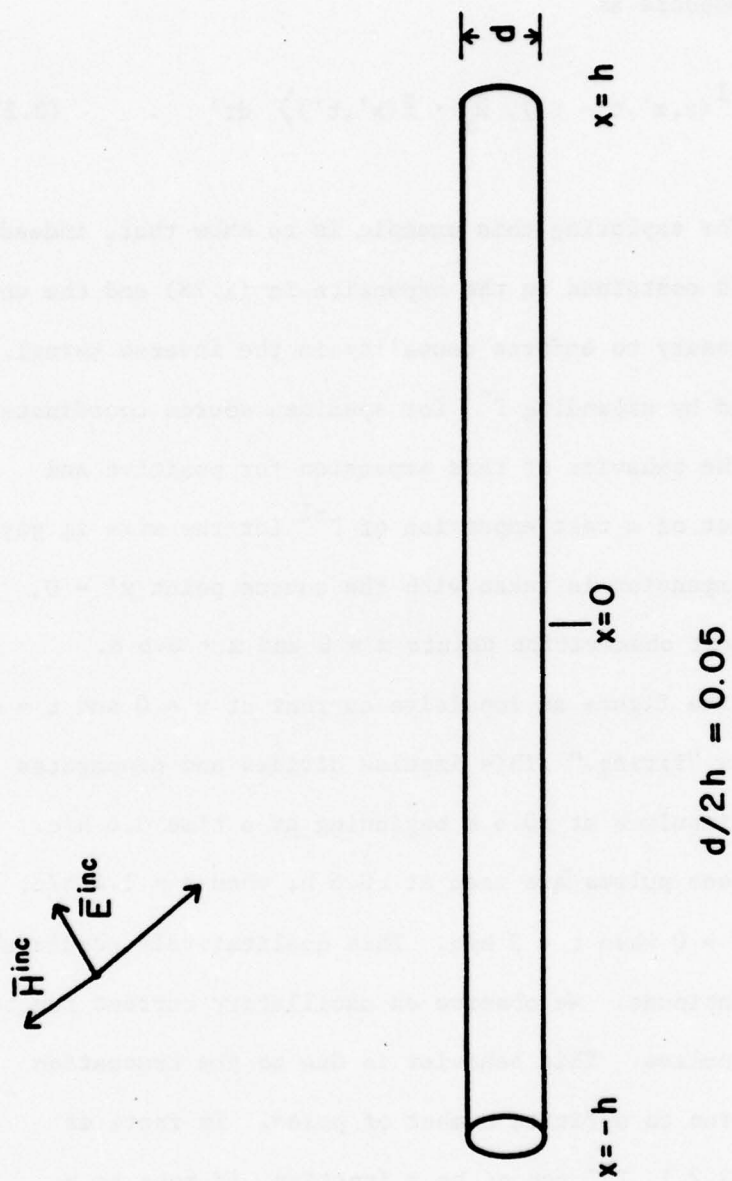


Figure 2.5. Geometry for thin-wire scatterer analysis.

We include the unit step function $u(t - t')$ at this stage as a precaution to insure that our inverse kernel is causal. This matter is explored further below. Then for an arbitrary incident field, we construct the current response as

$$J(x,t) = \int_{-\infty}^{\infty} \left\langle \Gamma^{-1}(x,x',t-t'), \hat{u}_x \cdot \bar{E}(x',t') \right\rangle dt' \quad . \quad (2.27)$$

The motivation for exploring this example is to show that, indeed, an acausal response is contained in the expansion in (2.28) and the unit step function is necessary to enforce causality in the inverse kernel. This is readily tested by expanding Γ^{-1} for specimen source coordinates x', t' and studying the behavior of this expansion for positive and negative times. A plot of a test expansion of Γ^{-1} for the wire is given in Figure 2.6. The expansion is taken with the source point $x' = 0$, $t' = 0$ for two different observation points $x = 0$ and $x = 0.6 h$.

We observe from the figure an impulsive current at $x = 0$ and $t = 0$ due to the generator's "firing." This impulse divides and propagates outwardly to produce impulses at $\pm 0.6 h$ beginning at a time $0.6 h/c$. The reflections of these pulses are seen at $\pm 0.6 h$, when $t = 1.4 h/c$, and then merging at $z = 0$ when $t = 2 h/c$. This qualitatively predictable reflection pattern continues. We observe an oscillatory current function between the expected pulses. This behavior is due to the truncation of the residue expansion to a finite number of poles. In fact, as mentioned in Section 2.2.1, Γ^{-1} cannot be a function, it must be a Dirac-like distribution. The smoothness and the oscillations are attributable to expansion of the distribution in terms of a finite number of continuous functions.

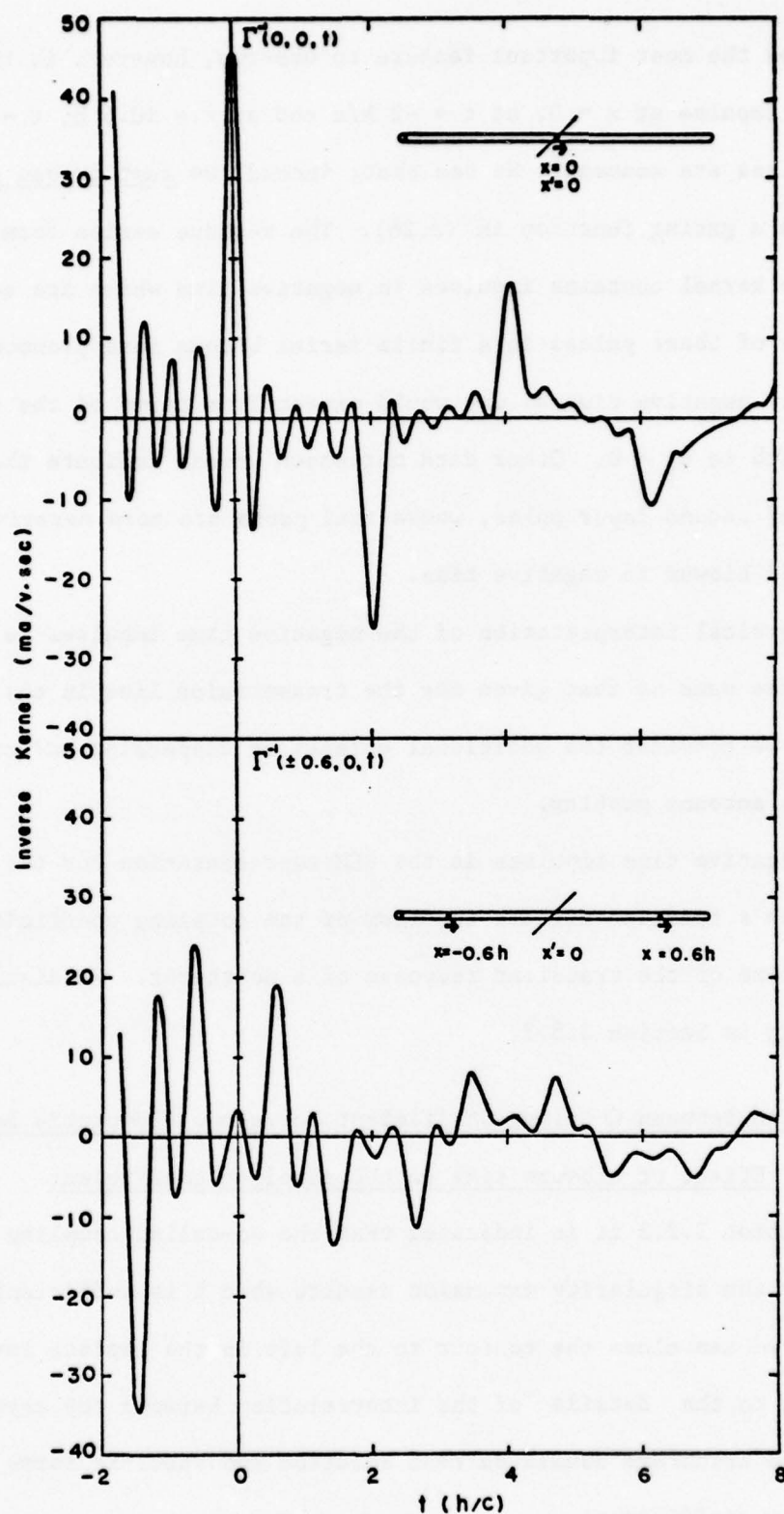


Figure 2.6. Time domain inverse kernel for thin-wire scatterer plotted as a function of time for a source point at $x' = 0$ and two observation points. The function was expanded from SEM data at ten first layer poles as given by Tesche [9].

Perhaps the most important feature to observe, however, is the presence of an impulse at $x = 0$, at $t = -2 h/c$ and at $x = \pm 0.6 h$, $t = -0.6 h/c$. These impulses are acausal! We see that, indeed, we must impose causality on Γ^{-1} with a gating function in (2.26). The residue series form for the inverse kernel contains impulses in negative time which are acausal. The effects of these pulses in a finite series become more pronounced with increasingly negative time as one would expect from terms of the form $\exp(s_i t)$ with $\text{re } s_i < 0$. Other data not shown herein indicate that the inclusion of second layer poles, whose real parts are more negative, causes a very rapid blowup in negative time.

The physical interpretation of the negative time impulses is essentially the same as that given for the transmission line in the preceding section if we consider the additional effects of dispersion and radiative loss in the antenna problem.

The negative time impulses in the SEM representation for the time domain Green's function affects the form of the coupling coefficient in the early time of the transient response of a scatterer. We discuss this bearing in Section 2.5.3.

2.5 Relation Between Coupling Coefficient Forms and Asymptotic Behavior

2.5.1 Effect of closure time on the coupling coefficient

In Section 2.2.3 it is indicated that the so-called coupling coefficient for the singularity expansion results when t is sufficiently large that we can close the contour to the left in the Laplace inversion. We now turn to the details of the interrelation between the asymptotic form for the transform domain current solution and specific forms of the coupling coefficient.

We begin with (2.6), the expression for the current solution to an electromagnetic integral equation.

$$\bar{J}(\bar{r}, t) = \frac{1}{2\pi j} \int_{C_B} \langle \bar{\Gamma}^{-1}(\bar{r}, \bar{r}', s), \bar{E}(\bar{r}, s) \rangle e^{st} ds \quad (2.28)$$

For the present discussion, we consider the incident field $\bar{E}(\bar{r}, t)$ to be a plane wave with a time history $f(t)$. We restrict $f(t)$ to have a transform $\tilde{f}(s)$ which is algebraic. Further, we consider object poles alone. The concepts which follow are readily extended to include wave-form poles and more general $\tilde{f}(s)$. These restrictions are cast in the interest of notational simplicity. A plane wave field may be written in the time domain as

$$E(\bar{r}, t) = \bar{E}_0 f(t) * \delta(t - \hat{p} \cdot \bar{r}/c) \quad , \quad (2.29)$$

where \bar{E}_0 is the polarization vector of the wave, \hat{p} is a unit vector in the direction of wave propagation and "*" denotes convolution. This representation has the transform domain image

$$\bar{E}(\bar{r}, s) = \bar{E}_0 \tilde{f}(s) e^{-s\hat{p} \cdot \bar{r}/c} \quad (2.30)$$

We use this expression in (2.6), change the order of integration between the spatial and transform variables, and denote the spatial integration explicitly to obtain

$$\bar{J}(\bar{r}, t) = \frac{1}{2\pi j} \int_{\text{Body}} \int_{C_B} \bar{\Gamma}^{-1}(\bar{r}, \bar{r}', s) \cdot \bar{E}_0 e^{-s\hat{p} \cdot \bar{r}'/c} \tilde{f}(s) e^{st} ds d\bar{r}' \quad (2.31)$$

The interchange of integration operators allows us to observe the asymptotic behavior of the integrand. Were the spatial integral performed first, the asymptotic behavior would be obscured in the process.

The s -dependent terms in the integrand in (2.31) are the inverse kernel, the exponential of the propagating incident wave, the transform of the incident wave time history $\tilde{f}(s)$, and the Laplace kernel. The asymptotic behavior of $\tilde{\Gamma}^{-1}$ is generally unavailable to us. The propagating wave term and the Laplace kernel each have explicit exponential behavior. Thus, the algebraic behavior of $\tilde{f}(s)$ and the potential algebraic behavior of $\tilde{\Gamma}^{-1}$ are dominated by the exponential factors. This restricts our interest in the asymptotic behavior of $\tilde{\Gamma}^{-1}$ to exponential terms. Accordingly, we define asymptotic forms for C_{∞}^{+} and C_{∞}^{-} as

$$\tilde{\Gamma}^{-1}(\bar{r}, \bar{r}', s) \sim \begin{cases} \bar{\bar{D}}_R d_R(s) e^{-sT_R(\bar{r}, \bar{r}')} & s \in C_{\infty}^{+} \\ \bar{\bar{D}}_L d_L(s) e^{-sT_L(\bar{r}, \bar{r}')} & s \in C_{\infty}^{-} \end{cases}, \quad (2.32)$$

where the $d(s)$ functions are algebraic and the $\bar{\bar{D}}$ are dyads which are independent of s . The coefficients of s in these terms are dimensionally equal to time. They depend on both \bar{r} and \bar{r}' , potentially, and might be positive or negative.

We restrict attention to cases where $T_L(\bar{r}, \bar{r}') \leq T_R(\bar{r}, \bar{r}')$ so that pole information suffices in the representation for the Laplace inversion of $\tilde{\Gamma}^{-1}$.

For $t > T_L(\bar{r}, \bar{r}')$ the integrand in (2.31) decays exponentially as $|s| \rightarrow \infty$ on C_∞^- , the left-side closure of C_B . For such t we close C_B with C_∞^- and a residue series results from the inner integral. For $t < T_L(\bar{r}, \bar{r}') \leq T_R(\bar{r}, \bar{r}')$ the integrand decays on C_∞^+ so that closing to the right yields zero. In the dyadic notation of (2.12), we write explicitly

$$J(\bar{r}, t) = \int_{\text{Body}} u[t - \hat{p} \cdot \bar{r}'/c - T_L(\bar{r}, \bar{r}')] \sum_{m=0}^{\infty} \beta_m \bar{E}_0 \cdot \bar{C}_m(\bar{r}') \tilde{f}(s_m) e^{s_m(t - \hat{p} \cdot \bar{r}'/c)} \cdot M_m(\bar{r}) d\bar{r}' , \quad (2.33)$$

where

$$u(t) = \begin{cases} 1, & t > 0 \\ 0, & t < 0 \end{cases} .$$

A bandlimited behavior in $\tilde{f}(s)$ allows us to truncate the series at, say, M terms in (2.33). Then with some rearrangement we have

$$\bar{J}(\bar{r}, t) = \sum_m^M f(s_m) \beta_m \int_{\text{Body}} \bar{E}_0 \cdot \bar{C}_m(\bar{r}') e^{-s_m \hat{p} \cdot \bar{r}'/c} u[t - \hat{p} \cdot \bar{r}' - T_L(\bar{r}, \bar{r}')] d\bar{r}' \cdot M_m(\bar{r}) e^{s_m t} . \quad (2.34)$$

The integral factor is a "generalized" coupling coefficient

$$\eta_m(\bar{r}, t) = \int_{\text{Body}} \bar{E}_0 \cdot \bar{C}_m(\bar{r}') e^{-s_m \hat{p} \cdot \bar{r}'/c} u[t - \hat{p} \cdot \bar{r}' - T_L(\bar{r}, \bar{r}')] d\bar{r}' . \quad (2.35)$$

Then (2.34) is written as the singularity expansion form

$$\bar{J}(\bar{r}, t) = \sum_m^M \tilde{f}(s_m) \beta_m \eta_m(\bar{r}, t) \bar{M}_m(\bar{r}) e^{s_m t} . \quad (2.36)$$

There are two commonly used coupling coefficient forms which may be interpreted as particularizations of the generalized form in (2.35).

Baum terms these as class 1 and class 2 coupling coefficients, respectively [1]

A class 1 form results by assuming

$$T_L(\bar{r}, \bar{r}') = -\hat{p} \cdot \bar{r}'/c + t' \quad (2.37)$$

where t' is some chosen "turn-on time" typically taken to be the arrival time of the incident wave at the body. This results in the current expansion

$$\bar{J}(\bar{r}, t) = u(t - t') \sum_m^M \tilde{f}(s_m) \beta_m \eta_m^{(1)} \bar{M}_m(\bar{r}) e^{s_m t} , \quad (2.38)$$

where the class 1 coupling coefficient is

$$\eta_m^{(1)} = \int_{\text{Body}} \bar{E}_0 \cdot \bar{C}_m(\bar{r}') e^{-s_m \hat{p} \cdot \bar{r}'/c} d\bar{r}' . \quad (2.39)$$

It is notable that the assumed T_L form is independent of \bar{r} and yields a coupling coefficient independent of both \bar{r} and t . For some applications of SEM such as broadband equivalent circuit modeling of distributed structures [21], this feature is useful.

A class 2 coupling coefficient results when T_L is taken to be zero. Then a series in the form (2.36) results but with the coupling coefficient

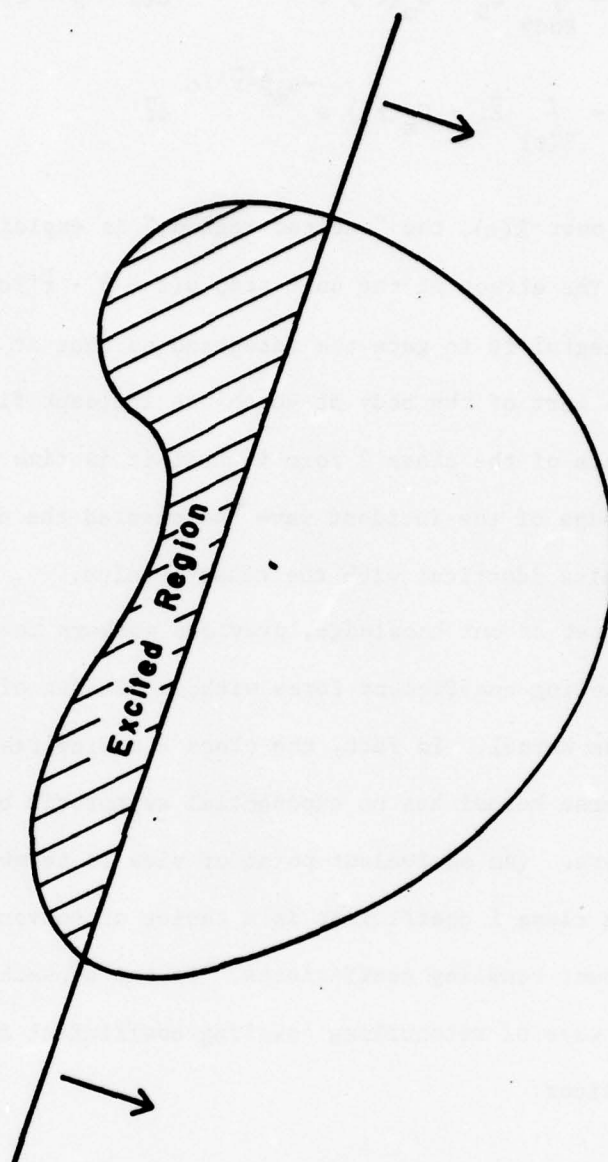
$$\begin{aligned}
\eta_m^{(2)}(t) &= \int_{\text{Body}} \bar{\mathbf{E}}_0 \cdot \bar{\mathbf{C}}_m(\bar{\mathbf{r}}') e^{-s_m \hat{\mathbf{p}} \cdot \bar{\mathbf{r}}'/c} u(t - \hat{\mathbf{p}} \cdot \bar{\mathbf{r}}'/c) d\bar{\mathbf{r}}' \\
&= \int_{R(t)} \bar{\mathbf{E}}_0 \cdot \bar{\mathbf{C}}_m(\bar{\mathbf{r}}') e^{-s_m \hat{\mathbf{p}} \cdot \bar{\mathbf{r}}'/c} d\bar{\mathbf{r}}' .
\end{aligned} \tag{2.40}$$

The integral over $R(t)$, the "excited region," is explained with the aid of Figure 2.7. The effect of the unit step $u(t - \hat{\mathbf{p}} \cdot \bar{\mathbf{r}}'/c)$ in the coupling coefficient integral is to gate the integrand so that it contributes to $\eta_n(t)$ only over the part of the body at which the incident field has arrived. A notable feature of the class 2 form is that it is time dependent. After the leading edge of the incident wave has cleared the object, it takes on a constant value identical with the class 1 value.

To the best of our knowledge, previous workers in SEM have made their choice of coupling coefficient forms without benefit of the asymptotic form of the inverse kernel. In fact, the class 2 choice results from an assumption that the inverse kernel has no exponential asymptotic behavior, i.e., $T_L = 0$ as in the above. (An equivalent point of view is termwise integration of the series.) The class 1 coefficient is a choice of convenience in the form of time independent coupling coefficients. In the subsections which follow, we explore some ways of reconciling coupling coefficient forms with their inverse kernel expansions.

2.5.2 Heuristic development of the asymptotic form of $\frac{1}{r}^{-1}$ - a conservative coupling coefficient

The transmission line example developed in Section 2.3 gives us insight because the asymptotic form of the transform domain Green's function is clearly discernible. In that example, there is some freedom of choice in the left closure time because of the time interval during which both the SEM representation and zero are valid representations of the solution.



Leading edge
of incident wave

Figure 2.7. Representation of a scatterer showing the "excited region" over which the illuminating wave has passed.

The other example in our knowledge where the asymptotic form of the SEM Green's function has been explored is in the loop [5]. For the majority of SEM problems, which rely on numerical determination of the component terms for the expansion, it seems unlikely that the necessary asymptotic information will be directly available. In the following paragraphs, we develop heuristically a useable form for the asymptotic behavior and a new coupling coefficient form which results from it. It is observed to be unnecessarily conservative for the examples of the transmission line and the wire scatterer considered in previous sections. But, because of its conservatism, it provides a "safe" approach to new problems. The next subsection provides a numerical test procedure for relaxing the conservatism to an appropriate degree.

We consider the asymptotic behavior of the inverse kernel with the aid of Figure 2.8. The object is represented in a coordinate system with origin at 0. A source point is located at $\bar{r} = \bar{r}'$ and an observation point at $\bar{r} = \bar{r}_0$. The vector \bar{S} is a local surface vector at \bar{r}' with unit components in two orthogonal directions in the local tangent plane. At the observation point \bar{r}_0 , the current on the body is represented by $\bar{J}(\bar{r}_0, t)$ in local vector components. Then if an excitation

$$\bar{E}(\bar{r}, t) = \bar{S}(\bar{r}') \delta(\bar{r} - \bar{r}') \delta(t) \quad ,$$

which is impulsive in time and space, is applied at the observation point, we expect a temporal response which departs from zero only for $t > |\bar{r} - \bar{r}'|/c$. That is,

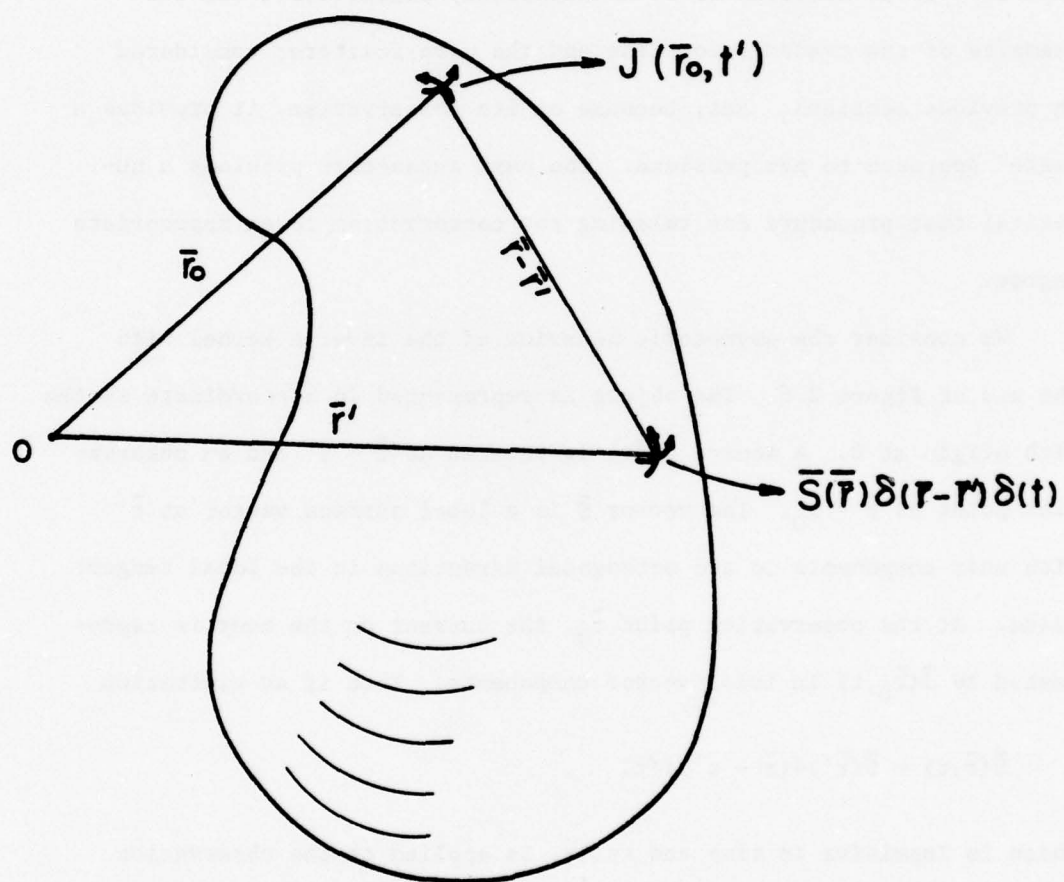


Figure 2.8. Geometry for discussion of asymptotic form of $\tilde{\Gamma}^{-1}(\bar{r}, \bar{r}', s)$.

$$\bar{J}(\bar{r}_0, t) = \begin{cases} 0 & , \quad t < |\bar{r}_0 - \bar{r}'|/c \\ \bar{I}(\bar{r}_0, t) & , \quad t > |\bar{r}_0 - \bar{r}'|/c \end{cases}$$

with $\bar{I}(\bar{r}_0, t) = 0$ only at isolated points in t .

By definition, $\bar{F}^{-1}(\bar{r}, \bar{r}', t)$ is the kernel of a convolution relating $\bar{E}(\bar{r}, t)$ and $\bar{J}(\bar{r}, t)$ so that

$$\begin{aligned} \bar{J}(\bar{r}_0, t) &= \int_{-\infty}^{\infty} \langle \bar{F}^{-1}(\bar{r}_0, \bar{r}, t - t'), \bar{S}(\bar{r}') \delta(\bar{r} - \bar{r}') \delta(t') \rangle dt' \\ &= \langle \bar{F}^{-1}(\bar{r}_0, \bar{r}', t) \cdot \bar{S}(\bar{r}') \rangle . \end{aligned}$$

It follows that in the transform domain $\bar{J}(\bar{r}_0, s)$ and hence $\bar{F}^{-1}(\bar{r}_0, \bar{r}', s)$ must have an exponential factor to represent the time delay $|\bar{r}_0 - \bar{r}'|/c$.

We write explicitly

$$\bar{F}^{-1}(\bar{r}, \bar{r}', s) = e^{-s|\bar{r}-\bar{r}'|/c} \bar{K}(\bar{r}, \bar{r}', s)$$

and

$$\bar{F}^{-1}(\bar{r}, \bar{r}', s) \sim \bar{D} d(s) e^{-s|\bar{r}-\bar{r}'|/c} , \quad |s| \rightarrow \infty , \quad (2.41)$$

where \bar{K} is a dyadic function, $d(s)$ is a polynomial in s , and \bar{D} is a dyad independent of s . This assumed asymptotic behavior implies a closure time term of the form

$$T_L(\bar{r}, \bar{r}) = -|\bar{r} - \bar{r}'|/c$$

in (2.32)-(2.35). Specifically, a coupling coefficient of the following form results.

$$\eta_m^{(X)}(\bar{r}, t) = \int_{\text{Body}} \bar{E}_0 \cdot \bar{C}_m(\bar{r}') e^{-s_m \hat{p} \cdot \bar{r}' / c} u[t - \hat{p} \cdot \bar{r}' - |\bar{r} - \bar{r}'|/c] dr' . \quad (2.42)$$

We term this a "class X" coupling coefficient. (An X-tra cautious one.)

Some observations are in order. First, the class X coupling coefficient is dependent on both the observation time and the observation point. This feature renders it more complex than either the class 1 or class 2 forms discussed in Section 2.5.1. Second, the effect of the unit step function in (2.42) is to enforce causality directly. This feature is seen clearly in Figure 2.9 for the example of a thin-wire scatterer. The figure represents the support of current induced by the incident wave at two coupling points: $x = L/4$ and $x = 3L/4$. The coupling is from an incident plane wave whose direction of propagation forms an angle of 60 degrees with the axis of the scatterer. Consequently, its velocity component along the scatterer is $2c$. The time sequence depicts the wave arriving at the scatterer at $t = 0$, coupling at $x = L/4$ $t = L/8$, progressing on at $t = L/4c$, coupling at $x = 3L/4$ $t = 3L/8$, etc. The support for the current induced when the wave is at $x = L/4$ is depicted as impulsive when the wave is at that point then propagating outwardly at the velocity of light. A similar phenomenon is pictured for coupling at $x = 3L/4$.

A third observation is that this explicit enforcement of causality may prove unduly stringent. For example, the resonant transmission line problem in Section 2.3 led to a Green's function with the asymptotic behavior

$$\tilde{G}(x, x', s) \sim \begin{cases} e^{-s|x-x'|/c} & \text{in r.h.p.} \\ e^{s|x-x'|/c} & \text{in l.h.p.} \end{cases} ,$$

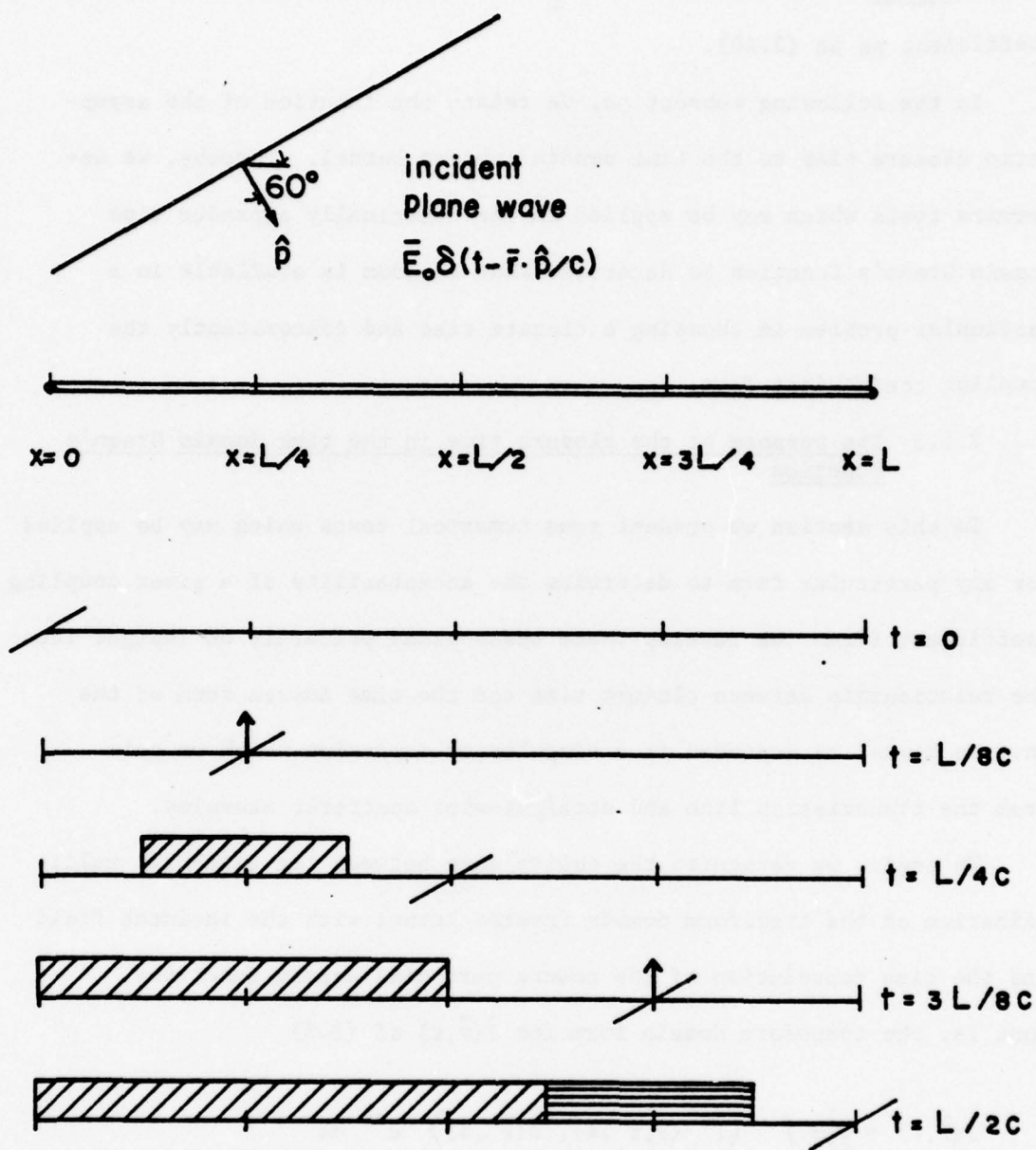


Figure 2.9. Representation of the expanding of support of current propagating away from source coupling at $L/4$ and $3L/4$ as a plane wave passes across a linear scatterer.

i.e., different asymptotic forms on C_{∞}^{-} and C_{∞}^{+} so that there is a period of time during which either closure of C_B is valid. For this example we can choose a left closure time $T_L' = 0$ and obtain a class 2 coupling coefficient as in (2.40).

In the following subsection, we relate the function of the asymptotic closure time to the time domain inverse kernel. Thereby, we determine tests which may be applied to the numerically expanded time domain Green's function to determine what freedom is available in a particular problem in choosing a closure time and concomitantly the coupling coefficient form.

2.5.3 The purpose of the closure time in the time domain Green's function

In this section we present some numerical tests which may be applied for any particular form to determine the acceptability of a given coupling coefficient form. We develop these tests based primarily on insight into the relationship between closure time and the time domain form of the inverse kernel as expanded in a singularity expansion which we gain from the transmission line and straight-wire scatterer examples.

To begin, we recognize the equivalence between the algebraic multiplication of the transform domain inverse kernel with the incident field and the time convolution of the counterpart time domain functions.

That is, the transform domain form for $\bar{J}(\bar{r}, t)$ of (2.6)

$$J(\bar{r}, t) = \frac{1}{2\pi j} \int_{C_B} \langle \tilde{\Gamma}^{-1}(\bar{r}, \bar{r}', s), \tilde{E}(\bar{r}', s) \rangle e^{st} ds$$

is equivalent to the time domain convolution

$$\bar{J}(\bar{r}, t) = \int_{-\infty}^{\infty} \langle \bar{F}^{-1}(\bar{r}, \bar{r}', t - t'), \bar{E}(\bar{r}', t') \rangle dt' \quad (2.43)$$

Any assumed asymptotic behavior applied in the inversion of (2.6) is carried in (2.43) in the individual inversions of \bar{F}^{-1} and \bar{E} .

To illustrate we again call upon the straight-wire scatterer example. Suppose that we expanded its response due to an obliquely incident plane wave using a class 1 coupling coefficient. In Section 2.5.1 Equation (2.37), it is pointed out that the class 1 coupling coefficient assumes an asymptotic form

$$\bar{F}^{-1}(\bar{r}, \bar{r}', s) \sim \bar{D} e^{-s(t' - \hat{p} \cdot \bar{r}'/c)},$$

where \bar{D} is a dyadic constant. Let us consider a configuration like that in Figure 2.9 and take the turn-on time $t' \sim 0$, the time at which the incident wave first impinges on the wire. The class 1 assumption is

$$\bar{F}^{-1} \sim \bar{D} e^{s \hat{p} \cdot \bar{r}'/c}, \quad \text{in l.h.p.}$$

The extreme value of \bar{r}' in the spatial inner product is $|\bar{r}'| = L$. In this extreme by using the class 1 coupling coefficient, we effectively gate the singularity expansion of $\bar{F}^{-1}(\bar{r}, \bar{r}', t)$ with the unit step $u(t + \hat{p} \cdot \bar{r}'/c)$ with $|\bar{r}'| = L$. This requires that the singularity expansion manifest causal behavior for all $t > -\hat{p} \cdot \bar{r}'/c$. In the 60 degree incidence example, this translates to $t > -L/2c$.

A reference to the plotted singularity expansion of $\bar{F}^{-1}(\bar{r}, \bar{r}', t)$ for the wire given in Figure 2.6 indicates that the required behavior is not present. There is an acausal impulse at $-|x - x'|/c$ so that the required clear time is not present for all observation points on

the wire. On the other hand, the class 2 coupling coefficient, which assumes that $\tilde{\Gamma}^{-1}$ has no asymptotic exponential behavior, i.e., it is algebraic, dictates a required causal behavior in the expansion for $t > 0$. We observe from the figure that this is the case within the frequency and numerical error limitations of the expansion.

Tesche [22] has attempted to use the class 1 coupling coefficient without success on the thin wire. The results which he presents in [7],[13] indicate that the class 2 coefficient form is satisfactory. Wilton and Umashankar have experimented with both forms on the L-wire scatterer as in [5]. Their experience has been similar to Tesche's with regard to the success and failure of the forms [23]. This experience is consistent with the theoretical evidence herein.

This illustration suggests a test which may be applied in the time domain to determine the appropriateness of a given coupling coefficient form to a particular problem. Corresponding to any coupling coefficient form is an assumed asymptotic behavior for the transform domain inverse kernel. This asymptotic form in turn implies a turn-on time for the time domain inverse kernel. For specimen source and observation points, the time domain inverse kernel can be numerically expanded in the manner of Section 2.4. By observation, one can determine whether or not the turn-on time associated with the coupling coefficient in question and the observed time domain inverse kernel are consistent with causality. Stated as a "recipe":

A. Analytical steps

1. For the particular coupling coefficient to be tested, discern the support of the integrand in the coupling coefficient inner

product, e.g., $u(t - t')$ as in (2.38)-(2.39) for class 1,
 $u(t - \hat{p} \cdot \bar{r}'/c)$ in (2.40) for class 2,
 $u(t - \hat{p} \cdot \bar{r}' - |\bar{r} - \bar{r}'|/c)$ in (2.42) for class X.

2. Translate the unit step argument into the left-half plane asymptotic form which it assumes, i.e., $\exp(sA)$, where A is the argument of the unit step. For class 2 plane wave excitation this is

$$e^{s(t - \hat{p} \cdot \bar{r}'/c)} = e^{st} e^{-s\hat{p} \cdot \bar{r}'/c} (e^0) .$$

3. Factor out the e^{st} Laplace kernel and the incident wave asymptotic behavior. For class 2 this takes care of both factors above. The remaining term $-e^0$ above - is the assumed asymptotic behavior of the inverse kernel implicit in the coupling coefficient form. The exponent of this exponential is $-s$ times the implicit turn-on time of the time domain inverse kernel.

B. Numerical steps (assuming that poles, modes, etc., are known)

1. Pick some specimen observation/source point pairs representing extreme cases (e.g., maximum separation on the object) and the transition in between.
2. For sources impulsive in time and space, expand the time domain inverse kernel in the manner of Section 2.4.
3. Observe the "clear time" in the time domain kernel prior to the arrival of the first causal disturbance. In particular, note the dependence of this time on \bar{r} and \bar{r}' .

- C. Compare the required clear time with the turn-on time determined in Step A3. Does the inverse kernel provide clear time between the turn-on time implied coupling coefficient and the first causal disturbance?

If the answer to this question is "No," then a more conservative coupling coefficient must be used. The class X coefficient developed in the preceding subsection is highly conservative since it imposes causality directly. The class 2 coefficient is somewhat less conservative because it requires a clear time from $t = 0$ to the first causal disturbance. Experience in using it on many problems corroborates its usefulness, however. The class 1 coefficient should be used only with caution. It assumes a clear time of $-L/c$, independent of \bar{r}, \bar{r}' , where L is the maximum dimension of the object.

A second potential test procedure on a coupling coefficient form is simply to compare its results with the conservative class X form. One must be cautious to include representative incident angles and spectra of the excitation in conducting this test, however.

The Step B3 above is the point at which one must exercise proverbial "engineering judgment." Obviously, in dealing with graphical data such as those in Figure 2.6, the decisions are not clear-cut. We use the qualitative plot of a time domain inverse kernel in Figure 2.10 to point out the features which one might expect in such a plot. Hopefully, the most prominent feature will be the expected causal disturbance arriving at $t = |\bar{r} - \bar{r}'|/c$. The clear time region, if present, must be an approximation to a zero-weight distribution. In Figure 2.10 we see depicted oscillations which are significant in magnitude compared with the proper disturbance. We note, however, that the waveform with which this function is convolved varies slowly compared with these oscillations if it is bandlimited appropriately for the number of poles used. Thus, in an approximate sense, these ripples cancel among themselves

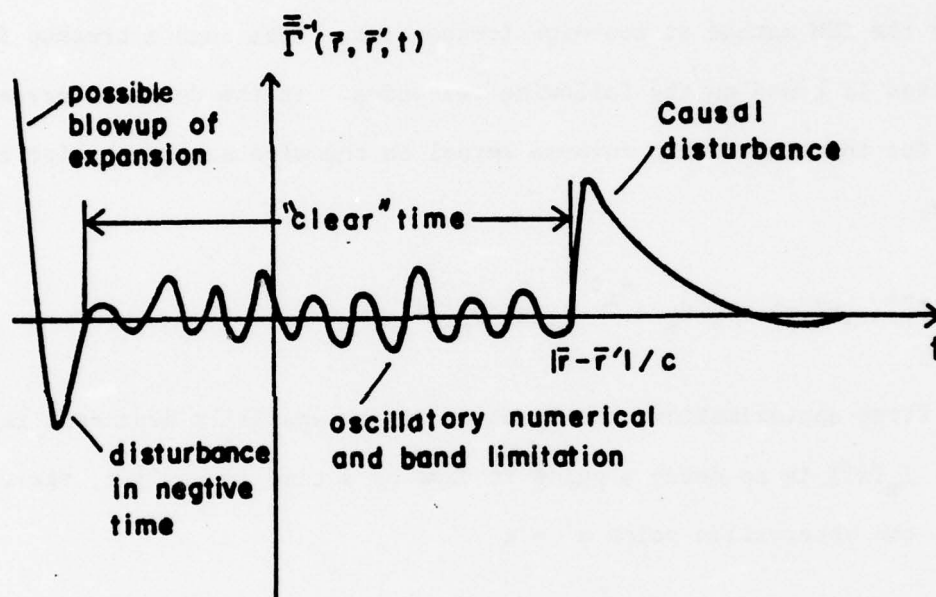


Figure 2.10. Qualitative representation of a time domain inverse kernel plot showing the principal features which have bearing on the applicability of the kernel.

in the convolution. The acausal region of the distribution may be marked by one of two features: either a prominent disturbance prior to $t = |\bar{r} - \bar{r}'|/c$ or a "blowup" of the expansion. This blowup is expected at some point in negative time, because in negative time, the real parts of the exponents in the series are positive (the result of the negative real part of the pole times a negative time).

Another breakup of the representation to which one should be sensitive in studying $\bar{\Gamma}^{-1}$ is that which is expected from attempting to apply the SEM method at too high frequencies. That such a breakup is expected is based on the following reasoning. In the dyadic representation for the time domain inverse kernel on the wire scatterer, for example,

$$\Gamma^{-1}(x, x', t) = \sum \beta_m e^{s_m t} J_m(x) J_m(x') .$$

To a first approximation, the function of the spatially dependent factor $J_m(x) J_m(x')$ is to delay a pulse in time by a time $|x - x'|/c$, viz., if at the observation point $x' = x$

$$\Gamma^{-1}(x, x, t) = \sum_{m=0}^M A_m e^{s_m t} = f(t) ,$$

at a point separated from the observation point

$$\Gamma^{-1}(x, x', t) \approx f(t - |x - x'|/c) = \sum_{m=0}^M A_m e^{-s_m |x - x'|/c} e^{s_m t} .$$

It is seen that if M is increased, the factors $\exp[-s_m |x - x'|/c]$ grow since $\text{Re } s_m$ becomes more negative as m increases. Further, the larger

a pole in magnitude, the more subject it is to numerical error. This error is magnified due to the exponential dependence on the s_m . This error will manifest itself as a blowup in the oscillations in the clear-time region of the inverse kernel. The net effect is a numerical limitation on the time resolution relative to body size in a given SEM solution.

2.6 Conclusions

In this chapter we present the fundamental formalism of the singularity expansion method. Well-known theory relating the asymptotic behavior of a function in the transform domain and the support of its inverse in the time domain is brought to bear on the SEM formulation. The significant conclusions are summarized in the following list.

1. The support of the time domain inverse kernel to an electromagnetic integral equation is dependent on the asymptotic behavior of the transform domain form of the inverse kernel. This asymptotic behavior, and hence the support, depend, in general, on the source and observation points.
2. The dependence of the support on the source and observation points affects the coupling coefficient form applicable to the formulation for a particular problem.
3. In a numerically treated SEM problem, we have only a limited amount of pole data available. These data are adequate to form the components of an approximate solution by way of the transform domain inverse kernel. It is not adequate to provide asymptotic behavior of the inverse kernel.

4. We must turn to other information in order to gain this asymptotic information which is necessary to construct correctly the time domain SEM solution, in particular, the coupling coefficients.
5. The observation of a numerically computed time domain inverse kernel allows us to choose a coupling coefficient form consistent with causality.

By example, it is seen that for at least one problem, that of a straight-wire scatterer, direct application of the class 1 coupling coefficient form introduces acausal contributions into the solution. This observation is consistent with the experiences of Tesche and of Wilton and Umashanker in attempts to apply class 1 coefficients to numerical SEM solutions [22], [23]. Further, Van Blaricum and, independently, Poggio have observed that in applying Prony's method to electromagnetics an exponential series alone cannot describe the time dependence of observed waveforms while the driving field is present [24], [25]. This observation, in effect, recognizes a breakdown in the class 1 coupling coefficient SEM form for these problems. The class 1 form relegates all time dependence to the exponential factors in the singularity expansion. It indicates that other terms in the representation must indeed be time dependent. This too, is consistent with the observation in this chapter that, at least for some problems, a coupling coefficient which varies with time during the passage of the incident wave is required. A second potential source of the additional time variation is an entire function contribution during the passage of the wave.

The discussion in this chapter is based on the objective of writing the SEM representation for a time domain solution in terms of the residue series alone. We observe, by example, that for some structures, the class 1

coupling coefficient introduces an acausal contribution to the solution. Baum [1] observes correctly that in the Mittag-Leffler representation for a meromorphic function an entire function with zeros at the poles of $\tilde{\Gamma}^{-1}$ may be added and subtracted so as to modify the asymptotic behavior of the pole series portion of the representation. The class 1 form results for the series by such a manipulation, viz., from (2.9) and (2.13) write

$$\tilde{\Gamma}^{-1}(\bar{r}, \bar{r}', s) = \sum_m \beta_m (s - s_m)^{-1} M_m(\bar{r}) C_m(\bar{r}') + \tilde{\Gamma}_e^{-1}(\bar{r}, \bar{r}', s) \quad , \quad (2.44)$$

where $\tilde{\Gamma}_e^{-1}$ is an entire function in s . Then add and subtract an entire function with zeros at $s = s_m$ to obtain

$$\begin{aligned} \tilde{\Gamma}^{-1}(\bar{r}, \bar{r}', s) &= e^{-s(t' - \hat{p} \cdot \bar{r}')} \sum_m \beta_m (s - s_m)^{-1} e^{s_m(t' - \hat{p} \cdot \bar{r}')} M_m(\bar{r}) C_m(\bar{r}') \\ &\quad + \tilde{\Gamma}_e^{-1}(\bar{r}, \bar{r}', s) \\ &= \tilde{\Gamma}_\Sigma^{-1}(\bar{r}, \bar{r}', s) + \tilde{\Gamma}_e^{-1}(\bar{r}, \bar{r}', s) \quad , \end{aligned} \quad (2.45)$$

where $\tilde{\Gamma}_e^{-1}$ is the modified entire function. Now $\tilde{\Gamma}_\Sigma^{-1}(\bar{r}, \bar{r}', s)$ is a unique function and its asymptotic form is the same whether it be represented by (2.44) or (2.45). However, if we invert the product of $\langle \tilde{\Gamma}_\Sigma^{-1}(\bar{r}, \bar{r}', s), E(\bar{r}', s) \rangle$ from (2.45) we have the superposition of the series contribution and the entire function contribution. Then, treating the series inversion termwise, we effectively have introduced the class 1 asymptotic exponent, $T_L = \hat{p} \cdot \bar{r}' + t'$, to each term in the series. Thus, a class 1 form results for the series in the time domain:

$$\bar{J}(\bar{r}, t) = \bar{J}_\Sigma(\bar{r}, t) + \bar{J}_e(\bar{r}, t) \quad , \quad (2.46)$$

with \bar{J}_Σ a current expanded by the class 1 expansion of (2.36) and (2.39). The examples of the transmission line demonstrate that J_Σ potentially includes acausal contributions. Therefore, the manipulation between (2.44) and (2.45) necessarily introduces a contribution in $\bar{J}_e(\bar{r}, t)$ which cancels the acausal portion of \bar{J}_Σ . The following one-term example illustrates the principle. Let

$$\tilde{f}(s) = \frac{1}{s - s_0} \leftrightarrow f(t) = u(t) e^{s_0 t}.$$

The partitioning below results in a sum form:

$$\tilde{f}(s) = e^{-T_0(s_0-s)} / (s - s_0) + \left[1 - e^{-T_0(s_0-s)} \right] / (s - s_0).$$

The second term is an entire function. Termwise inversion of this expression yields

$$f(t) = u(t + T_0) e^{s_0 t} - e^{s_0 t} [u(t + T_0) - u(t)] = u(t) e^{s_0 t}.$$

In this example $\tilde{f}(s)$ is the transform of a "causal" function. Modifying the asymptotic form pole term allows the premature application of its inverse transform but at the expense of an additive canceling term.

By considering the net asymptotic form of $\tilde{f}^{-1}(\bar{r}, \bar{r}', s)$ as in the preceding sections, we obtain a time domain representation involving only a pole series but with a coupling coefficient of the class 2 or class X type which is time dependent. By partitioning the asymptotic behavior between the series and entire functions as in (2.45), we gain a class 1 pole series form at the expense of a required entire function to cancel any acausal behavior present in the class 1 pole series.

3. DETERMINATION OF THE SEM REPRESENTATION FOR A RECTANGULAR APERTURE

3.1 Introduction

This chapter describes the numerical determination of the SEM quantities of poles, natural modes, coupling vectors and normalization constants. The determination is based on a method of moments numerical solution to the integrated E-field integral equation form for the dual problem of a rectangular plate [3]. These coupled integral equations have a form counterpart to the Hallén integral equation for a linear antenna.

In Section 3.2 we develop the integral equations for the problem for complex frequencies and develop the symmetry relationships which exist between the natural modes for the problem. The symmetry provides a significant computational benefit in the numerical solution of the integral equation.

Section 3.3 describes the numerical solution procedure based on the method of moments used in solving the integral equations. Other more routine computational considerations are discussed there, too. In attacking a two-dimensional SEM problem numerically, it is essential to be mindful of computational efficiency.

Section 3.4 presents the results of some numerical checks used to validate the solution procedure and the programming thereof. These checks include convergence studies for the poles.

Section 3.5 describes the pole search strategy used in obtaining the SEM data for the aperture. The use of argument number in pole location is discussed from an applications point of view.

3.2 Thin-Plate Integral Equation Formulation for Complex Wavenumber

3.2.1 The integral equations for complex frequency

Rahmat-Samii and Mittra [3] give an integral equation formulation for the rectangular plate subject to time-harmonic excitation. Their results may be directly extended to the complex wavenumber case. That is, for the geometry in Figure 3.1 with $\exp[st]$ time dependence, $s = \sigma + j\omega$ complex, and an incident plane-wave magnetic field component

$\vec{H}^i = [H_{ox}^i \hat{a}_x + H_{oy}^i \hat{a}_y + H_{oz}^i \hat{a}_z] \exp[s\hat{p} \cdot \vec{r}/c]$, the following coupled integral equations result:

$$\begin{aligned} \int_{-L/2}^{L/2} \int_{-w/2}^{w/2} \begin{Bmatrix} J_x(x,y) \\ J_y(x,y) \end{Bmatrix} K(x,y|x',y') dx' dy' &= \frac{j4\pi c}{sp_z} \begin{Bmatrix} H_{oy}^i \\ 1 \\ -H_{ox}^i \end{Bmatrix} \exp[s(p_x x + p_y y)/c] \\ &+ \frac{\pi c}{s} \begin{Bmatrix} -1 \\ j \end{Bmatrix} \sum_{n=-\infty}^{\infty} C_n [j^{n+1} \exp[j(n+1)\phi] J_{n+1}(-js\rho/c) \\ &+ \begin{Bmatrix} 1 \\ -1 \end{Bmatrix} j^{n-1} \exp[j(n-1)\phi] J_{n-1}(-js\rho/c)] \end{aligned} \quad (3.1)$$

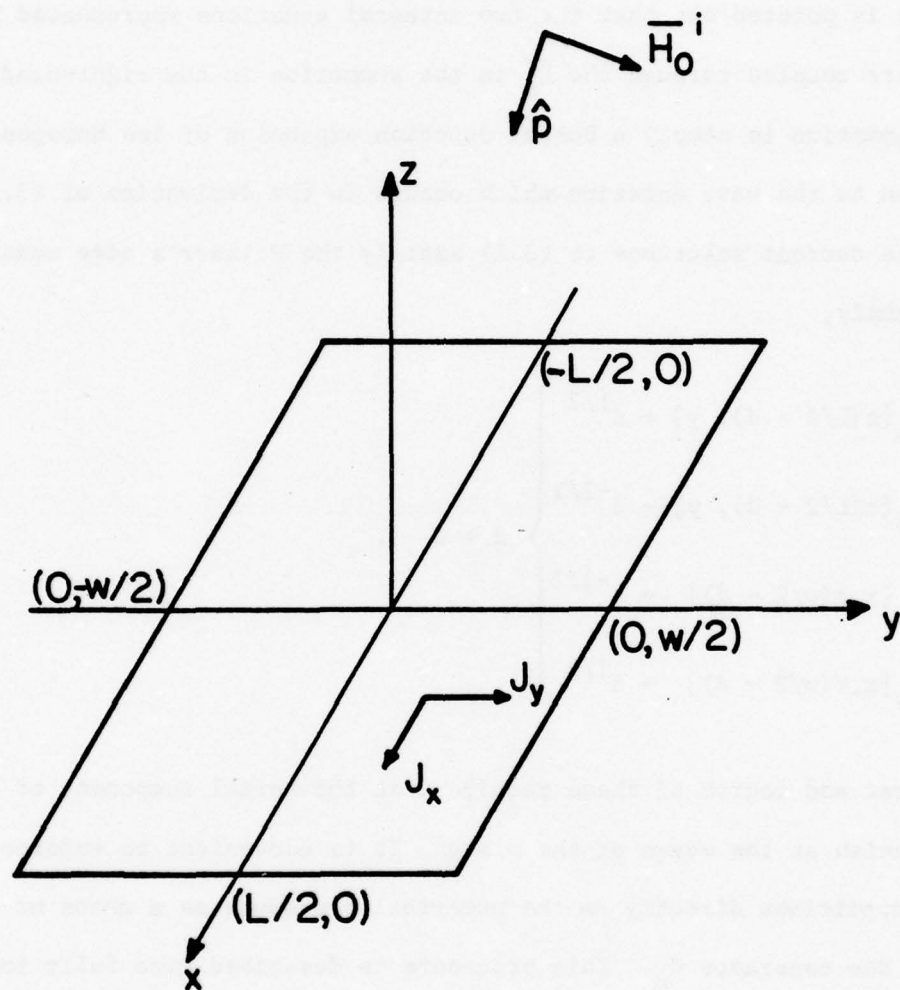
The kernel is given by

$$K(x,y|x',y') = \exp[-sR/c]/R \quad (3.2)$$

with

$$R = [(x - x')^2 + (y - y')^2]^{1/2}$$

The propagation is in the direction of the unit vector \hat{p} . The $J_x(x,y)$



Aspect ratio = w/L

Figure 3.1. Geometry of the rectangular plate.

and $J_y(x,y)$ denote the respective x and y components of current on the plate; $J_n(\zeta)$ denotes the Bessel function of the first kind; C_n are unknown constants; c is the velocity of light; and (ρ, ϕ) are the polar coordinates for the point (x,y) on the plate. Equation (3.1) holds for $x \in (-L/2, L/2)$ and $y \in (-w/2, w/2)$, and $z = 0$.

It is pointed out that the two integral equations represented by (3.1) are coupled through the C_n in the summation in the right-hand side. This summation is simply a Bessel function expansion of the homogeneous solution to the wave equation which occurs in the derivation of (3.1).

The current solutions to (3.1) satisfy the Meixner's edge condition [2]; namely,

$$\left. \begin{aligned} J_x[\pm(L/2 - d), y] &\rightarrow d^{1/2} \\ J_y[\pm(L/2 - d), y] &\rightarrow d^{-1/2} \\ J_x[x, \pm(w/2 - d)] &\rightarrow d^{-1/2} \\ J_y[x, \pm(w/2 - d)] &\rightarrow d^{1/2} \end{aligned} \right\} d \rightarrow 0 \quad . \quad (3.3)$$

The first and fourth of these require that the normal component of current vanish at the edges of the plate. It is convenient to enforce these conditions directly in the numerical procedure as a means of evaluating the constants C_n . This procedure is described more fully in Section 3.3.

3.2.2 Symmetry conditions for the natural mode currents

The natural frequencies of (3.1) occur when the complex frequency s is such that there are nontrivial J_x and J_y and the accompanying C_n

which satisfy (3.1) for $\bar{H}^1 = 0$. Such J_x and J_y solutions are natural mode current solutions for the rectangular plate, and the concomitant value of s is a pole of the plate. The vanishing of incident wave dependence gives rise to symmetry in the integral equations. By discerning the symmetry relations a priori and bringing them to bear upon solution procedures, one gains significant computational savings in the numerical solution for poles and natural modes.

The excitation-free form of (3.1) is

$$\int_{-L/2}^{L/2} \int_{-w/2}^{w/2} J_x K(x, y | x', y') dx' dy' = \frac{j\pi c}{s} \sum_{n=-\infty}^{\infty} C_n \left\{ j^{n+1} \exp[j(n+1)\phi] J_{n+1}(-j s \rho / c) \right. \\ \left. + j^{n-1} \exp[j(n-1)\phi] J_{n-1}(-j s \rho / c) \right\} \quad (3.4a)$$

and

$$\int_{-L/2}^{L/2} \int_{-w/2}^{w/2} J_y K(x, y | x', y') dx' dy' = \frac{\pi c}{s} \sum_{n=-\infty}^{\infty} C_n \left\{ j^{n+1} \exp[j(n+1)\phi] J_{n+1}(-j s \rho / c) \right. \\ \left. - j^{n-1} \exp[j(n-1)\phi] J_{n-1}(-j s \rho / c) \right\}. \quad (3.4b)$$

By using the symmetry of the Bessel function with respect to order, expanding the exponentials by way of Euler's identity, and appropriately adjusting the indices, one arrives at the following equations after some manipulation.

$$\int_{-L/2}^{L/2} \int_{-w/2}^{w/2} J_x K dx' dy' = \frac{j\pi c}{s} \sum_{n=0}^{\infty} \left\{ j^{n+1} d_n^+ [\cos(n+1)\phi J_{n+1}(-j s \rho / c) \right. \\ \left. - u_{n-1} \cos(n-1)\phi J_{n-1}(-j s \rho / c)] - j^n d_n^- [\sin(n+1)\phi J_{n+1}(-j s \rho / c) \right. \\ \left. - u_{n-1} \sin(n-1)\phi J_{n-1}(-j s \rho / c) \right\} \quad (3.5a)$$

and

$$\int_{-L/2}^{L/2} \int_{-w/2}^{w/2} J_y K dx' dy' = \frac{j\pi c}{s} \sum_{n=0}^{\infty} j^{n+1} d_n^+ [\sin(n+1)\phi J_{n+1}(-j\sigma\rho/c) + u_{n-1} \sin(n-1)\phi J_{n-1}(-j\sigma\rho/c)] + j^n d_n^- [\cos(n+1)\phi J_{n+1}(-j\sigma\rho/c) + u_{n-1} \cos(n-1)\phi J_{n-1}(-j\sigma\rho/c)] \quad , \quad (3.5b)$$

where

$$d_n^{\pm} = C_n \pm C_{-n}$$

and

$$u_n = \begin{cases} 1, & n \geq 0 \\ 0, & n < 0 \end{cases} .$$

It is noted that the d_n^+ multiply terms containing cosine functions in the J_x equation, while they multiply terms containing sine functions in the J_y equation. The situation is reversed for the d_n^- .

Because of the symmetry properties of the kernel, the integral operator on the left-hand sides of (3.5) produces a function whose symmetry character is identical to that of the current on which it operates. Then, for a given current symmetry, only part of the d_n^{\pm} on the right-hand side may be nonzero because of the symmetries possessed by the trigonometric terms. Thus, the respective symmetries for J_x and J_y , which are compatible, and the surviving terms in the right-side series may be discerned by (1) postulating a symmetry for J_x , (2) determining from (3.5a) which right-hand-side terms survive so as to be

compatible with the J_x symmetry, (3) observing in (3.5b) the variation of the terms in the right-hand side which have nonzero coefficients, and (4) determining the J_y symmetry conditions from the symmetry observed in the right-hand side and thus compatible with the postulated J_x symmetry conditions.

For example, if J_x is symmetric with respect to the y-axis and antisymmetric with respect to the x-axis, only $\sin(n+1)\phi$ terms with n even are compatible in (3.5a). Thus, only d_n^- , n even, may be nonzero. In the right-hand side of (3.5b), the coefficients multiply $\cos(n+1)\phi$ terms with n even. These cosines sum to functions which are antisymmetric with respect to the y-axis and symmetric with respect to the x-axis. Stated mathematically, if

$$J_x(x,y) = J_x(-x,y) \quad (3.6a)$$

and

$$J_x(x,y) = -J_x(x,-y) \quad , \quad (3.6b)$$

then

$$d_n^+ = 0, \quad \text{for all } n \quad , \quad (3.6c)$$

$$d_n^- = 0, \quad n \text{ odd} \quad , \quad (3.6d)$$

and

$$J_y(x,y) = -J_y(-x,y) \quad (3.6e)$$

$$J_y(x,y) = J_y(x,-y) \quad . \quad (3.6f)$$

These vector symmetries are in accord with the general symmetry relations given by Baum [27]. The information in (3.6) may be used to reduce the complexity of the integral equations (3.4), viz., by (3.6a,b,e,f) the range of each integration may be halved while by (3.6c,d) the zero terms of the right-hand side are known a priori:

$$\int_0^{L/2} \int_0^{w/2} J_x K^{+-}(x,y|x',y') dx' dy' = \frac{\pi c}{s} \sum_{\substack{n=0 \\ n \text{ even}}}^{\infty} d_n^- j^{n-1} [\sin(n+1)\phi J_{n-1}(-j s \rho / c) - \sin(n-1)\phi J_{n-1}(-j s \rho / c)] \quad (3.7a)$$

and

$$\int_0^{L/2} \int_0^{w/2} J_y K^{+-}(x,y|x',y') dx' dy' = \frac{\pi c}{s} \sum_{\substack{n=0 \\ n \text{ even}}}^{\infty} j^{n+1} d_x^- [\cos(n+1)\phi J_{n+1}(-j s \rho / c) + u_{n-1} \cos(n-1)\phi J_{n-1}(-j s \rho / c)] \quad (3.7b)$$

where

$$\begin{aligned} K^{+-}(x,y|x',y') &= K(x,y|x',y') - K(x,y|-x',y') \\ &\quad + K(x,y|x',-y') - K(x,y|-x',-y') \end{aligned} \quad (3.8a)$$

and

$$\begin{aligned} K^{-+}(x,y|x',y') &= K(x,y|x',y') + K(x,y|-x',y') \\ &\quad - K(x,y|x',-y') - K(x,y|-x',-y') \end{aligned} \quad (3.8b)$$

For subsequent reference

$$\begin{aligned}
K^{++}(x,y|x',y') &= K(x,y|x',y') + K(x,y|-x',y') \\
&+ K(x,y|x',-y') + K(x,y|-x',-y')
\end{aligned} \tag{3.8c}$$

and

$$\begin{aligned}
K^{--}(x,y|x',y') &= K(x,y|x',y') - K(x,y|-x',y') \\
&- K(x,y|x',-y') + K(x,y|-x',-y')
\end{aligned} \tag{3.8d}$$

are defined as well. Equations (3.7) are enforced for $z = 0$, $x \in (0, L/2)$ and $y \in (0, w/2)$.

Table 3.1 summarizes the four symmetry cases which are derived as in the foregoing discussion. By means of this table, four integral equation pairs can be constructed in the spirit of (3.7) by replacing the kernels in (3.7) with the appropriate kernels from the table and retaining only the nonvanishing terms in the series expansion.

Figure 3.2 depicts qualitatively the respective modal current distributions for the lowest frequency natural resonance exhibiting each symmetry.

3.3 The Numerical Model

3.3.1 Discretization of the integral equations

The integral equation pair of the form (3.7) for each of the four symmetry cases can be discretized by the method of moments. In the work reported here, two-dimensional, subsectionally constant expansion functions were used with collocation testing. The zoning scheme is represented in Figure 3.3.

The unknown currents J_x and J_y were expanded in piecewise constant functions as in [3] with subsectioning of the form given in Figure 3.3.

TABLE 3.1
COMPATIBLE CURRENT SYMMETRY FEATURES

| J_x | | | | | J_y | | | |
|--------------------|--------------------|----------|-----------------------|-----------------|-----------------------|----------|--------------------|--------------------|
| Sym. w.r.t. x-axis | Sym. w.r.t. y-axis | Kernel | Compatible Trig. Fns. | Coefs. $\neq 0$ | Compatible Trig. Fns. | Kernel | Sym. w.r.t. x-axis | Sym. w.r.t. y-axis |
| sym | sym | K^{++} | $\cos 2n\phi$ | d_{2n+1}^+ | $\sin 2n\phi$ | K^{--} | anti | anti |
| sym | anti | K^{+-} | $\cos(2n+1)\phi$ | d_{2n}^+ | $\sin(2n+1)\phi$ | K^{-+} | anti | sym |
| anti | sym | K^{-+} | $\sin(2n+1)\phi$ | d_{2n}^- | $\cos(2n+1)\phi$ | K^{+-} | sym | anti |
| anti | anti | K^{--} | $\sin 2n\phi$ | d_{2n+1}^- | $\cos 2n\phi$ | K^{++} | sym | sym |

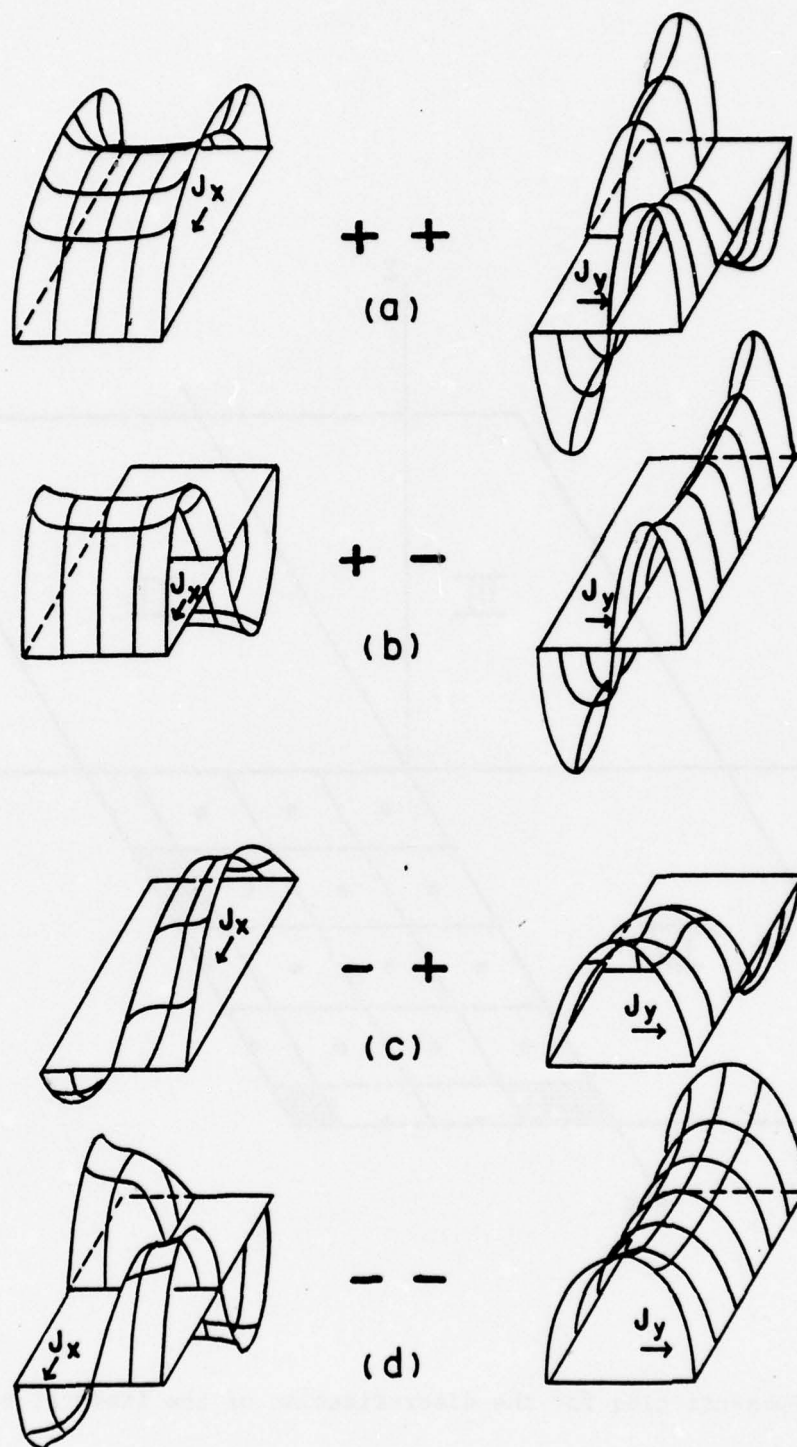


Figure 3.2. Lowest-order natural mode current pairs for each of the symmetry cases, (a) J_x symmetric w.r.t. x-axis and symmetric w.r.t. y-axis, (b) symmetric-antisymmetric, (c) antisymmetric-symmetric, and (d) antisymmetric-antisymmetric.

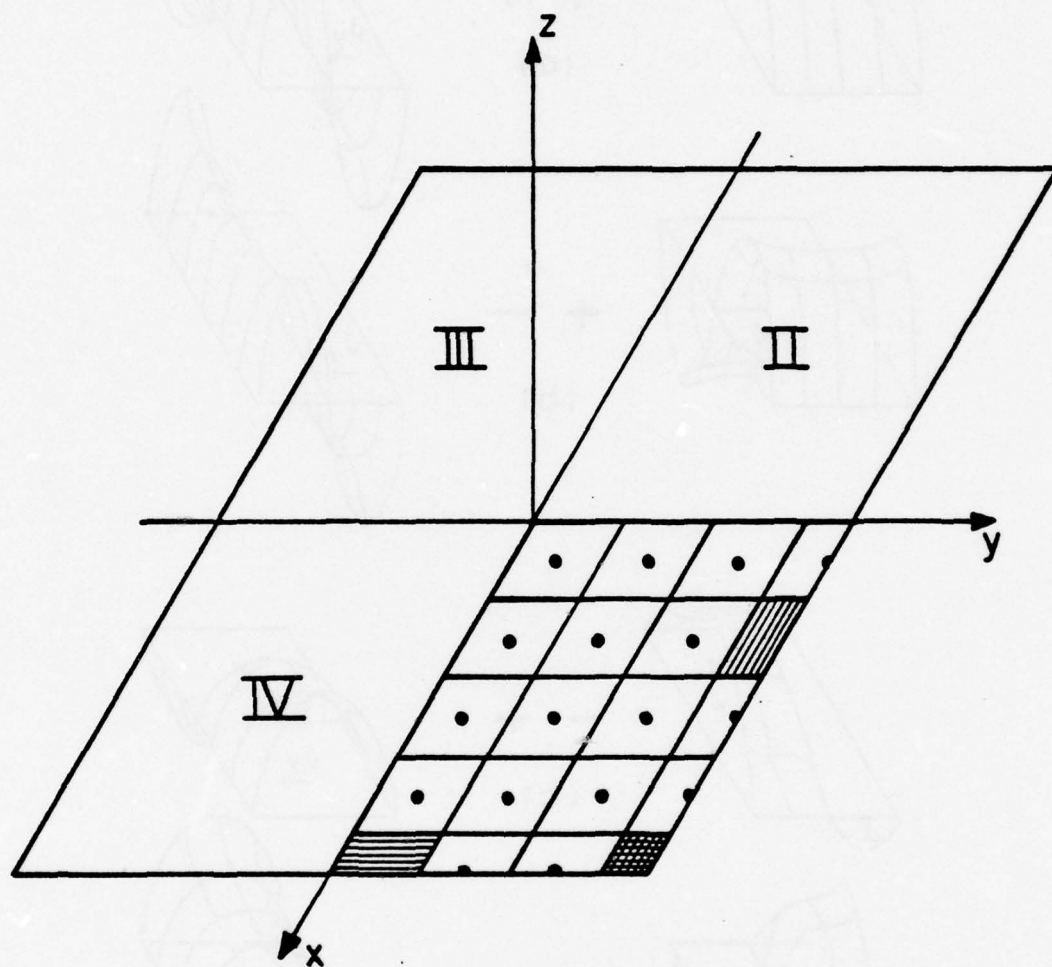


Figure 3.3. Subsectioning for the discretization of the integral equations.

Notice that half-width patches are used at the edges of the plate so that match points lie precisely on the edge of the plate. The half-width pulse has proved useful in realizing the actual electrical size of a body in one-dimensional problems [28].

The boundary condition $J_{\text{norm}} = 0$ must be enforced on selected patches at the edge of the plate as discussed in [3]. Concomitantly, only as many d_n^+ 's are retained in the right-hand-side summation in (3.7) as there are current values preassigned to zero. The shaded patches in Figure 3.3 indicate the selection of patches where a current component is preassigned a zero value. At the corner patch, both components are preassigned zero values. By assigning one match point per expansion patch and by retaining one series expansion term for each current value preassigned in each of the two integral equations, we obtain a square system of linear equations. The truncated summation is taken to the left-hand side so that a homogeneous system results. The matrix organization used to represent these equations is given by the partitioned matrix equation

$$\begin{bmatrix} M_x(s) & 0 \\ 0 & M_y(s) \end{bmatrix} \begin{bmatrix} J_x \\ J_y \\ d \end{bmatrix} = \begin{bmatrix} 0 \end{bmatrix} \quad (3.9)$$

The symbols are as follows. The matrix $[M_x]$ is the moment matrix for the J_x integral equation as given in (3.7a) but with the kernel symmetry appropriate to the mode symmetry for which an individual solution is being conducted. The matrix $[M_y]$ is the J_y moment matrix as in (3.7b) with the kernel symmetry compatible with that of the J_x kernel. The

coupling enters through $[M_z]$. This matrix is formed by the negative of sine-Bessel function products on the right-hand sides of (3.7a,b) which survive under the symmetry considered. Sufficient terms are taken in the series to render a square system after entries for the edge currents which are preassigned to zero are deleted from moment matrices.

In using this integral equation in the real frequency domain, Rahmat-Samii and Mittra experienced a numerically unstable matrix if the zero current edge condition was enforced at every zone on the edge of the plate. This difficulty was attributed to redundancy in the imposition of the boundary condition and was corrected when the condition was enforced only for every second or third zone at the edge. The edge current zones in between which were left undetermined attained a value of zero within limits of numerical error in the course of the numerical solution.

The procedure of preassigning currents at preselected edge zones proved to fail when it was applied in the SEM pole search in the complex s -plane. It was observed that the moment matrix had zeros in the complex plane whose associated homogeneous solution did not approximate zero for the zones in between specified patches. The procedure of specifying at every edge zone that the normal current component vanish provided physically consistent solutions.

The matrix in (3.9) is a function of the complex frequency s . An SEM "pole" or complex resonance occurs when this composite matrix has a zero determinant. It follows directly from the analyticity of the kernels of the original integral equations (3.2) that the determinant is an analytic function of s throughout the whole of the complex s -plane. The Muller method for searching for roots of nonlinear systems

of equations provides an efficient algorithm [29] for systematically searching for the values of s for which the determinant vanishes. Many evaluations of the determinant are required in the course of the iteration to locate a zero. This places a premium on computational efficiency in the evaluation of the matrix and its determinant. The next subsection discusses the means taken to attain computational efficiency.

3.3.2 Algorithmic considerations in evaluating the system determinant

Some considerations taken into account in generating the system matrix and evaluating its determinant efficiently are discussed in this section. Since these two operations must be repeatedly carried out for many values of s in the course of determining the natural frequencies of the plate, it is essential that clean, efficient computer programming and coding be used so that execution of the program will be affordable. The volume of code in the algorithms is consistently compromised toward a larger size in order to meet the following two time-efficient objectives:

1. Avoidance of calculating the same quantity twice; and
2. Avoidance of logical decisions, particularly those which might be imbedded in loops.

The program is discussed in the context of the following major segments:

1. Computation of an "interaction matrix";
2. Construction of the nonzero submatrices of the system matrix from the interaction matrix;
3. Computation of the series terms' submatrix; and
4. Determinant evaluation.

The major contribution to the elimination of redundant calculations is the one-time computation of an "interaction matrix" which is made up of the individual kernel integral terms from (3.2) for all argument combinations which occur in the computation. The subsequent program step then picks, by subscript, entries from this matrix and constructs the appropriate kernel from one of Equations (3.8) according to the symmetry conditions being solved. This procedure can be viewed in terms of the layout given in Figure 3.4a. The terms in the interaction matrix are those evaluated for the match point as shown in the lower left with the source patches indexed over the entire plate to generate the matrix. Thus, all geometric relationships which occur in the kernel terms are encompassed in the calculation. Note that all source patches are full patches for this calculation. The effect of half patches at the edges is accounted for by weighting by a factor of $1/2$ the edge contributions. The kernel integral appropriate to the symmetry is constructed by summing with correct signs the appropriate elements from the matrix. Figure 3.4b gives an example of the four source patches entering into one kernel integral.

Differing degrees of sophistication are required in the calculation of the interaction terms depending on the spacing of the patches for which an interaction is being calculated. For the self patch, i.e., the patch in which the match point resides, the integration of the kernel must be performed analytically because of the integrable singularity in the kernel there. For the patches adjacent to the patch containing the match point, the kernel is a rapidly varying but well-behaved function. The integration over these patches is evaluated numerically by a polynomial approximation. For patches further separated, the kernel

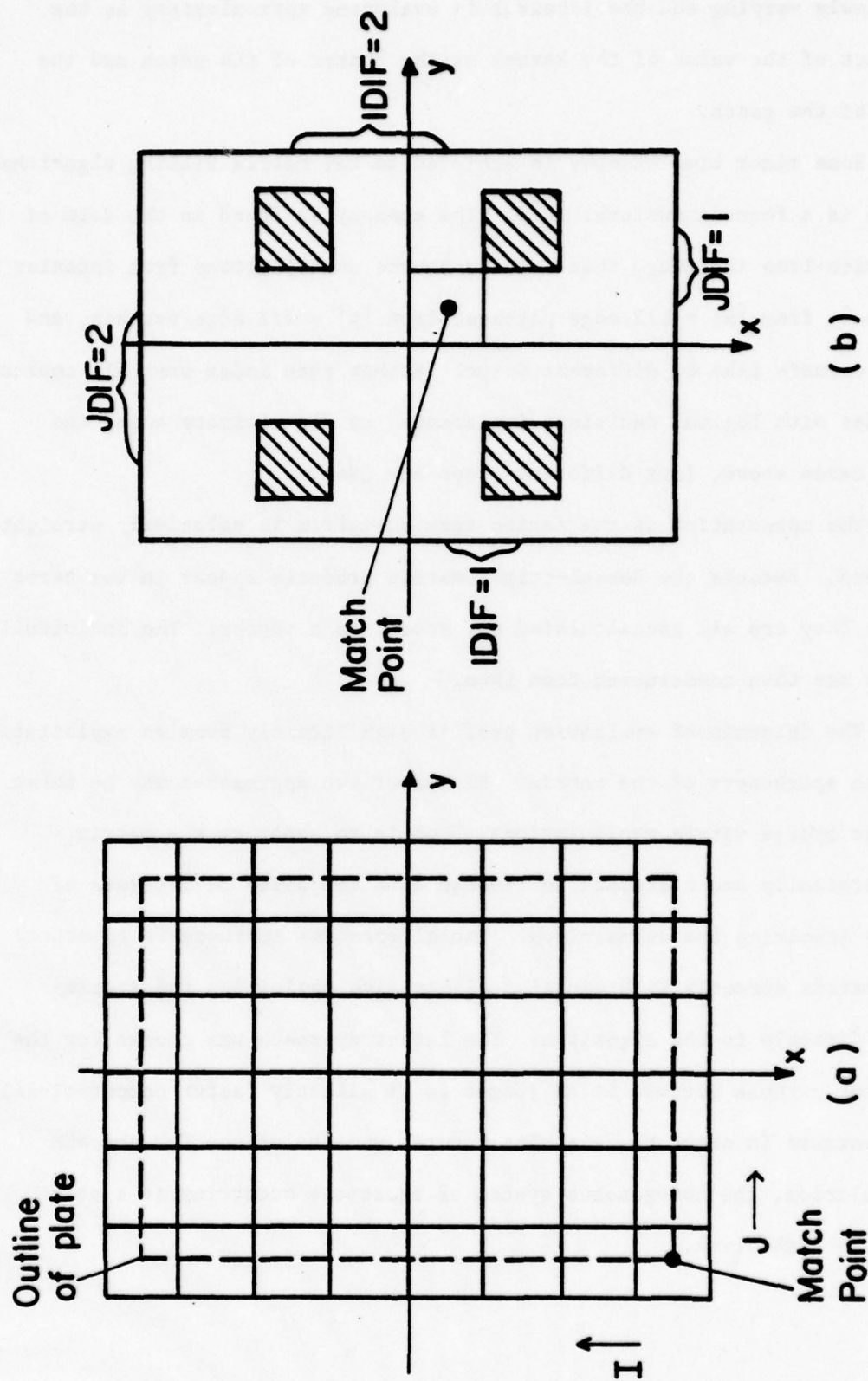


Figure 3.4. (a) Conceptual zoning for calculation of the interaction matrix, (b) example of the four interaction contributions to a single source term.

is slowly varying and the integral is evaluated approximately as the product of the value of the kernel at the center of the patch and the area of the patch.

Some minor time economy is achieved in the matrix filling algorithm, which is a four-dimensional loop. The economy is found in the form of decision-free indexing, that is, the source contributions from interior patches, from $|x| = L/2$ edge patches, from $|y| = w/2$ edge patches, and from corners take on different forms. Rather than index over all source patches with logical decisions implemented to discriminate among the four cases above, four different loops are used.

The computation of the series term submatrix is relatively straightforward. Because the Bessel-trigonometric products appear in two terms each, they are all precalculated and stored in a vector. The individual terms are then constructed from them.

The determinant evaluation profits significantly from an exploitation of the sparseness of the matrix. Either of two approaches may be taken to the sparse matrix manipulations. One is to separate the matrix algebraically and calculate an inverse as a composite of inverses of terms involving the submatrices. The alternative approach is to attack the matrix directly with Gaussian elimination exploiting the sparseness directly in the algorithm. The latter approach was chosen for the present purpose because it is judged to be slightly faster computationally and because in order to determine natural mode solutions for the SEM formulation, the homogeneous system of equations occurring at a pole must be backsolved.

3.3.3 Numerical evaluations of natural modes, coupling vectors, and normalization constants

In addition to the poles, the associated coupling vectors and natural mode vectors defined by (2.11) and the normalization constants defined by (2.13) form the SEM description of a given problem. In a method of moments solution, these are calculated in a discretized fashion and are "one-time" calculations for each pole. We need not be quite so mindful of computation costs as we are in the matrix/determinant computation which is used iteratively.

The natural mode computation is a straightforward one once a pole is located. The Gaussian elimination with maximum pivoting used to calculate the determinant in the course of pole location results in a triangularized matrix which has a zero in the lower-right position when a zero determinant is computed. Thus, the last triangularized matrix upon return from the zero search iteration may be backsolved by assigning a value to the last element in the vector of unknowns and then backsolving the system of equations systematically. The present work applies this procedure using the sparse matrix format so as to be compatible with the determinant evaluation algorithm discussed above.

The coupling vectors are found in a similar manner except that the transpose conjugate of the moment matrix must be triangularized and backsolved for the adjoint solution. The transpose conjugate is that of Equation (3.9). The benefit of sparseness is not as great for the transposed form because the coupling there appears in the lower rows of the matrix. The moment matrix can be recalled from storage or recomputed and the transpose conjugate formed in the composite format of (3.9). This matrix is triangularized and backsolved with elementary routines.

The normalization constant in (2.13) is computed from the s-derivative of the moment matrix at the pole and the vectors already computed. The s-derivative may be formed by analytical differentiation of the matrix components directly. This amounts to forming the matrix elements as before with the kernels and Bessel functions replaced by their s-derivatives. The double inner product in (2.13) becomes a straightforward matrix-vector product in the method of moments formulation.

3.4 Numerical Checks and Convergence

3.4.1 Pole convergence in the thin-strip limit

Initial tests on the accuracy of the model were made for a rectangular strip with a shape ratio $w/L = 1/10$. Such a strip has an approximate equivalent dipole whose diameter-to-length ratio is $1/10\pi$.

Figure 3.5 gives the results of pole determinations for the first two poles for various numbers of pulses in the expansion of the current. The strip was zoned with one pulse across a quadrant. The numbers indicated in the figure are N_X , the numbers of pulses along the longitudinal direction of a quadrant. The differences are small for increasing numbers of pulses. The $N_X = 6$ results for the second pole show some departure from the trend established by the results for $N_X = 4$ and $N_X = 5$. This is attributable to the fact that the matrix is on the brink of numerical instability for $N_X = 6$. The results for $N_X = 7$, which are not shown, are observed to be meaningless because of the instability manifested.

For comparison purposes, the first two poles for an equivalent cylinder (one whose circumference equals the strip width) are given as computed by Tesche [14]. The equivalent radius taken is, of course, an approximation. The comparison is observed to be favorable, within the expectations concomitant with this approximation.

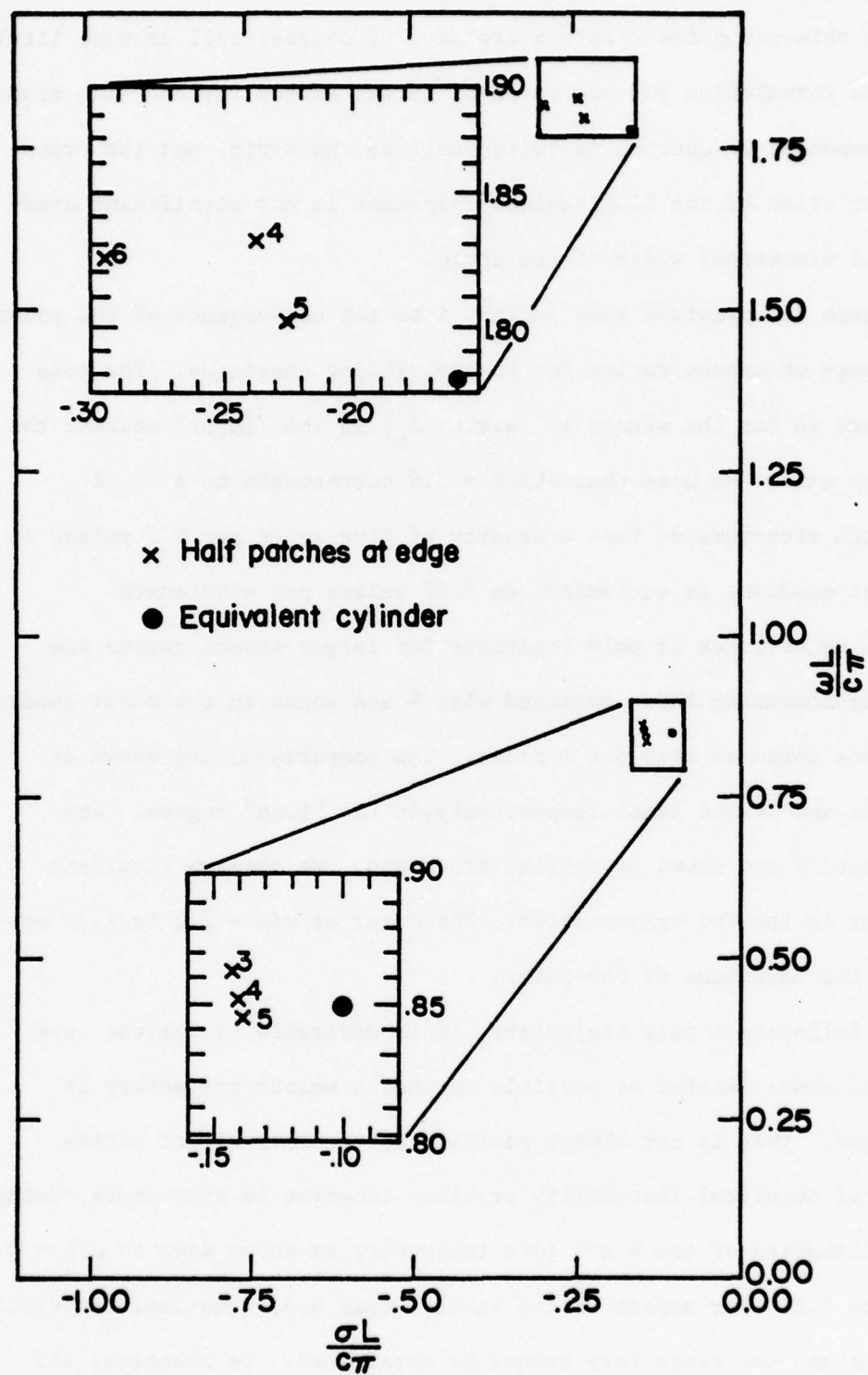


Figure 3.5. Calculated pole locations for thin strip for varying numbers of zones in the x-direction (cylinder results from Tesche [6]).

3.4.2 Pole convergence for larger aspect ratios

The thin-strip tests on convergence, of course, tell us very little about the formulation for apertures of larger aspect ratios. The transverse component of current is quite small on the strip, and the transverse variation of the longitudinal component is not significant over the small electrical width of the strip.

Figure 3.6 provides some insight into the convergence of the poles for a range of aspect ratios for several zoning densities. The pole trajectory is for the second $++$ (w.r.t. J_x) in the "layer" nearest the imaginary axis. We note that $wL/c\pi = 3.0$ corresponds to a $1-1/2$ wavelength structure so that a density of five zones per $L/2$ pulses in the first quadrant is equivalent to 6.67 pulses per wavelength.

The convergence of pole locations for larger aspect ratios was tested by comparing those obtained with 4×4 zones in the first quadrant with those computed with 5×5 zones. The comparisons are shown as the solid and dashed lines, respectively, in the "loop" region. The aspect ratios are shown as decimal fractions. We observe excellent agreement in the two trajectories. The error at $w/L = 1.0$ is 1.16 percent of the magnitude of the poles.

In following a pole trajectory, it is desirable to use the same number of zones insofar as possible so that a smooth trajectory is determined. This is not always possible for smaller aspect ratios because of numerical instability problems inherent in over-dense zoning. The continuation of the 4×4 zone trajectory is shown down to $w/L = 0.3$ in Figure 3.6. For aspect ratios smaller than 0.3, numerical instability besets us and the trajectory cannot be determined. In practice, the numerical instability may be manifested in one of two forms: either

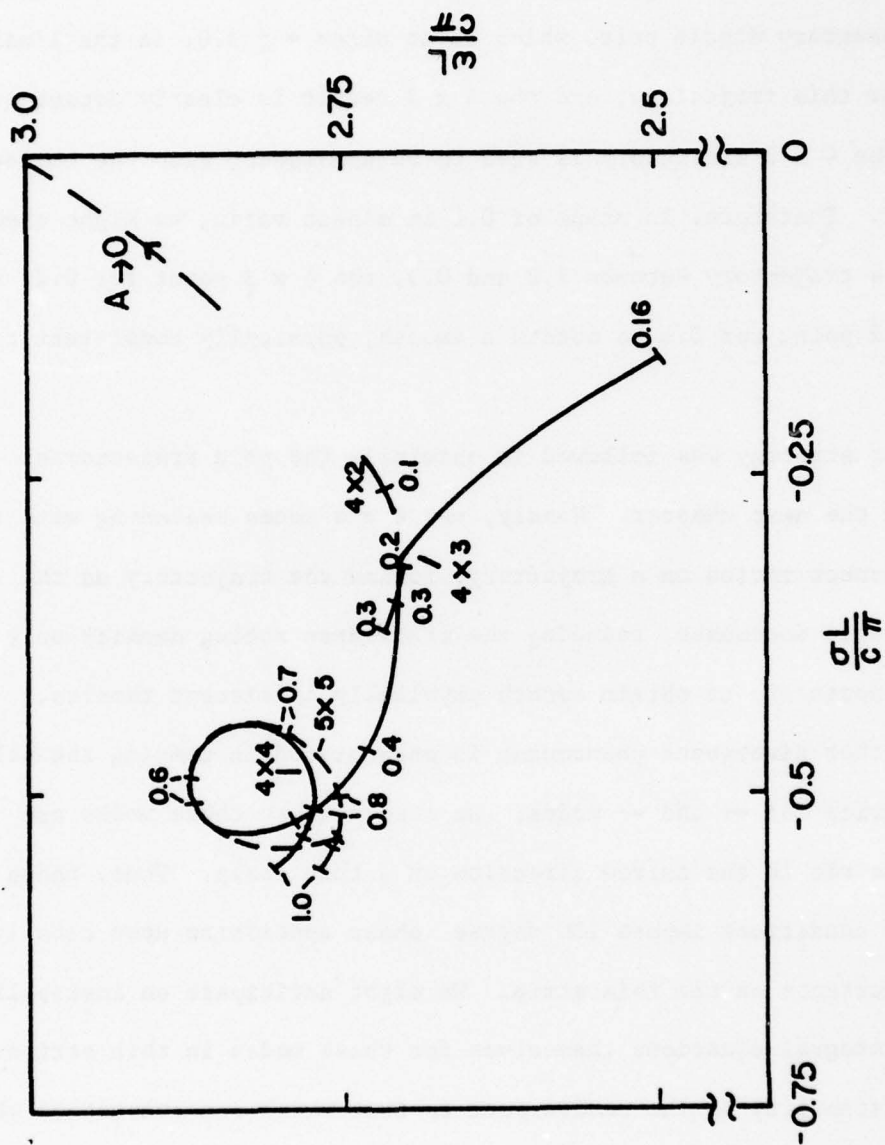


Figure 3.6. Convergence study plots of the second ++ mode poles.

a failure to converge in the pole search or an abrupt "tailing off" in a smooth trajectory. The former manifestation forced the termination of the 4 x 4 trajectory. The latter is evident in the 4 x 3 trajectory plotted. The filamentary dipole pole, which is at $sL/c\pi = j 3.0$, is the limiting point for this trajectory, and the 4 x 3 result is clearly departing from this. The 4 x 2 trajectory is seen to be consistent with the correct behavior. Therefore, in steps of 0.1 in aspect ratio, we might choose the 4 x 4 trajectory between 1.0 and 0.3, the 4 x 3 point for 0.2, and the 4 x 2 point for 0.1 to obtain a smooth, physically consistent trajectory.

This strategy was followed in obtaining the pole trajectories given in the next chapter. Namely, use 4 x 4 zones beginning with the larger aspect ratios on a trajectory; follow the trajectory as the aspect ratio decreases, reducing the transverse zoning density only as much as necessary to obtain smooth physically consistent results.

Another divergence phenomenon is encountered in tracing the pole trajectories for \rightarrow and \leftarrow modes. We observe that these modes are antisymmetric in the narrow direction on a thin strip. Thus, these symmetry conditions impose 180 degree phase opposition upon closely spaced currents on the thin strip. We might anticipate an instability in the integral equations themselves for these modes in thin strips. (This instability is the counterpart to that which one encounters when solving two parallel linear antennas which are closely spaced.)

Instability does appear in these solutions. Its manifestation is that for thin strips with the longitudinal component of current

antisymmetric in the transverse direction the pole search converges, but the point to which the algorithm converges is weakly dependent (within a few percent) on its starting point. In addition, the pole values obtained depend strongly on the number of zones used. This zone dependence is evident in Figure 3.7. The result is that none of the \rightarrow or \leftarrow trajectories are determinable by the present means for aspect ratios of below 0.2 or 0.3. The dominant current component is antisymmetric in the narrow direction, however. This results in weak coupling of these modes for smaller aspect ratios so that they are generally negligible.

3.5 Pole Location Strategies

The basic pole location method used in this work was the Muller iteration to find zeros of the determinant of the moment matrix as a function of the complex frequency s as was mentioned in Section 3.4. It appears to be a common trait to numerical SEM formulations that except for the poles near the imaginary axis in the complex plane, the contours of the determinant indicate the presence of the zero determinant in a highly local fashion. The paragraphs below describe the methods used in locating the poles in an exhaustive fashion without undue difficulty with the local character of the poles.

Baum [14] has proposed using the argument number of the determinant of the moment matrix as an indicator of the presence of a zero of the determinant within a prescribed region of the complex plane. The method exploits the analyticity of the determinant as a function of s . It follows that the number of zeros of the determinant $D(s)$ within a region in the s -plane bounded by a closed contour C is given by

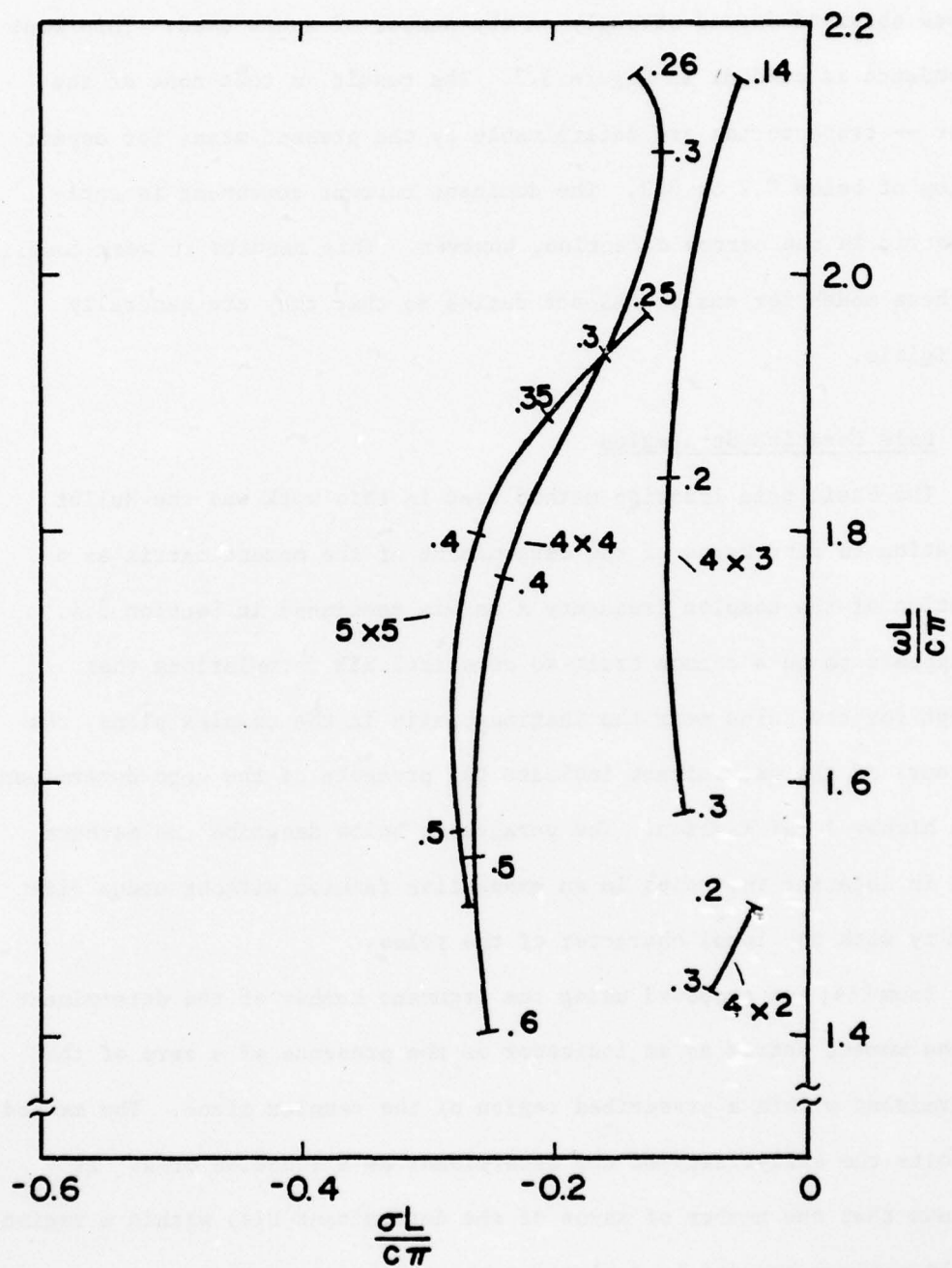


Figure 3.7. Trajectories of the first -- mode pole for various zonings and thinner aspect ratios.

$$N_C = \frac{1}{2\pi} V_C\{D(s)\} = \frac{1}{2\pi} (\arg[D(s)]|_C) ,$$

where V_C denotes the "variation of the argument" of $D(s)$ around the contour C . (See, for example, [3].) This approach was used conveniently and successfully in the present work to localize a pole to a small region before using the iterative method to locate it specifically.

Figure 3.8 illustrates the method used. The region of interest in the complex plane was subdivided into moderately sized quadrants. The argument number was evaluated around each quadrant from twenty-one values of $D(s)$ along each side of the quadrant. The contributions to N_C from each leg of each quadrant were evaluated separately so that only alternate quadrants needed to be computed. The results of the procedure for the $++$ modes are shown in Figure 3.8 for aspect ratios of 1.0 and 0.5. The pole trajectories eventually determined are included for reference purposes. It is seen that the method correctly localizes all of the poles and provides confidence that the search is exhaustive. Each quadrant was subsequently quadrasected. By evaluating the argument number on the four sides of two of the four subquadrants, the pole is still better isolated. The Muller iteration was then begun at the center of the subquadrant to which the pole was isolated and in every case converged from that point.

Once the two points on a trajectory corresponding to 0.5 and 1.0 aspect ratios were located, the trajectory was followed by changing the aspect ratio slightly and by using the pole location for the original aspect ratio as a starting point. This method of incrementing w/L fails in some cases when the pole location moves rapidly with respect to w/L . The following projection scheme proved useful in these cases.

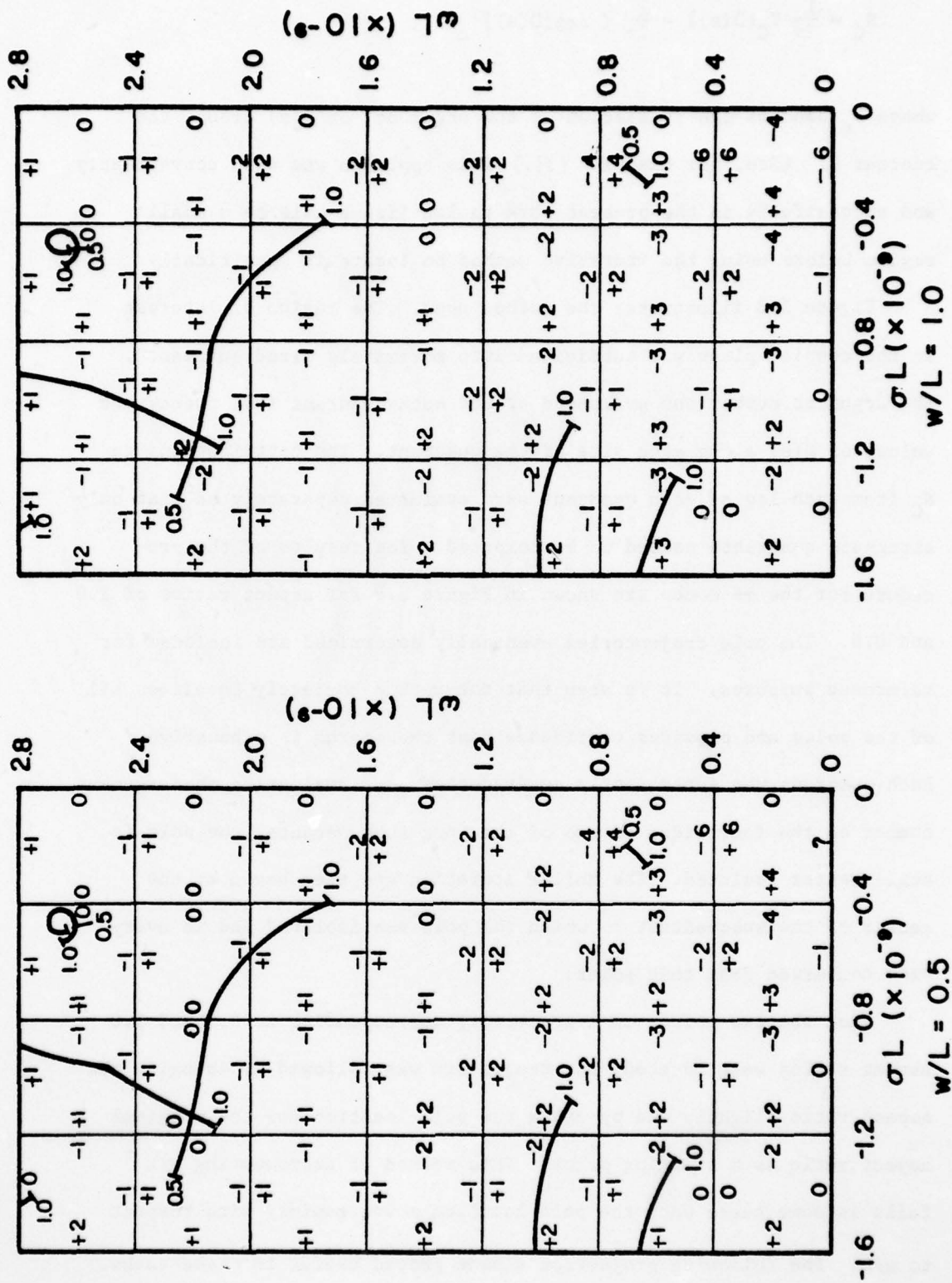


Figure 3.8. The scheme of separating the complex plane into quadrants to apply the argument number method in locating pole trajectories for the $++$ modes.

We observe from Figure 3.2 that for $w/L = 1$ a ninety-degree spatial rotation of the $++$ mode results in the $--$ mode configuration in the original coordinate system. Similarly, the $+-$ mode rotates into itself, and the $-+$ mode does, as well. This means that a $++$ distribution for $w/L = 2.0$ is identical to a $--$ distribution with $w/L = 0.5$. Similarly, the pole for each case will be identical when normalized to the long dimension.

Figure 3.9 shows the $++$ pole trajectory continued on past $w/L = 1.0$ to $w/L = 8.0$. Note that the scales for the plot are normalized to L . To renormalize, for example, the $w/L = 2.0$ $++$ pole to w , we need to multiply the pole value $sL/c\pi$ by w/L . Because of the rotation property, the renormalized $w/L = 2.0$ $++$ pole is identical with the $--$ $w/L = 0.5$ pole. This relationship is denoted graphically in Figure 3.9 by the line segment passing through the $w/L = 2.0$ point on the $++$ trajectory and striking the $w/L = 0.5$ point on the $--$ trajectory. The length of the segment OB on this line is twice OA . Three other specimen radii indicate this relationship at other points.

It is observed that the $--$ curve is rapidly varying with respect to aspect ratio. We can follow it with ease, however, by computing the $++$ curve on past $w/L = 1.0$ in the incremental fashion discussed above and projecting it outward to form the $--$ trajectory. This procedure was employed to advantage in obtaining the results presented in the next chapter, both by projecting $++$ onto $--$ trajectories and by projecting $+-$ or $-+$ trajectories onto themselves. A posteriori tests of the projection corroborated that the correct pole had been projected.

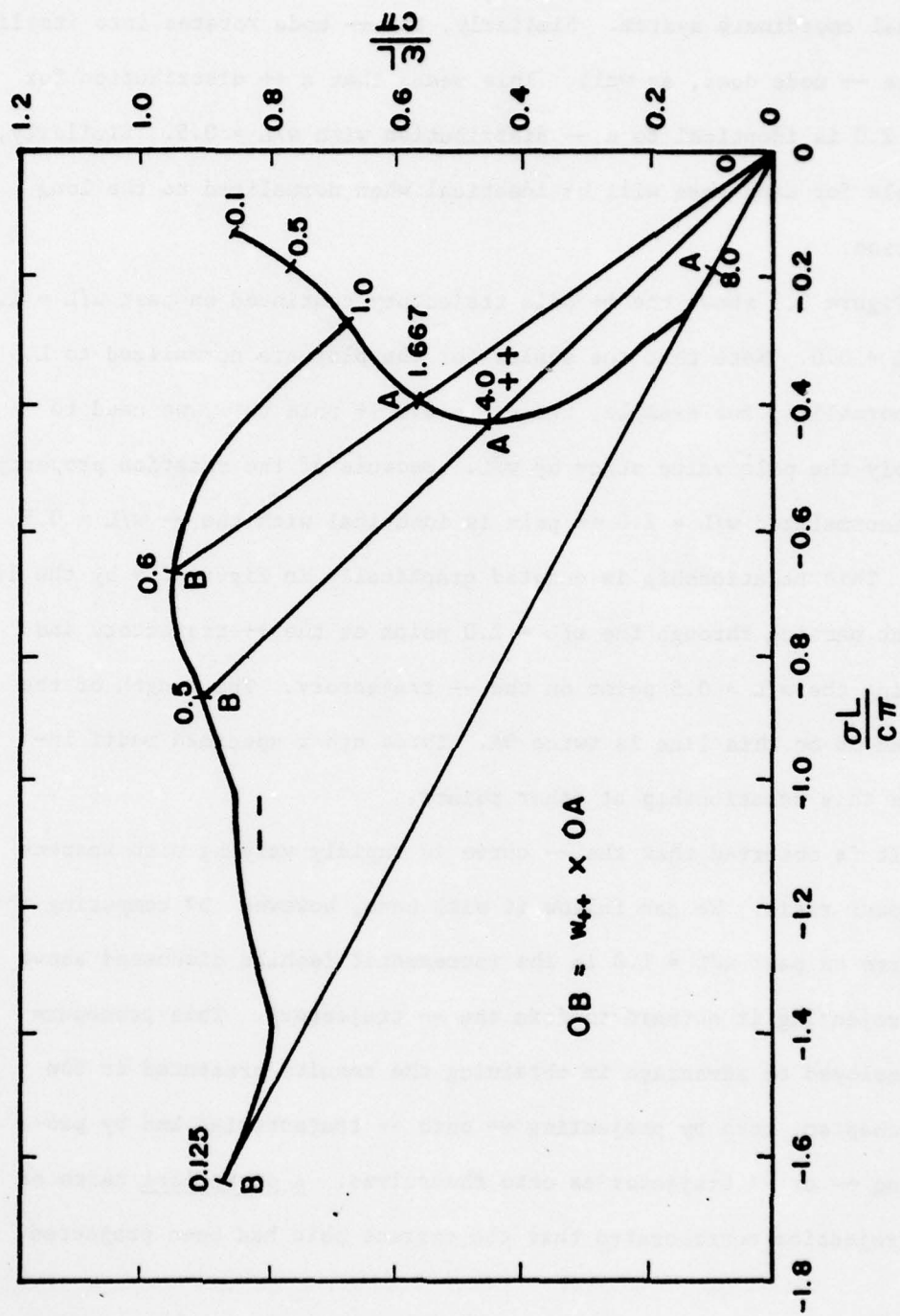


Figure 3.9. Projection of the oversquare ++ trajectory onto the undersquare -- trajectory.

4. SEM CHARACTERIZATION FOR THE RECTANGULAR PLATE

4.1 Introduction

This chapter provides the pole and natural mode data for the dominant terms in the SEM characterization of the rectangular plate. By duality, the representation applied to the rectangular aperture as well. The data span the three dominant resonances for the structure - that is, a range of frequencies extending, nominally, to where the greater dimension of the rectangle is one-and-one-half wavelengths. The aspect ratio parameter w/L is varied between 0.1 and 1.0. Rahmat-Samii and Mittra have observed in previously reported work [15] that for frequencies corresponding to roughly one wavelength and beyond, the aperture becomes quite broadband so that transient waves with higher frequency spectral content are passed essentially unmodified. This observation is supported by the present data which show poles in proximity to one another appearing at higher frequencies.

Representative natural modes for selected poles are presented herein. Exhaustive graphical presentation of the corresponding natural modes here is prohibitively cumbersome both because of their number (approaching two hundred) and because of the futility of trying to represent complex vector functions of two variables. More nearly complete data are available in a digital computer data base format, however [3]. The data base storage of SEM data for complex structures, such as the aperture, is more in accord with ultimate user needs, because a computer is almost certainly required in any useful expansion of the data.

The coupling vectors and normalization constants are a part of the data base but are not reported here. The qualitative aspects of coupling are discernible from the natural mode data.

Section 4.2 deals with the pole locations for the structure and discusses the resonance behavior of the plate or aperture for the four modal symmetries. Section 4.2 presents some of the associated natural modes which have been selected to be representative of the mode structure in general.

4.2 Pole Trajectories of the Plate/Aperture as a Function of Aspect Ratio

The locations of poles for the rectangular structure are given in Figure 4.1 for a region of the third quadrant of the complex plane nearest the origin. The third quadrant data suffice because all poles have negative real parts and are arranged with conjugate symmetry in the complex plane. The poles are normalized with respect to $L/c\pi$ where L is the greater dimension of the rectangle. The small numbers adjacent to trajectories indicate the aspect ratio w/L for the tick mark beside which the number stands. Ticks are spaced at aspect ratio intervals of 0.1. Dashed lines indicate the trends of trajectories which are not completely determined. Poles that are left undetermined on a known trajectory either are judged negligible in contribution compared with poles close to the axis or in the case of $+$ and $-$ modes are undeterminable by the present method for the reasons outlined in Section 3.4.2. We reiterate that in the latter case the coupling coefficients will be small so that we may neglect these poles.

In the following paragraphs, we consider the physical significance of the pole behavior as shown in Figure 4.1. We discuss the $++$ and $+-$ modes as a group and then treat the $-+$ and $--$ modes. The former group possesses the common property of being symmetric about the x-axis, i.e., in the transverse direction. The latter group is antisymmetric

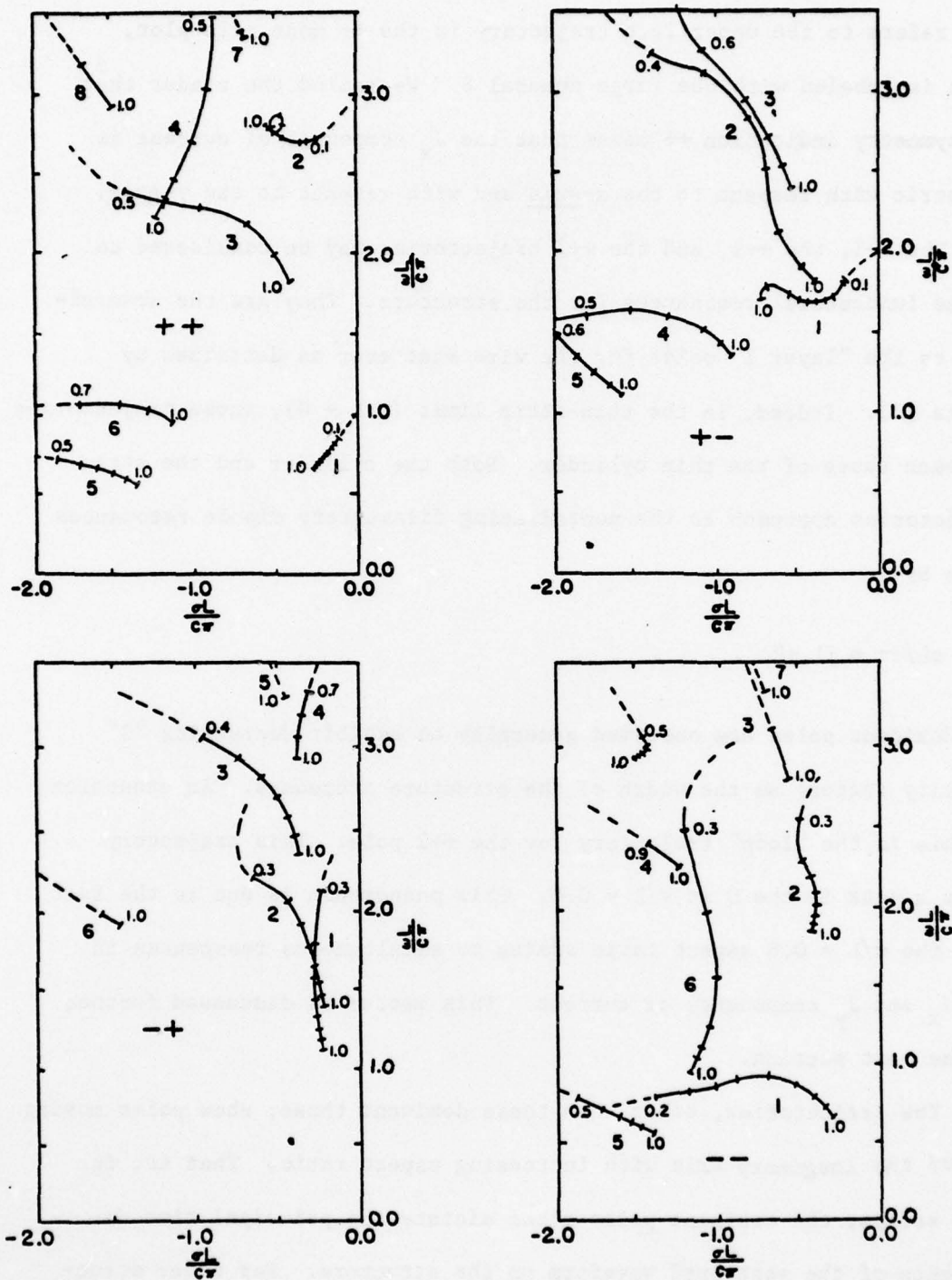


Figure 4.1. Pole trajectories for the four modal symmetries. Tick marks are spaced at increments of 0.1 in w/L . Decimal fractions indicate specific w/L ratio at selected ticks.

in the transverse direction. Terminology of the form ++8 is used: this refers to the upper-left trajectory in the ++ mode pole plot, which is labeled with the large numeral 8. We remind the reader that the symmetry indication ++ means that the J_x component of current is symmetric with respect to the x-axis and with respect to the y-axis.

The ++1, the +-1, and the ++2 trajectories may be considered to be the fundamental resonances for the structure. They are the counterpart to the "layer 1" poles for the wire scatterer as described by Tesche [3]. Indeed, in the thin-strip limit ($w/L \rightarrow 0$), these trajectories approach those of the thin cylinder. Both the cylinder and the strip trajectories approach to the nonradiating filamentary dipole resonances given by

$$sL/c\pi = j1, j2, \dots$$

The dominant poles are observed generally to exhibit decreasing "Q" (quality factor) as the width of the structure increases. An exception to this is the "loop" trajectory for the ++2 pole. This trajectory shows a peak in the Q at $w/L = 0.6$. This phenomenon is due to the fact that the $w/L = 0.6$ aspect ratio admits to simultaneous resonances in the J_x and J_y components of current. This matter is discussed further in the next section.

The trajectories, other than these dominant three, show poles moving toward the imaginary axis with increasing aspect ratio. That is, for thin strips, the dominant poles alone dictate the principal time dependence of the scattered waveform on the structure. For wider structures, the "layer 2" poles move toward the imaginary axis and influence the scattered fields as well. For example, for the square structure

with $w/L = 1.0$, we observe roughly equal order real parts for six modes. These complex frequency data corroborate real frequency broadbanding for $\omega L/c\pi \geq 1$ which Rahmat-Samii and Mittra observed in [3].

The region of the complex plane shown in Figure 4.1 is not large enough to allow comparison with the second layer poles for the cylinder from [3]. We note, in passing, that in the few observations made, there is not an agreement between the $w/L \rightarrow 0.1$ limits of the nondominant trajectories in Figure 4.1 and the layer 2 poles of the cylinder. It is not at all clear whether such an agreement should exist. If it should, either the failure to go to the filamentary limit or simply numerical errors inherent in the deep-plane results preclude observation of it.

The \rightarrow and $--$ modes cannot be directly related to cylinder modes. This is due to the nonphysical nature of antisymmetry of the longitudinal current in the transverse direction in the thin strip limit of these modes. It is difficult to separate out a dominant set of poles from Figure 4.1 for these symmetries. We do observe the grouping of many poles in the square-structure limit very much in the manner of the $++$ and $+-$ modes. However, several trajectories move on a path roughly parallel to the imaginary axis. This increase in Q with the narrowing of the structure is thus an increase in oscillation frequency of these modes at an approximately constant damping rate.

We make one other final observation about the poles. It is observed in Section 3.5 that on a square structure the $++$ and $--$ modes are identical with a 90 degree rotation of coordinates. A consequence of this property is that there is a $++$ $w/L = 1.0$ pole identical with

each -- $w/L = 1.0$ pole. This is evident in Figure 4.1. For example, the --1 and ++1 poles are identical for $w/L = 1.0$. The numbering scheme for the trajectories is, in fact, chosen so that the ++n and --n trajectories coalesce at $w/L = 1.0$ for each trajectory.

4.3 Natural Modes for the Rectangular Structure

4.3.1 Graphical representation of the modes

In the four subsections which follow, we present graphical data intended to characterize the natural modes associated with the poles shown in Figure 4.1. Complete mode data, i.e., data for each pole increment, are precluded by the sheer volume of information involved. As a result, representative mode data selected from the complete data base are given in the figures which follow.

Each natural mode is a two-component complex-valued vector function of two variables. The form of the displays is evident in Figure 4.2. Each mode is plotted as a current distribution on a thin-plate scatterer and separate plots for the x and y current components are given. The curves are magnitude/phase representations of the complex quantities. The rectangular shape of the plate is shown in proper proportion for each of the current components. The graph below the rectangle gives the appropriate current component along a cut in the transverse coordinate y. The graph to the right gives the same current component along a cut in x. (Note that x increases from right to left looking from below the x-axis.) The cuts along which the graph is taken are shown on the rectangle. In the case of multiple cuts in the same direction, a cut and the graph along the cut are coordinated by the same line type, i.e., solid, dashed, etc.

4.3.2 The ++ modes

Figures 4.2 through 4.6 are plots of selected ++ symmetry natural modes. Some of the features of the currents in Figure 4.2 are common to currents of all symmetries. The mode represented, the ++1 $w/L = 1.0$ mode, is a first resonance as manifested by the single "half-cycle" behavior in the x-coordinate cut of the J_x component of current. The transverse cut - that in the y-coordinate - indicates a steeply peaked behavior of the current near the edge. This is the representation obtained by the graphical interpolation through the subsectionally constant method of moments current solution. It is an approximate numerical representation of the correct singular current behavior as given by (3.3). The method of moments solution also manifests an "undershoot" in the first current zone inward from the edge zone as indicated near $y/L = \pm 0.3$ in the figure. Because of the rapid variation of this hump with respect to wavelength, we hold it suspect. A likely cause for such anomalous behavior is the approximation of a singular function by a constant zone for the current at the edge. In spite of these two anomalies, we expect the subsectionally zoned current to provide good approximate scattered field information at distances from the plate on the order of nominally one-half wavelength and greater.

Figures 4.3 through 4.5 give the modes for three different aspect ratios on the ++2 pole trajectory. A comparison of Figure 4.4 with 4.3 and 4.5 indicates that the transverse - J_y - current is much larger in magnitude for $w/L = 0.6$ than for 1.0 or 0.2. Indeed, it is the largest transverse component along the ++2 trajectory. This observation along with the observed loop in the ++2 trajectory is interpreted to be

AD-A036 999

ILLINOIS UNIV AT URBANA-CHAMPAIGN

F/G 20/14

THE SINGULARITY EXPANSION REPRESENTATION OF THE TRANSIENT ELECT--ETC(U)

FEB 77 L W PEARSON, R MITTRA

AF-AFOSR-2861-75

UNCLASSIFIED

AFWL -TR-76-249

NL

2 OF 2

AD
A036 999

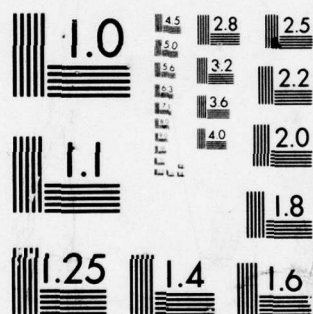


END

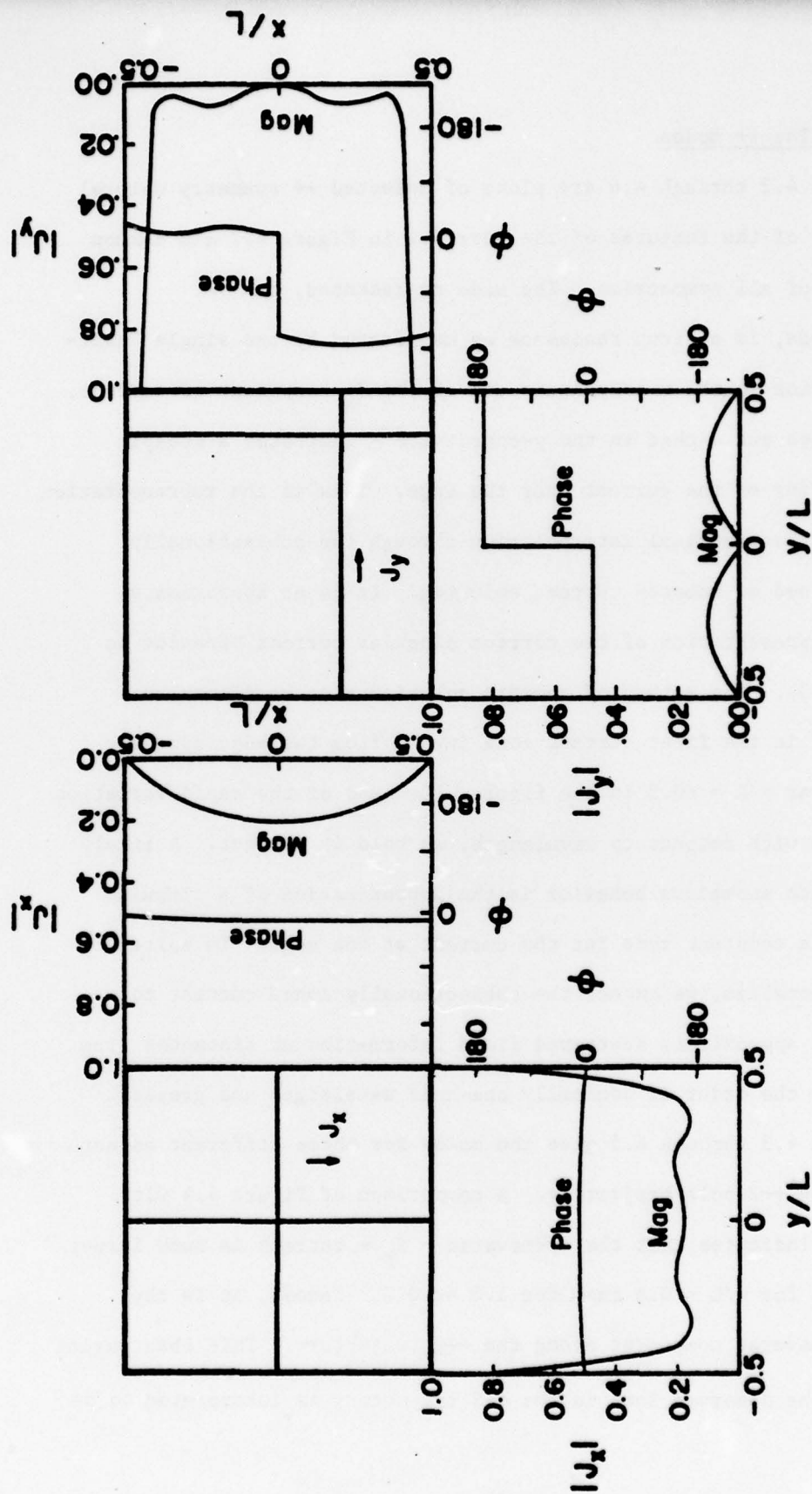
DATE

FILMED

4-77



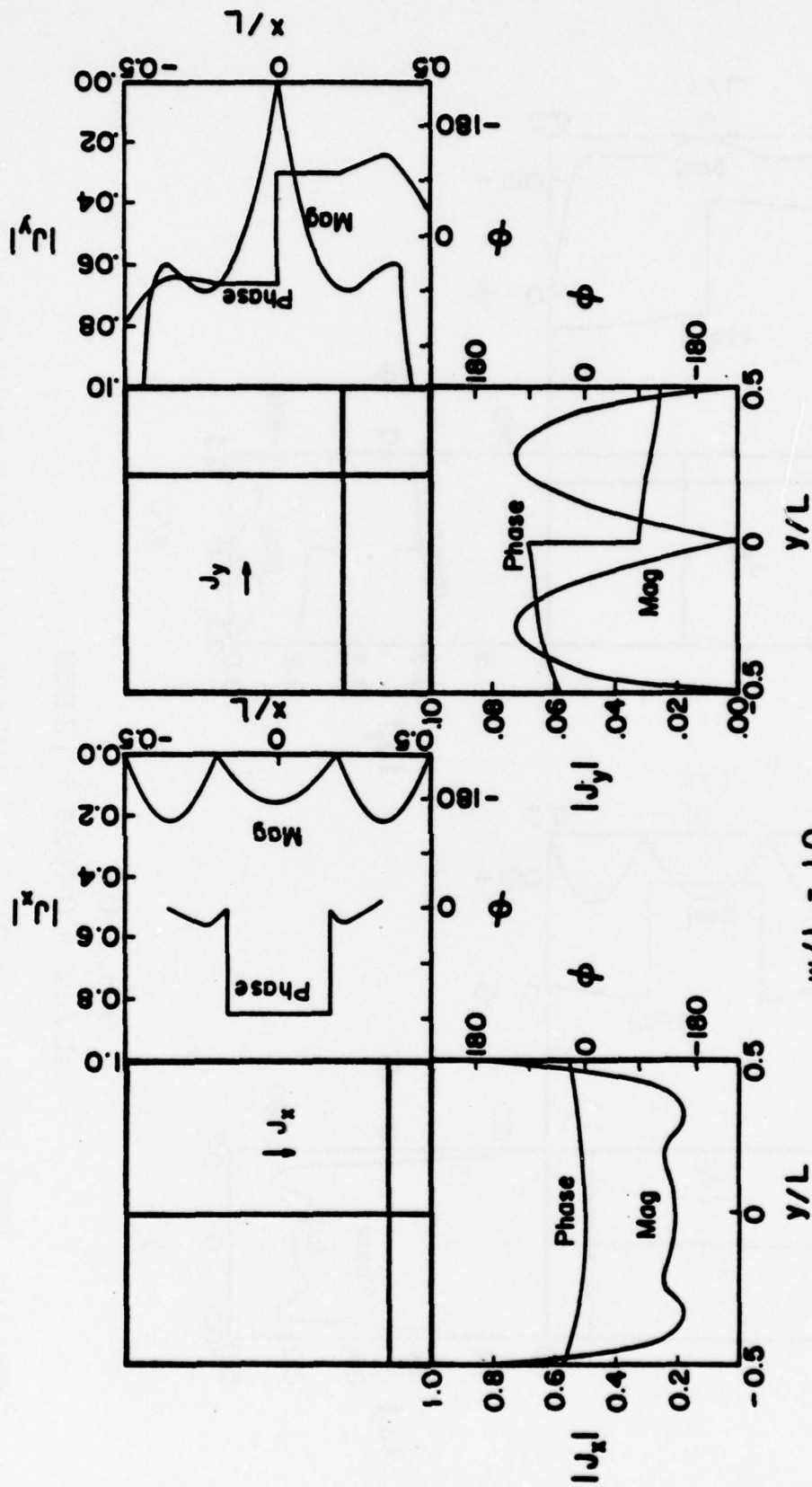
MICROCOPY RESOLUTION TEST CHART
NATIONAL BUREAU OF STANDARDS-1963-A



$$w/L = 1.0$$

$$sL/c\pi = -0.2724 + j.6754$$

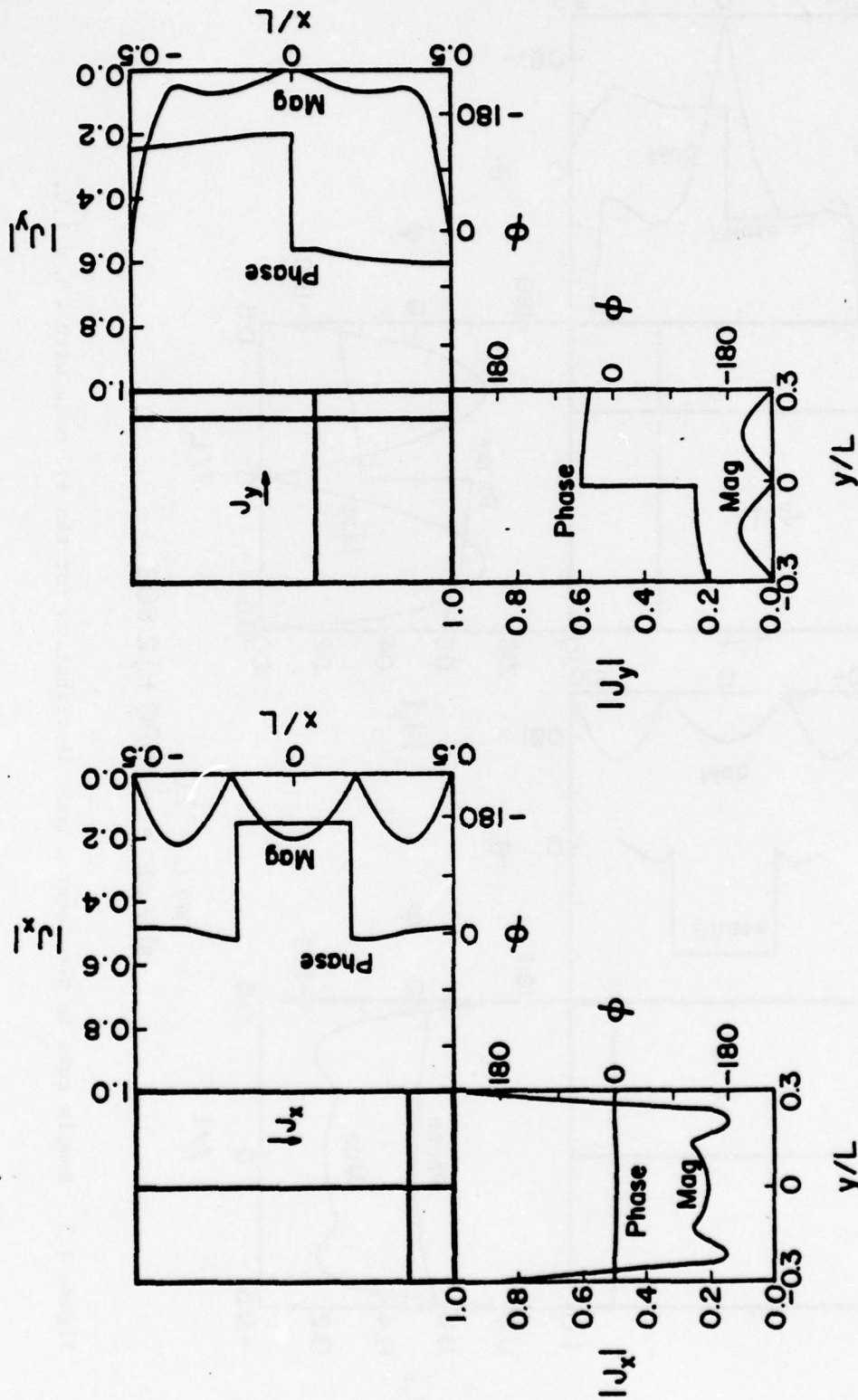
Figure 4.2. Sample cuts in the natural mode distribution for the ++1 mode with $w/L = 1.0$.



$$w/L = 1.0$$

$$sL/c\pi = -0.5590 + j2.802$$

Figure 4.3. Sample cuts in the natural mode distribution for the ++2 mode with $w/L = 1.0$.



$$w/L = 0.6$$

$$sL/c\pi = 0.4834 + j2.866$$

Figure 4.4. Sample cuts in the natural mode distribution for the ++2 mode with $w/L = 0.6$.

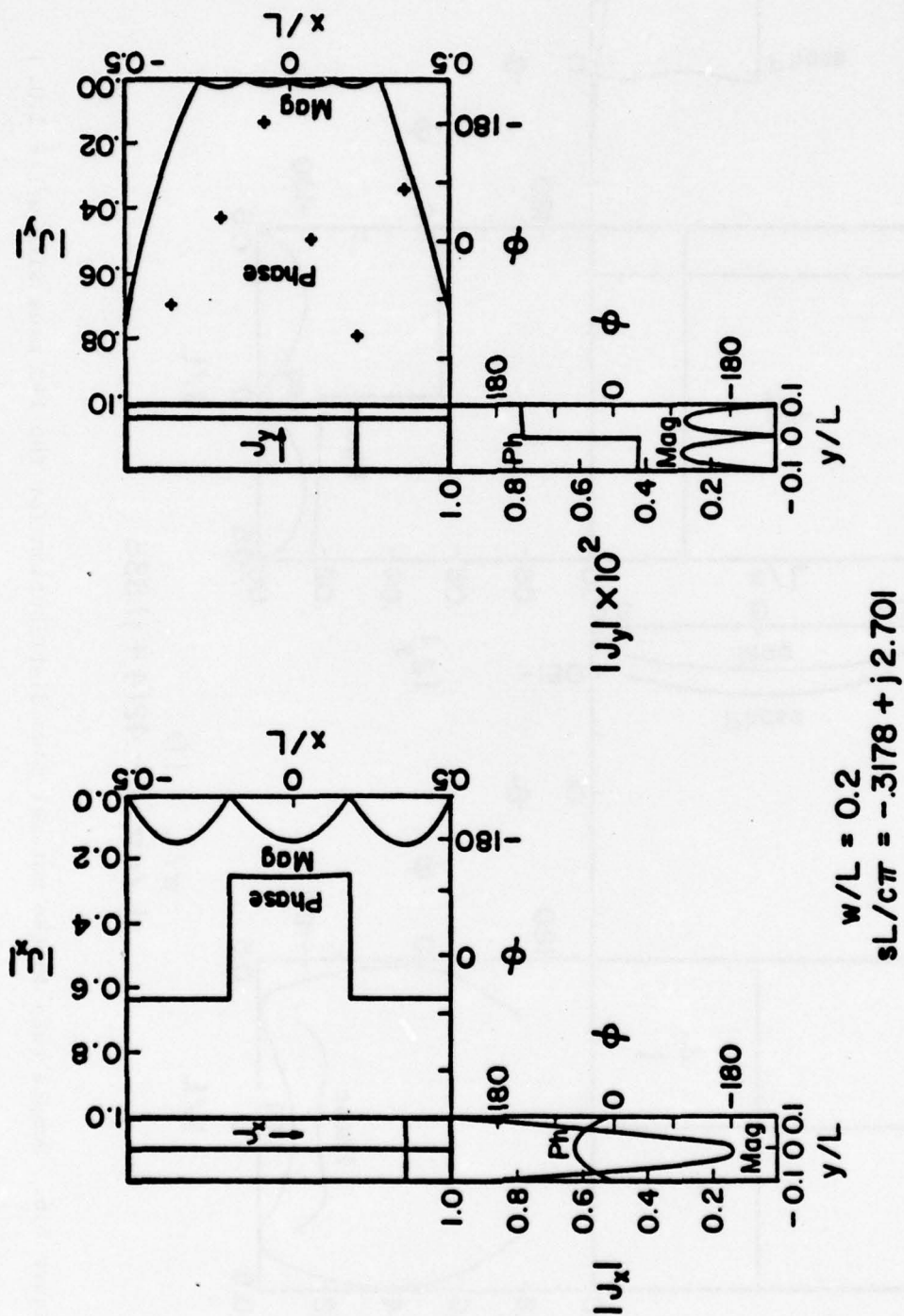


Figure 4.5. Sample cuts in the natural mode distribution for the ++2 mode with $w/L = 0.2$.

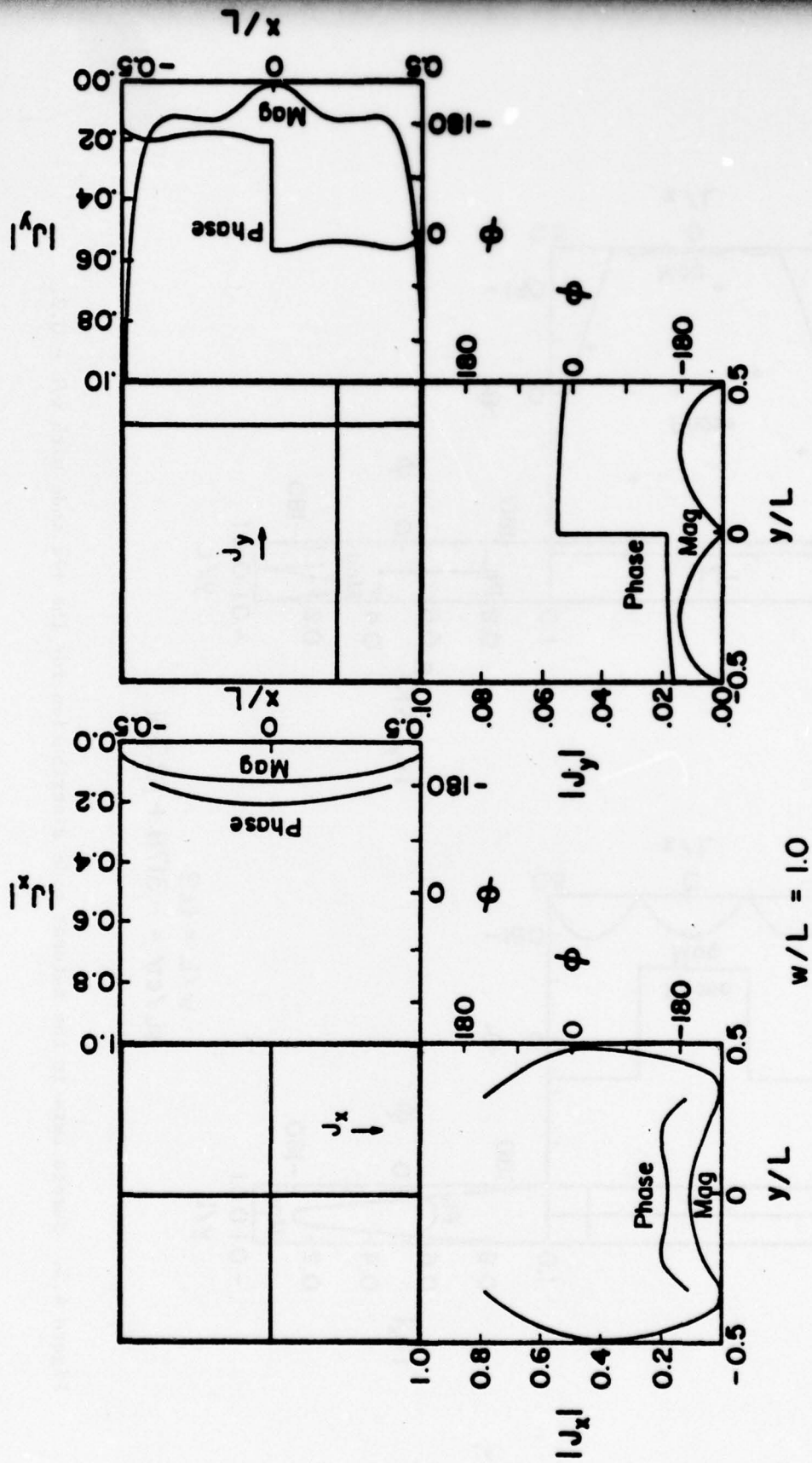


Figure 4.6. Sample cuts in the natural mode distribution for the ++3 mode with $w/L = 1.0$.

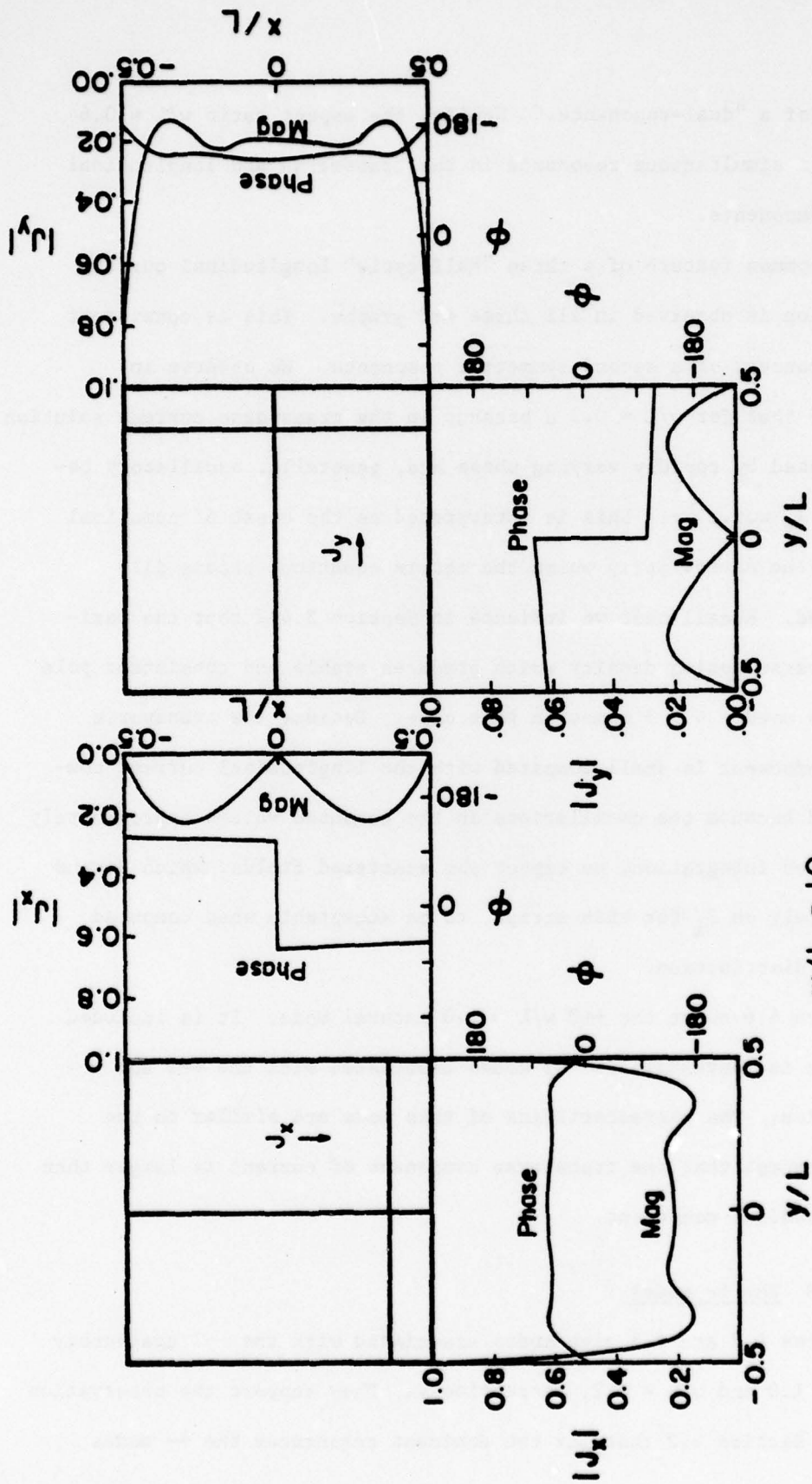
something of a "dual-resonance." Namely, the aspect ratio $w/L = 0.6$ admits to a simultaneous resonance in the transverse and longitudinal current components.

The common feature of a three "half-cycle" longitudinal current distribution is observed in all three $++2$ graphs. This is consistent with the concept of a second symmetric resonance. We observe in Figure 4.5 that for $w/L = 0.2$ a breakup in the transverse current solution is manifested by rapidly varying phase and, generally, oscillatory behavior of J_y w.r.t. x . This is interpreted as the onset of numerical noise for the narrow strip where the matrix equations become ill-conditioned. Recall that we indicate in Section 3.4.2 that the maximum transverse zoning density which produces stable and consistent pole results is used - 4×3 zones in this case. Because the transverse current component is small compared with the longitudinal current component and because the oscillations in the computed values approximately cancel under integration, we expect the scattered fields, which depend almost solely on J_x for thin strips, to be acceptable when computed from this distribution.

Figure 4.6 shows the $++3$ $w/L = 1.0$ natural mode. It is included because it is representative of modes associated with the $++3$ and $++4$ trajectories. The characteristics of this mode are similar to the $++1$ mode except that the transverse component of current is larger than the longitudinal component.

4.3.3 The $+-$ modes

Figures 4.7 and 4.8 give modes associated with the $+-1$ trajectory for $w/L = 1.0$ and $w/L = 0.2$, respectively. They support the observation stated in Section 4.2 that for the dominant resonances the $+-$ modes



$$w/L = 1.0$$

$$sL/c\pi = -0.7170 + j1.714$$

Figure 4.7. Sample cuts in the natural mode distribution for the +1 mode with $w/L = 1.0$.

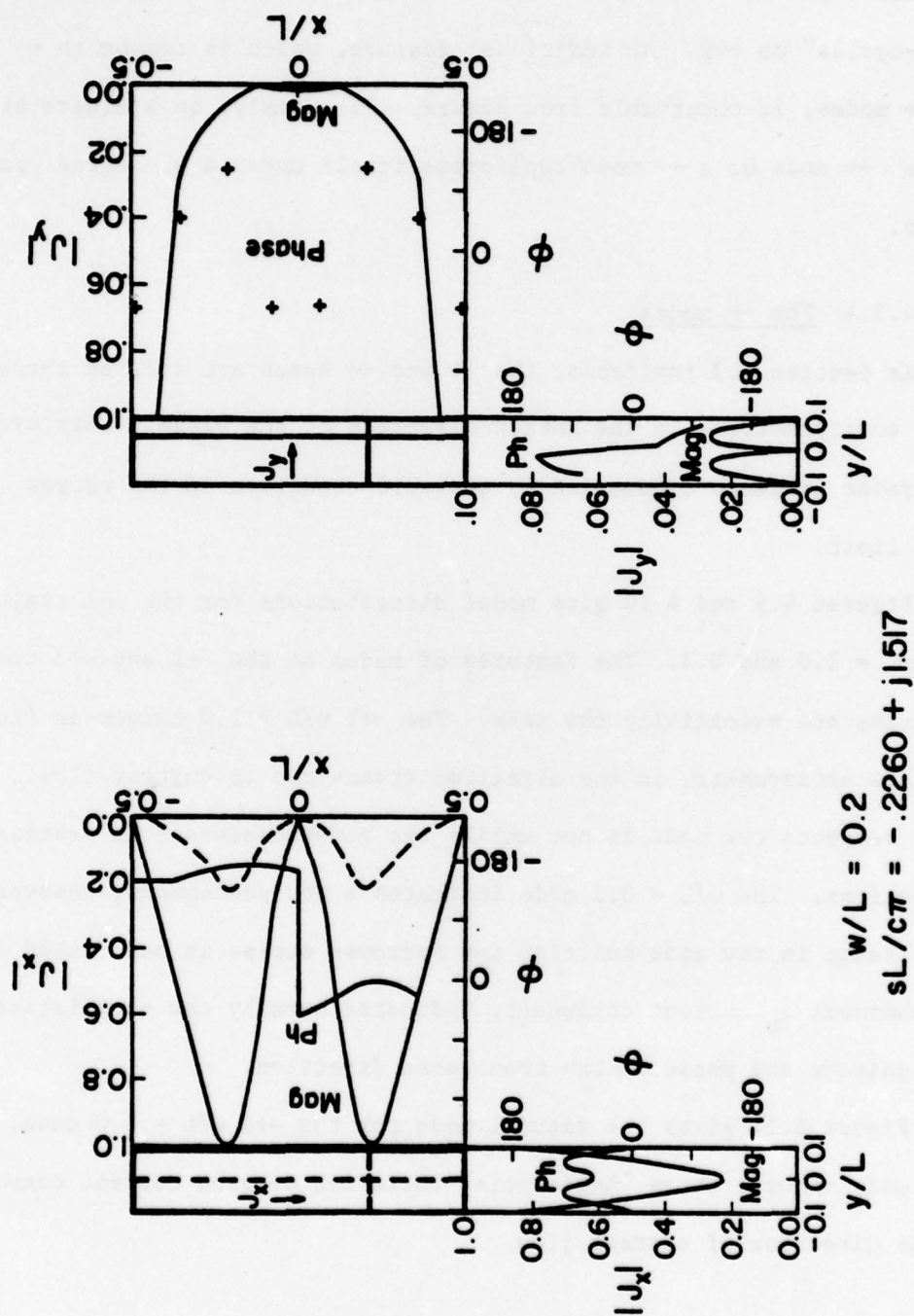


Figure 4.8. Sample cuts in the natural mode distribution for the +1 mode with $w/L = 0.2$.

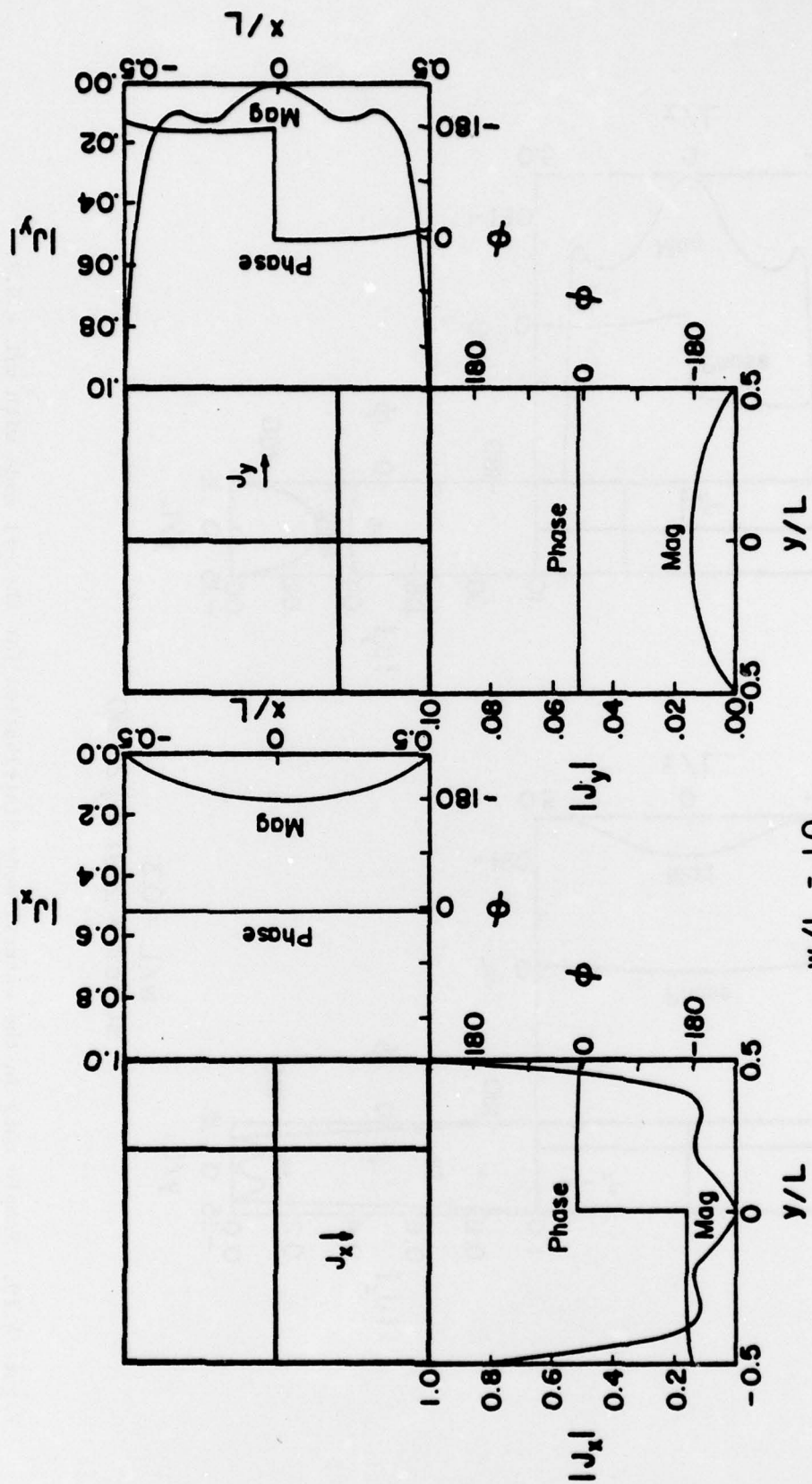
constitute the intermediate resonances between the $++$ modes. Comparisons of Figure 4.7 with 4.2 and 4.3 and of Figure 4.8 with 4.5 show a progression from one "half-cycle" on $++1$ to two on $+-1$ and then three "half-cycles" on $++2$. An additional feature, which is common to $+-$ and $-+$ modes, is observable from Figure 4.7. Namely, on a square structure a $+-$ mode or a $-+$ mode replicates itself under a 90 degree rotation.

4.3.4 The $-+$ modes

As Section 4.2 indicates, the $-+$ and $--$ modes are related through their antisymmetries in the narrow direction of the plate. This symmetry constraint produces a numerically unstable condition in the narrow strip limit.

Figures 4.9 and 4.10 give modal distributions for the $-+1$ trajectory and $w/L = 1.0$ and 0.3 . The features of modes on the $-+2$ and $-+3$ trajectories are essentially the same. The $-+1$ $w/L = 1.0$ curves in Figure 4.9 indicate antisymmetry in the direction transverse to current flow. In other respects the mode is not unlike the modes discussed in previous subsections. The $w/L = 0.3$ mode indicates a new phenomenon, however. The breakup in the mode solution for narrower strips is manifested in the dominant J_x current component, indicated here by the oscillations in magnitude and phase in the transverse direction.

Figure 4.11 gives the natural mode for the $-+4$ $w/L = 1.0$ case. This mode shows a three "half-cycle" variation of each current component in the direction of current flow.



$$w/L = 1.0$$

$$sL/c\pi = -2.153 + j1.085$$

Figure 4.9. Sample cuts in the natural mode distribution for the -1 mode with $w/L = 1.0$.

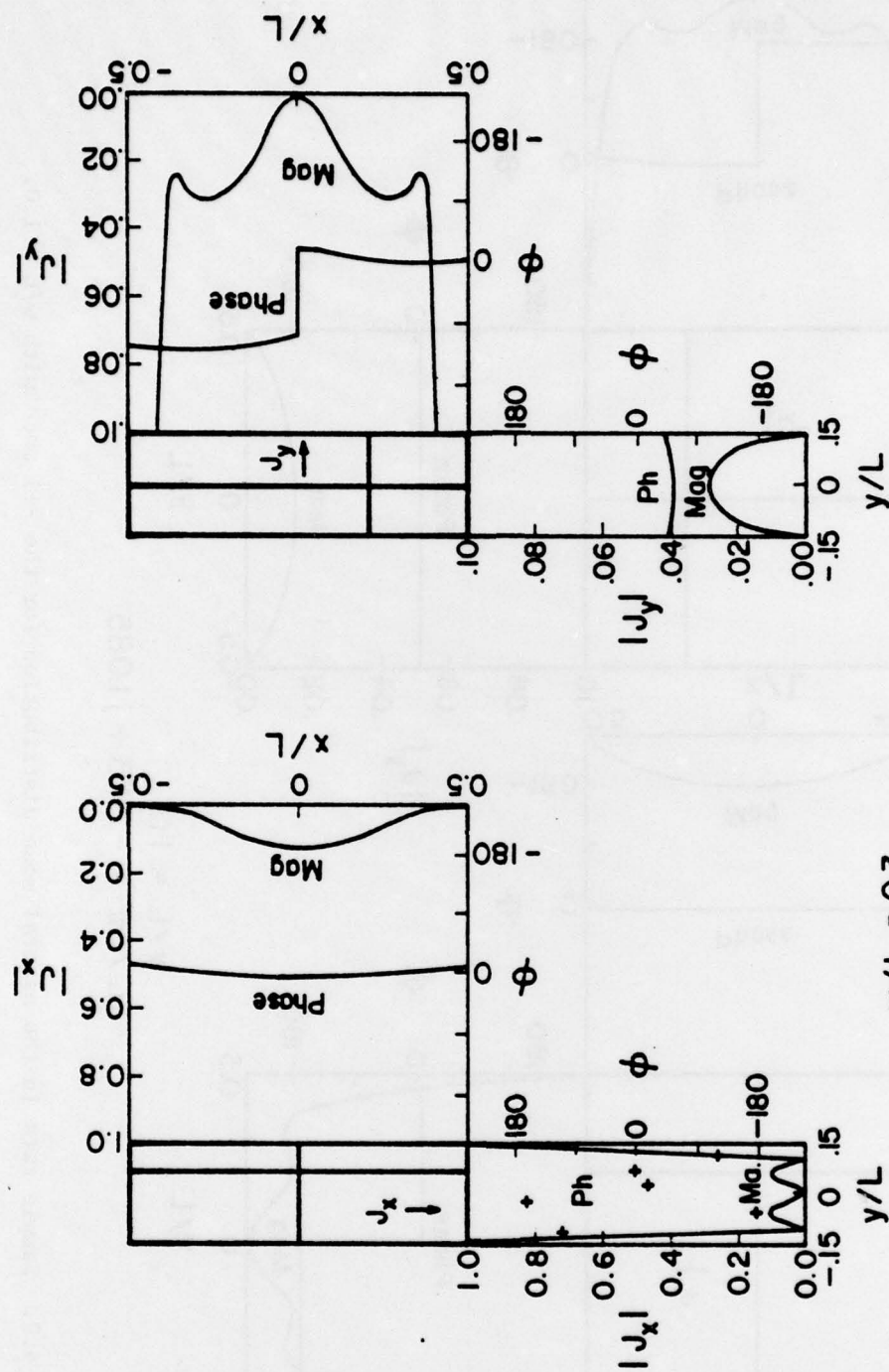


Figure 4.10. Sample cuts in the natural mode distribution for the -1 mode with $w/L = 0.3$.

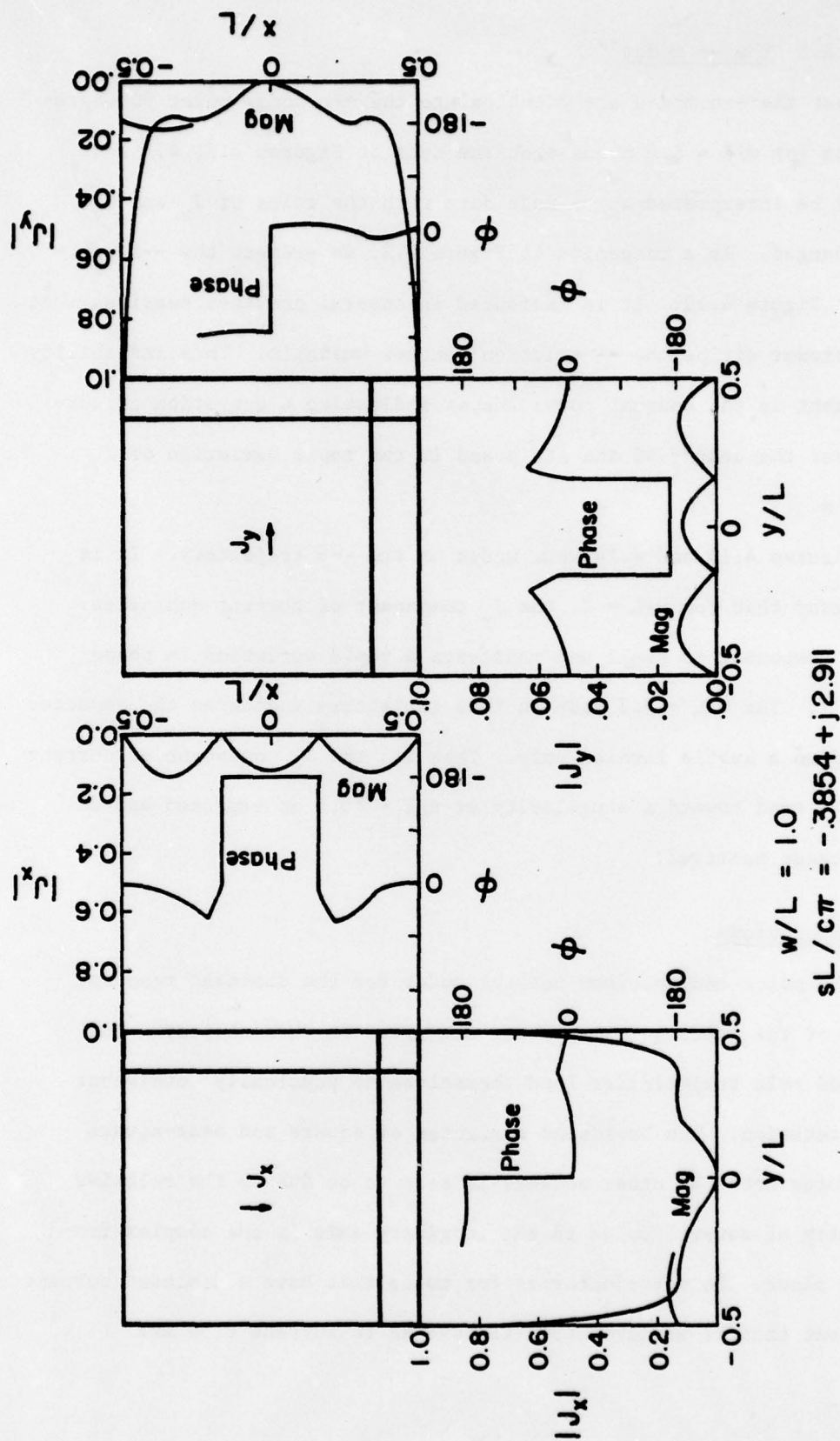


Figure 4.11. Sample cuts in the natural mode distribution for the $-+4$ mode with $w/L = 1.0$.

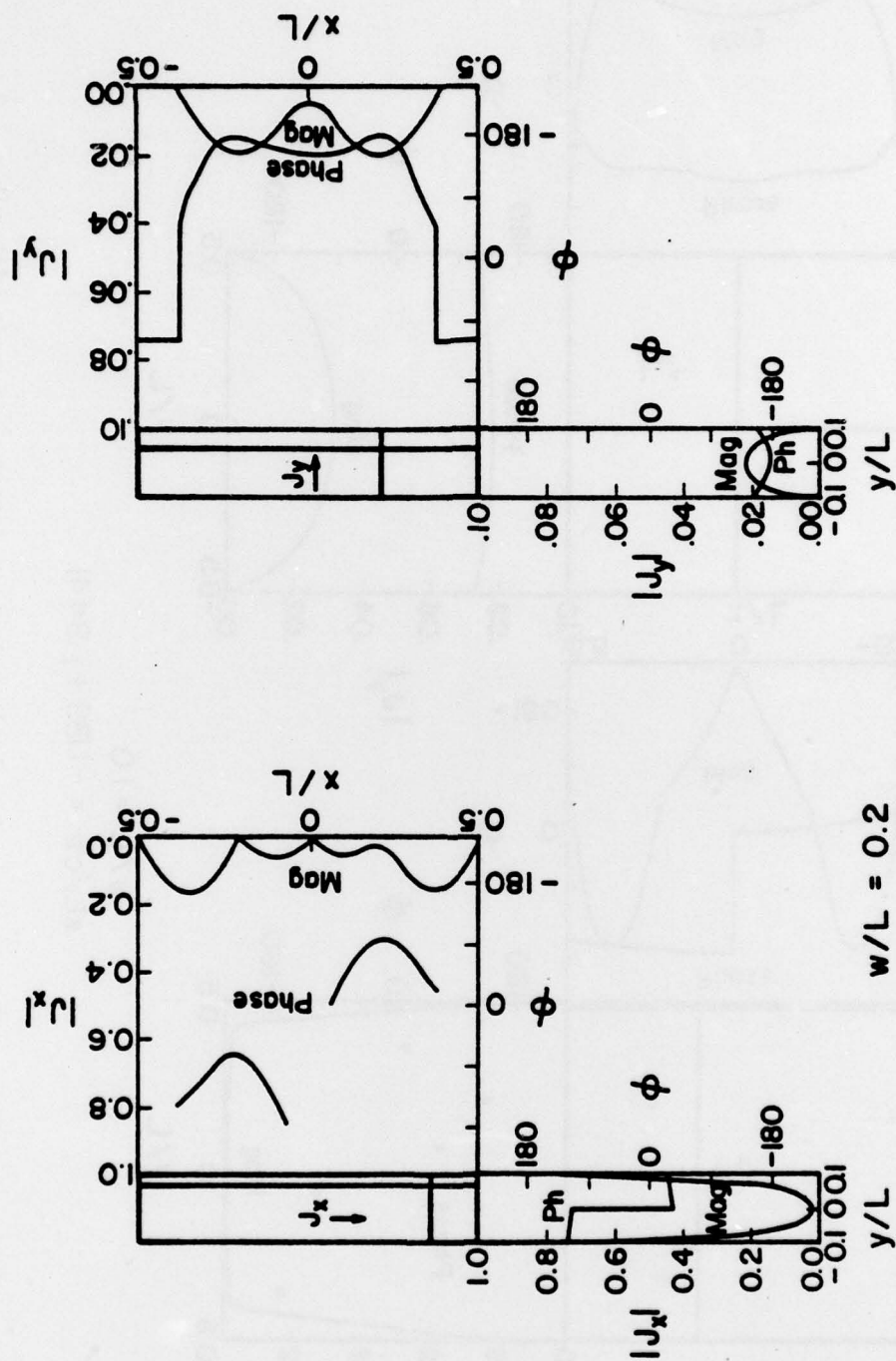
4.3.5 The -- modes

That the --n modes are identical to the ++n modes under 90 degree rotation for $w/L = 1.0$ means that the data in Figures 4.2, 4.3 and 4.6 may be interpreted as -- mode data with the roles of J_x and J_y interchanged. As a companion to Figure 4.2, we present the --1 $w/L = 0.2$ mode in Figure 4.12. It is indicated in several previous sections that for narrower strips the -- solution becomes unstable. This instability is evident in the unusual curve shapes indicating a depletion of current near the center of the strip and in the rapid variation of J_y w.r.t. x .

Figures 4.13 and 4.14 show modes on the --6 trajectory. It is noteworthy that for $w/L = 1$, the J_y component of current dominates. The J_x component is small and manifests a rapid variation in phase w.r.t. y . The $w/L = 0.3$ mode on this trajectory indicates the expected breakup in a subtle fashion only. That is, the J_y component of current does not tend toward a singularity at $x/L = \pm 0.5$ as expected and as other cases manifest.

4.4 Conclusions

The poles and specimen natural modes for the dominant resonant region of the rectangular aperture are given in this chapter. The computed pole trajectories lend themselves to physically consistent interpretation. The broadband character of square and near-square structures noted by other workers is seen to be due to the relative proximity of several poles to the imaginary axis in the complex frequency plane. Pole trajectories for modes that have a dominant current component that is antisymmetric transverse to current flow are



$$w/L = 0.2$$

$$sL/c\pi = -1.360 + j.7891$$

Figure 4.12. Sample cuts in the natural mode distribution for the $--1$ mode with $w/L = 0.2$.

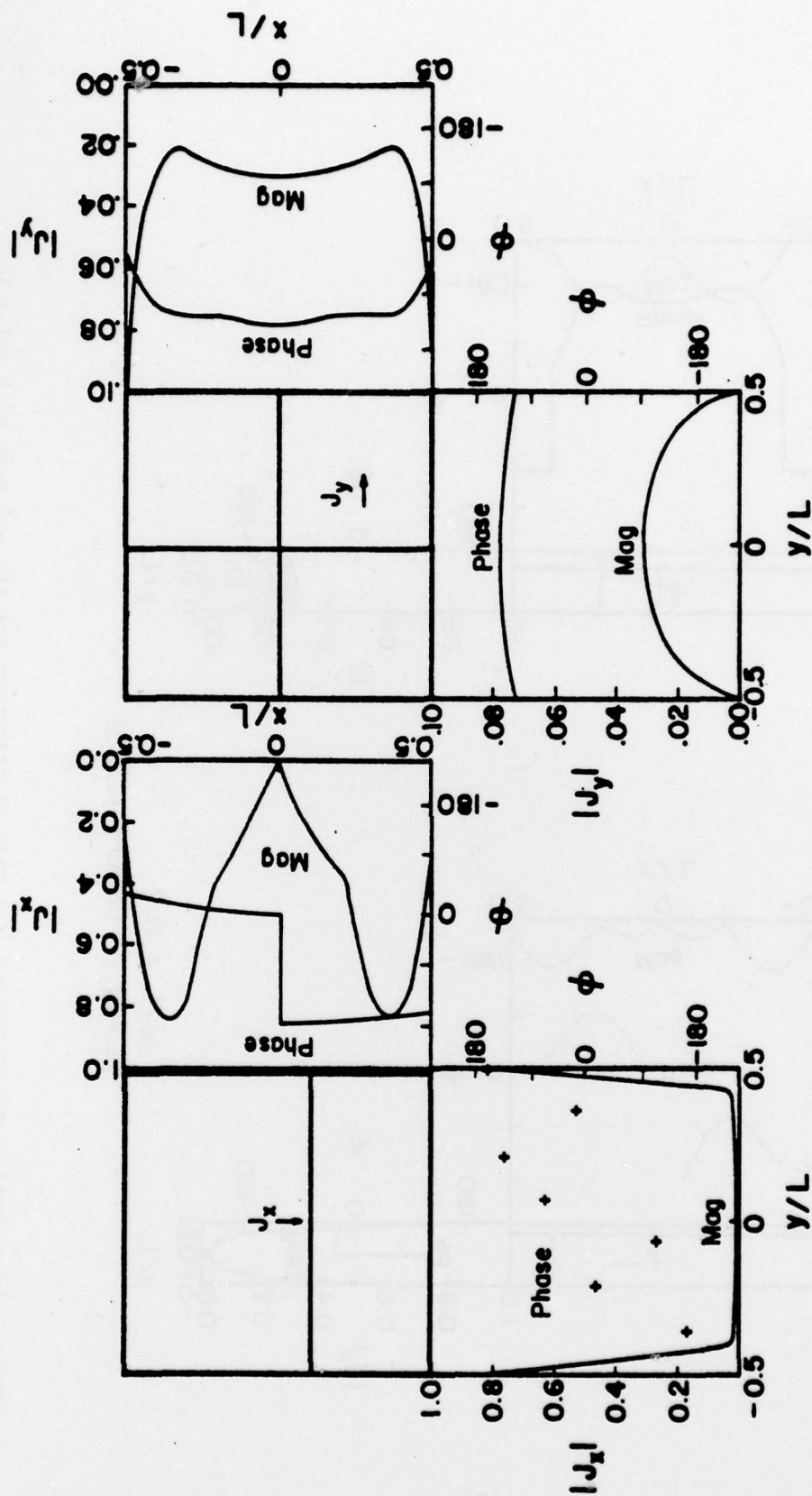


Figure 4.13. Sample cuts in the natural mode distribution for the --6 mode with $w/L = 1.0$.

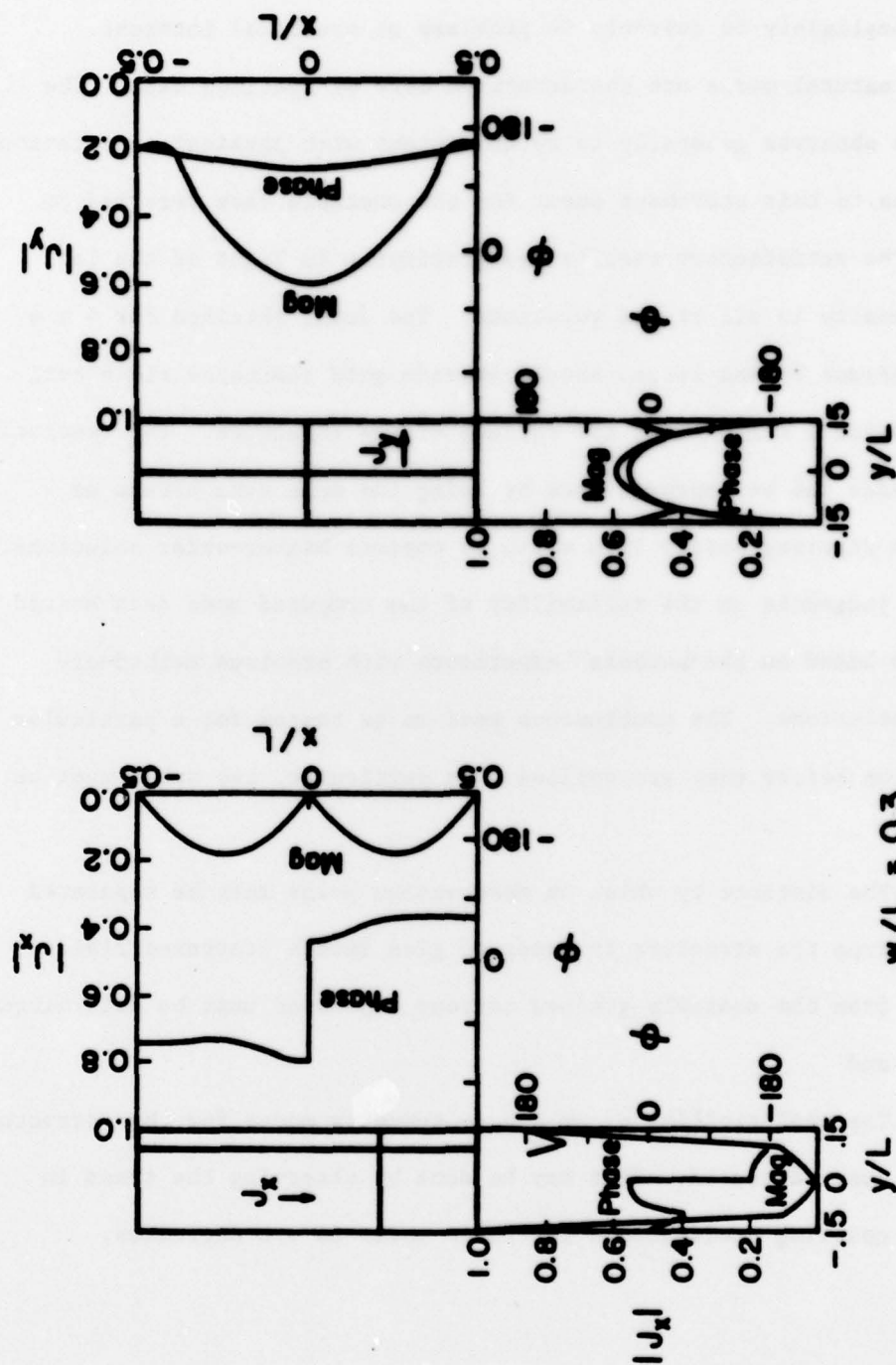


Figure 4.14. Sample cuts in the natural mode distribution for the --6 mode with $w/L = 0.3$.

undeterminable by the present method for strips narrower than about $w/L = 0.3$. Because of their antisymmetry, they are expected to contribute negligibly to currents in problems of practical interest.

The natural modes are characterized here by specimen data. The modes are observed generally to be consistent with physical expectations. Exceptions to this statement occur for the unstable case referred to above. The satisfactory results are gratifying in light of the low zoning density in all of the solutions. The data, obtained for 4×4 zones/quadrant by and large, should provide good scattered field estimates outside a region near the surface of the structure. The resolution of the modes can be improved upon by using the pole data herein as iteration starting points from which to conduct higher-order solutions.

The judgments on the reliability of the computed mode data stated above are based on the "authors'" experience with previous method-of-moments solutions. The conclusions need to be tested for a particular application before they are applied. In particular, two areas must be tested:

1. The distance by which an observation point must be separated from the structure in order to give smooth scattered fields from the coarsely grained current expansion must be determined; and
2. The negligibility of \rightarrow and $--$ symmetry modes for thin structures must be tested. This may be done by observing the trend in coupling coefficients for these modes as w/L decreases.

5. CONCLUSIONS

We attempt to fulfill two purposes with the work reported here. The first is to characterize the dual problems of the rectangular aperture and the rectangular plate. The second is to clarify some of the previously unsettled issues in the theory of SEM regarding suitability of particular coupling coefficient forms and the role of the entire function portion of the Mittag-Leffler form of the frequency domain singularity expansion.

That the first of these goals is met is supported by the inclusion of physically plausible SEM data given herein. Both the poles and natural modes determined lend themselves to straightforward physical interpretation. The natural mode information suffers from a "graininess" due to the use of minimal zoning density in the numerical procedures. It is anticipated that the only limitation imposed thereby is that coupled or scattered fields cannot be predicted from the modes in the immediate vicinity of the body.

The scope of the present effort did not allow time domain expansion of fields from the data herein. The ultimate judgment on the correctness and applicability of these results rests in their time domain applications. This testing shall necessarily include the causality tests proposed in Chapter 2.

The second goal has been partially fulfilled. Again, ultimate judgment must be deferred until the theoretical concepts in Chapter 2 are tested for their completeness in a broader range of problems. Specifically, the conclusions herein on these issues may be summarized as follows.

1. In a numerically conducted SEM solution, neither the entire function nor the asymptotic behavior of the frequency domain inverse kernel is explicitly recoverable.
2. If the Laplace transform inversion procedure is applied to the inverse kernel as a unit, assuming the net asymptotic behavior is available, the entire function contributes, at most, impulsive terms at the "turn-on" of the current.
3. The effect of the asymptotic behavior of the frequency inverse kernel is to dictate the support of its time domain counterpart. Functionally, in SEM this affects the form of the coupling coefficient.
4. The class 1 coupling coefficient and the asymptotic form implicitly assumed in using it are potentially inconsistent with causality if taken alone.
5. We have developed a conservative "class X" coupling coefficient which imposes causality directly. Further, we describe numerical tests whereby one may ascertain the consistency with causality of a given, less-conservative coupling coefficient, such as the class 1 or class 2 forms.
6. The asymptotic behavior of the series portion of the Mittag-Leffler form of the frequency domain expansion may be modified to admit to a class 1 coupling coefficient representation. This can quite possibly lead to acausal contributions to the solution, however, and an entire function contribution with support over a finite time must be included in the total solution in order to provide results consistent with causality.

We note several times in Chapter 2 that the class X coupling coefficient may prove unduly conservative for some problems. In fact, it is conservative for the transmission line and linear scatterer examples presented. Further work is needed to determine the conditions under which the class X imposition of causality may be relaxed to the class 2 form. The asymptotic behavior associated with the class 2 coefficient is equivalent to the asymptotic behavior of the residue series term by term. However, this series is not uniformly convergent, in general, and therefore does not admit directly to termwise integration. However, in the time domain inverse kernel plots in Chapter 2, the clear time between time zero and the time at which causality predicts the arrival of an incident wave indicates that the termwise integration would, indeed, produce correct results. The question of whether or not there is ever a need to include an entire function contribution with the class 2 and class X coupling coefficient expansions remains an open question.

REFERENCES

- [1] C. E. Baum, "The singularity expansion method," in Transient Electromagnetic Fields, L. B. Felsen, Ed., Heidelberg: Springer-Verlag, 1976, ch. 3, pp. 129-179.
- [2] C. E. Baum, "On the singularity expansion method for the solution of electromagnetic interaction problems," AFWL EMP Note IN 88, December 1971.
- [3] Y. Rahmat-Samii and R. Mittra, "A new integral equation solution of the electromagnetic aperture coupling and thin plate scattering problems," AFWL EMP Note IN 224, February 1975.
- [4] L. Marin, "Natural-mode representation of transient scattering from rotationally symmetric bodies," IEEE Trans. Antennas Propagat., vol. AP-22, no. 2, pp. 266-274, March 1974.
- [5] K. R. Umashankar, "The calculation of electromagnetic transient currents on perfectly conducting bodies using singularity expansion method," Ph.D. Thesis, University of Mississippi, Oxford, Mississippi, pp. 239-252, August 1974.
- [6] L. Marin and R. W. Latham, "Analytic properties of the field scattered by a perfectly conducting, finite body," AFWL EMP Note IN 92, January 1972.
- [7] F. M. Tesche, "On analysis of scattering and antenna problems using the singularity expansion technique," IEEE Trans. Antennas Propagat., vol. AP-21, no. 1, pp. 53-62, January 1973. (Also available as "On the singularity expansion method as applied to electromagnetic scattering from thin-wires," AFWL EMP Note IN 102, April 1972.)
- [8] D. R. Wilton and K. R. Umashankar, "Parametric study of an L-shaped wire using the singularity expansion method," AFWL EMP Note IN 152, November 1973.
- [9] K. R. Umashankar and D. R. Wilton, "Analysis of an L-shaped wire over a conducting ground plane using the singularity expansion method," AFWL EMP Note IN 174, March 1974.
- [10] L. Marin, "Transient electromagnetic properties of two parallel wires," AFWL EMP Note SSN 173, March 1973.
- [11] L. Marin, "Natural modes of two collinear cylinders," AFWL EMP Note SSN 176, May 1973.

REFERENCES (Continued)

- [12] T. H. Shumpert, "EMP interaction with a tin cylinder above a ground plane using the singularity expansion method," AFWL EMP Note SSN 182, June 1973.
- [13] F. M. Tesche, "Application of the singularity expansion method to the analysis of impedance loaded antennas," AFWL EMP Note SSN 177, May 1973.
- [14] C. E. Baum, "On the use of contour integration for finding poles, zeros, saddles and other function values in the singularity expansion method," AFWL ACT Note MaN 35, February 1974.
- [15] L. W. Pearson, "A data base for the SEM representation of the rectangular aperture and rectangular plate," University of Illinois Electromagnetics Laboratory Report 76-8, Department of Electrical Engineering, Urbana, Illinois, in preparation.
- [16] I. Stakgold, Boundary Value Problems of Mathematical Physics, Vol. 2, New York: McMillan, 1968, pp. 194-311.
- [17] C. E. Baum, "On the eigenmode expansion method for electromagnetic scattering and antenna problems, Part I: Some basic relations for eigenmode expansions, and their relation to the singularity expansion," AFWL EMP Note IN 229, January 1975.
- [18] G. F. Carrier, M. Krook and C. E. Pearson, Functions of a Complex Variable. New York: McGraw Hill, 1966, pp. 81-82.
- [19] A. I. Markushevich, Theory of Functions of a Complex Variable, Vol. II. Englewood Cliffs, New Jersey: Prentice-Hall, 1965, pp. 299-304.
- [20] L. Schwartz, Mathematics for the Physical Sciences. Reading, Massachusetts: Addison-Wesley, 1966, pp. 130-132.
- [21] C. E. Baum, "Use of singularities in the complex plane and eigenvalues of integral equations for transient and broadband electromagnetic analysis and synthesis," Proc. USNC/URSI Meeting, Urbana, Illinois, p. 111, June 3-5, 1975.
- [22] F. M. Tesche, private communication.
- [23] D. R. Wilton and K. R. Umashankar, private communication.
- [24] M. L. Van Blaricum, private communication.
- [25] M. L. Van Blaricum, "Techniques for extracting the complex resonances of a system directly from its transient response," Ph.D. Thesis, University of Illinois, Urbana, Illinois, 1976.

REFERENCES (Continued)

- [26] J. Van Bladel, Electromagnetic Fields. New York: McGraw-Hill, 1964, pp. 385-387.
- [27] C. E. Baum, "Interaction of electromagnetic fields with any object which has an electromagnetic symmetry plane," AFWL EMP Note IN 63, March 1971.
- [28] C. M. Butler, "Integral equation solution methods," in "Wire Antennas and Scatterers," Short Course Notes, University of Mississippi, Oxford, Mississippi, April 1972. (See also IEEE Trans. Antennas Propagat., Vol. AP-20, pp. 731-736, 1972.)
- [29] Subroutine ZANLYT, International Math Subroutine Library, International Math and Statistical Libraries, Suite 510, 6200 Hillcroft, Houston, Texas 77036 (available by institutional subscription).
- [30] K. S. Miller, Advanced Complex Calculus. New York: Dover, 1960, pp. 172-173.